Mar Biol (2009) 156:669–677
DOI 10.1007/s00227-008-1117-6

ORIGINAL PAPER

Sulfide assimilation by ectosymbionts of the sessile ciliate, *Zoothamnium niveum*

Hans Røy · Kay Vopel · Markus Huettel · Bo Barker Jørgensen

Received: 17 October 2008 / Accepted: 15 December 2008 / Published online: 3 February 2009

Abstract We investigated the constraints on sulfide uptake by bacterial ectosymbionts on the marine peritrich ciliate *Zoothamnium niveum* by a combination of experimental and numerical methods. Protists with symbionts were collected on large blocks of mangrove-peat. The blocks were placed in a flow cell with flow adjusted to in situ velocity. The water motion around the colonies was then characterized by particle tracking velocimetry. This shows that the feather-shaped colony of *Z. niveum* generates a unidirectional flow of seawater through the colony with no recirculation. The source of the feeding current was the free-flowing water although the size of the colonies suggests that they live partly submerged in the diffusive boundary layer. We showed that the filtered volume allows *Z. niveum* to assimilate sufficient sulfide to sustain the symbiosis at a few micromoles per liter in ambient concentration. Numerical modeling shows that sulfide oxidizing bacteria on the surfaces of *Z. niveum* can sustain 100-times higher sulfide uptake than bacteria on flat surfaces, such as microbial mats. The study demonstrates that the filter feeding zooids of *Z. niveum* are preadapted to be prime habitats for sulfide oxidizing bacteria due to *Z. niveum*'s habitat preference and due to the feeding current. *Z. niveum* is capable of exploiting low concentrations of sulfide in near norm-oxic seawater. This links its otherwise dissimilar habitats and makes it functionally similar to invertebrates with thiotrophic symbionts in filtering organs.

Communicated by M. Kühl.

Electronic supplementary material The online version of this article (doi:10.1007/s00227-008-1117-6) contains supplementary material, which is available to authorized users.

H. Røy · B. B. Jørgensen
Max Planck Institute for Marine Microbiology,
Celsiusstr. 1, 28359 Bremen, Germany

Present Address:
H. Røy (✉)
Department of Biological Sciences,
Center for Geomicrobiology, University of Aarhus,
Ny Munkegade 1535, 8000 Aarhus C, Denmark
e-mail: hans.roy@biology.au.dk

K. Vopel
School of Applied Sciences,
Auckland University of Technology, Mail No C43,
Private Bag 92006, Auckland 1142, New Zealand

M. Huettel
Department of Oceanography,
Florida State University, 117 N Woodward Ave.,
OSB 517, Tallahassee, FL 32306-4320, USA

Introduction

The peritrich ciliate *Zoothamnium niveum* (Ehrenberg 1838) forms attached contractile colonies that are visible to the naked eye. The colony shape resembles a feather with an average length between 3 and 5 mm. The side-branches of the "feather" carry several hundred microzooids (zooid = single ciliate) in a regular pattern (see Bauer-Nebelsick et al. 1996a, b for a detailed description). The entire surface of the zooids, stalk and branches are covered by a single layer of sulfide-oxidizing bacteria belonging to the Gamma-proteobacteria (Rinke et al. 2007). The peritrich ciliates are filter-feeders, and the microzooids of *Z. niveum* possess a fully developed oral ciliature and cytopharynx, similar to *Zoothamnium* species that are not covered by sulfide oxidizing bacteria (Bauer-Nebelsick et al. 1996b). Rapid contractions of zooids, branches and the distal parts of the stalk are characteristic of all *Zoothamnium*

Fig. 1 White spot around a 1 cm wide conduit into the peat wall. Several *Zoothamnium niveum* colonies can be seen around the hole. Recorded in situ with a Nikon coolpix 960 in underwater housing

species. For *Z. niveum,* the contraction takes only about 4 ms, and the average velocity reaches 520 mm s^{-1} (Vopel et al. 2002). During contractions and the following slow expansion the cilia cease.

The type organisms for a recent re-description of *Z. niveum* (Bauer-Nebelsick et al. 1996b) were collected on mangrove islands of the Belize barrier reef. Several ecological investigations have been performed on this population. Aggregations of *Z. niveum* and non-symbiotic sulfur-bacteria form characteristic "white spots" (Fig. 1) on undercut peat-banks under Red Mangrove (*Rhizophora mangle*) stands. Typical spots are 5–25 mm in diameter and contain 9–43 *Zoothamnium* colonies (Ott et al. 1998). The spots often occur around bark-lined holes in the peat. The holes form when a mangrove root dies and the core of the root decomposes. The seawater in these bark conduits is anoxic and contains up to 1 mmol L^{-1} sulfide. Sulfidic water in the conduits mixes with the surrounding seawater, primarily driven by wave-generated oscillating boundary flow. This makes the holes function like miniature sulfide vents (Vopel et al. 2005).

Though the published evidence is mostly suggestive, the association between *Z. niveum* and its ectosymbionts has been assumed to be obligatory. A trophic character of the symbiosis is suggested from observation of bacteria morphotypes in the food vacuoles (Bauer-Nebelsick et al. 1996b), and by poor growth of the ciliates without ectosymbionts (Ott et al. 1998; Vopel et al. 2001). Ott et al. (1998) proposed that *Z. niveum* supplies the bacterial symbionts with sulfide through periodic contraction into the anoxic and sulfidic diffusive boundary layer (DBL). Studies of the physical and chemical microenvironment around the colonies (Vopel et al. 2001, 2002, 2005) could not confirm this mechanism, but suggested that the feeding currents intercept sulfide and brings it to the symbiotic bacteria.

In this study, we link the sulfide transport quantitatively from the turbulent water column, via the feeding current, to the bacteria on the surface of *Z. niveum*. We analyze the flow field around individual colonies at high resolution. These data identify the source, pathway and volume of seawater passing through the colonies. We use literature data on the oxygen consumption of *Z. niveum* to estimate the sulfide requirements of the consortia based on the stoichiometry of lithothropic growth by sulfide oxidation. The filtered seawater volume together with the sulfide requirement provides a rough estimate of the constraints on sulfide uptake by the ecto-symbionts on *Z. niveum*. We refined the constraints further using numerical modeling.

Material and methods

Field site and sampling

Experimental work was conducted on the island of Carrie Bow Cay, Belize, in April 2002, at the field station operated by the Caribbean Coral Reef Ecosystem program of the National Museum of Natural History (Washington, DC, USA). Fieldwork was done in the channel that separates the two islands of Twin Cays, in an area locally known as Batfish Point. Detailed description of Twin Cays and the tidal channels can be found in Rützler and Macintyre (1982) and Ott et al. (1998).

In situ observations and ciliate collection were performed while SCUBA diving along undercut peat banks at Batfish Point. Current speed and direction were measured by timing 10 cm displacements of natural particles in the seawater with a stopwatch. Typical currents were 5–20 mm s^{-1} measured 1–3 cm from the peat surface. Then the spots with ciliate colonies were cut out together with a $20 \times 20 \times 20$ cm^3 block of surrounding peat and placed in a closed container while still under water.

Laboratory flow cell

After transport to the laboratory, the fibrous peat blocks were trimmed to fit a glass flow-cell that accommodated a 45 mm thick 90×150-mm peat block. Care was taken to align the surface of the peat flush with the inflow and to place the blocks with the same orientation to the current as

they were found in situ. Peat and ciliates were never exposed to air.

Water in the flow cell was re-circulated through an aerated container holding 7 L of seawater. At the entrance of the flow cell, seawater was passed through 50 mm of coarse filter-foam (blue EHEIM) to dissipate inflow turbulence. A similar foam block was placed downstream of the peat to prevent the flow from converging toward the outflow. The free-flow section between the foam blocks was 150 mm and the water depth during measurements 50 mm. Free flow velocity was adjusted to 1 cm s^{-1} reproducing a setting within the velocity range measured in situ (see below). The entire system was allowed to reach equilibrium at 29°C and 190 µmol O_2 L^{-1} before measurements. These values were within the range observed in the habitat. All laboratory observations were performed within 18 h from the time of collection.

Particle-tracking velocimetry

The flow cell was mounted on a metal frame together with a video microscope (Navitar) with a digital CCD camera (PCO SensiCam). A high resolution 2 × 1.5 mm image field was captured from 90 mm distance. The frame also carried a laser diode with optics (Lasiris LAS-670-30) that projected a 0.1 mm thick vertical light sheet aligned with the flow. Camera and laser were mounted on micromanipulators to allow precise control of the area imaged. The seawater in the experimental system was spiked with 10 µm diameter neutrally buoyant, hollow inert glass spheres, resulting in a turbidity matching the seawater at Batfish Point. Ciliates close to the center of the flow cell were illuminated with the vertical laser sheet and imaged by the CCD camera together with the particles suspended in the flow.

The images were subjected to four exposures of 1 ms separated by 2 ms intervals. The short intervals between the sub-exposures could resolve the fast flow in the swash behind a contracting colony by measuring displacement of particles between the first and the last exposure in a single image. Image sequences were recorded at a frequency of 10 s^{-1}. The slower background flow and feeding currents were resolved by multi-frame PTV: corresponding particles were identified in three consecutive images and the velocity calculated from the displacements. Each velocity field typically contained 500–1,000 independent vectors. The scattered vectors were calculated into sectional streak-lines in the chosen plane using Tecplot (Amtec Engineering).

Finite element modeling

Advective and diffusive sulfide transport around individual feeding micro zooids were calculated in COMSOL Multiphysics (Stockholm), which can perform reaction–diffusion–advection calculations in an arbitrary geometry by dividing it into triangular finite elements. The flow around individual zooids was calculated from the "Incompressible Navier–Stokes" application mode from the "Earth Science Module". Solute dynamics was calculated in the "Convection and Diffusion" application mode based on the results of the Navier–Stokes solution. Geometry of the zooids was based on Bauer-Nebelsick et al. (1996a, b) and that of *T. zoothamnicoli* on Rinke et al. (2007). The density of the calculation mesh was adjusted to give adequate calculation speed and tested not to influence the model results. Time steps were controlled dynamically to assure numerical stability. The applied model of *Z. niveum* describes a single radial-symmetric zooid with surrounding seawater. The purpose of the model was to describe the flux to the bacteria on the ciliates surface. Three scenarios were modeled: (1) one micro-zooid with functional cilliary apparatus; (2) a hypothetical scenario with a single isolated micro-zooid without feeding current, and (3) a single bacterial symbiont suspended in stagnant water.

Boundary conditions for scenario 1 were radial symmetry around the center of the zooid and unrestricted flow through upstream and downstream boundaries. The outer radial boundary was set to zero drag to simulate the presence of neighboring zooids with similar flow fields. The action of the cilliary apparatus was simulated by imposing a velocity of 0.6 mm s^{-1} parallel to the cell surface at the edge of the oral surface of the zooid. The boundary conditions for sulfide concentration were 3 µmol L^{-1} at the upstream boundary, radial symmetry around the center of the zooid and symmetry at the outer radial boundary. The downstream boundary was modeled purely as convective flux. Sulfide uptake was simulated by setting the concentration to zero at the surface of the zooid, which results in maximum estimates.

Scenario 2 contains no flow. The boundaries were moved 1 mm away from the zooid and sulfide concentration at the boundary was set to 3 µmol L^{-1}. Sulfide uptake was simulated by setting the concentration to zero at the surface of the zooid as in scenario 1. This accurately simulates an isolated zooid in an infinite seawater volume and was performed to separate the effect of the feeding current from the effect of zooid geometry. This approach neglects depletion of sulfide between the zooids and therefore gives a clear overestimation of the possible sulfide flux.

Boundary conditions for scenario 3: This scenario is a simple situation with a non-motile bacterial cell suspended in seawater. The modeled geometry was a 2 µm long and 1 µm thick rod-shaped bacterial cell in the centre of a 100 µm sphere of water. Sulfide uptake was simulated by setting the concentration to zero at the surface of the bacterium and the infinite pool of sulfide in the water outside the

modeled water sphere was simulated by setting the concentration on the outer boundary to 3 µmol sulfide L^{-1}. This scenario contains no flow.

Other parameters used in the models were a diffusion coefficient for sulfide (2.23×10^{-9} m^{-2} s^{-1}) and dynamic viscosity (10^{-3} Pa s). The morphology of the micro-zooid was taken from Bauer-Nebelsick et al. (1996b) and the dimensions of the bacterial symbionts from Rinke et al. 2007. Flow velocity through the ciliary apparatus (0.6 mm s^{-1}) was taken from the flow measurements. The sulfide concentration of 3 µmol sulfide L^{-1} is where Rinke et al. (2007) found optimal growth. This external concentration is well within the range measured between the colonies in situ by Vopel et al. (2005).

Results

In situ observations and peat description

The peat structure was fibrous with occasional clumps of carbonate clay. Permeability of the clean peat calculated from percolation under a constant hydraulic head of 1,500 Pa (Klute and Dirksen 1986), was 4.6×10^{-12} m^{-2} (SE 1.9×10^{-12}, $n = 15$). It corresponds to the permeability of fine sand (Huettel and Gust 1992). All colonies examined grew at the mouth of a bark-lined tube that reached at least 5 cm into the peat. The diameters of the holes were between 5 and 10 mm, but due to a fluffy overgrowth by root-fibers and microbial mats the opening was not always visible on the surface. Flows into, or out of, the bark channels were not apparent. Note, however, that at the concentration of sulfide in these channels is so high (Vopel et al. 2005) that even minute flows could supply enough substrate to drive a small thiotrophic community. *Z. niveum* grew attached to the exposed edges of the bark and to the peat within a distance of a few millimeters of the channel opening. White filamentous bacteria and pillows of filamentous sulfur were often found together with *Z. niveum,* but the ciliates were not generally found attached to areas covered by such mats.

Z. niveum colonies in situ contracted spontaneously at an average frequency of 1.7 min^{-1} (133 contractions observed in 78 min, distributed over 24 different colonies). Similar frequencies were observed in the laboratory. No correlation could be found between the concentration of suspended particles and contraction frequency. The time between contraction and restarting of cilliary motion varied from 2 to 5 s. Thus, the colonies spent 90% of the time fully stretched, with beating cilia.

Current velocity along the peat walls varied between 5 and 20 mm s^{-1}, measured 10–30 mm from the peat surface. Velocities encountered by the ciliates on the peat surface depended on both the free-stream velocity and the local topography (Fig. 2). As in all other graphs in this paper, the free-stream was from left to right. *Z. niveum* grew attached to top and sides of the "hill" in the center of Fig. 2 that contained the empty bark of a mangrove root. Most individuals were found on the sides of the hill where flow was reduced.

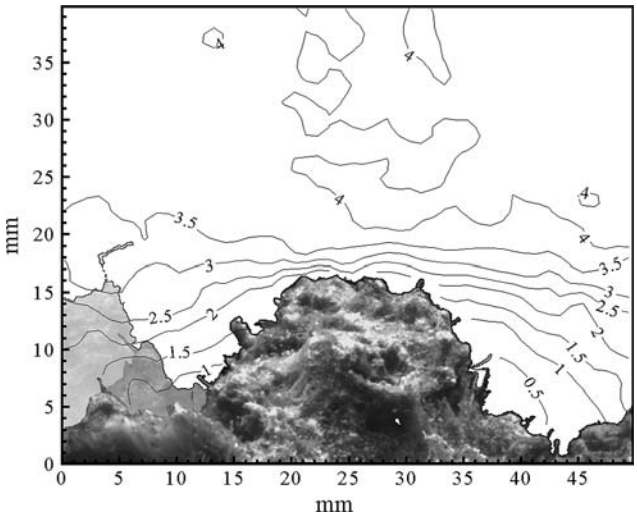

Fig. 2 Background flow along the rough peat surface. The flow, coming from the left, is visualized with isolines of equal flow speed. Note that these lines do not contain information about the flow direction. A *Zoothamnium niveum* colony on the lee side of the "hill" at $x = 35$ mm, $y = 10$ mm, can be seen close up in Fig. 3

Flow patterns during feeding

Three different current systems could be distinguished around feeding *Z. niveum*: (1) The feeding current, which is generated by the cilia of the zooids; (2) the secondary flow, which is induced by the feeding current but does not come into contact with the colony, and (3) the background current over the peat surface. Transitions between these current systems are smooth due to the prominence of viscous forces at low Reynolds numbers (Fig. 3a, b). The ambient current transforms smoothly into the feeding current, which passes through the colony along its entire length. The secondary current is seen as a vortex at the tip of the colony.

The feeding current was unidirectional through the colony from the convex side towards the concave (Fig. 3a). This seawater was ejected in a narrow band along the center-line of the colony. Velocity of the ejected seawater was always between 0.3 and 0.6 mm s^{-1}, irrespective of colony size and background flow. At this velocity the water of the feeding current spent less than 1 s in the colony. The measured velocity in the feeding current was in the narrow range expected for membranelle-generated flow (Fenchel 1986). The Reynolds number, based on the length of the ejected jet, was around 1. Closed streak-lines (Fig. 3a)

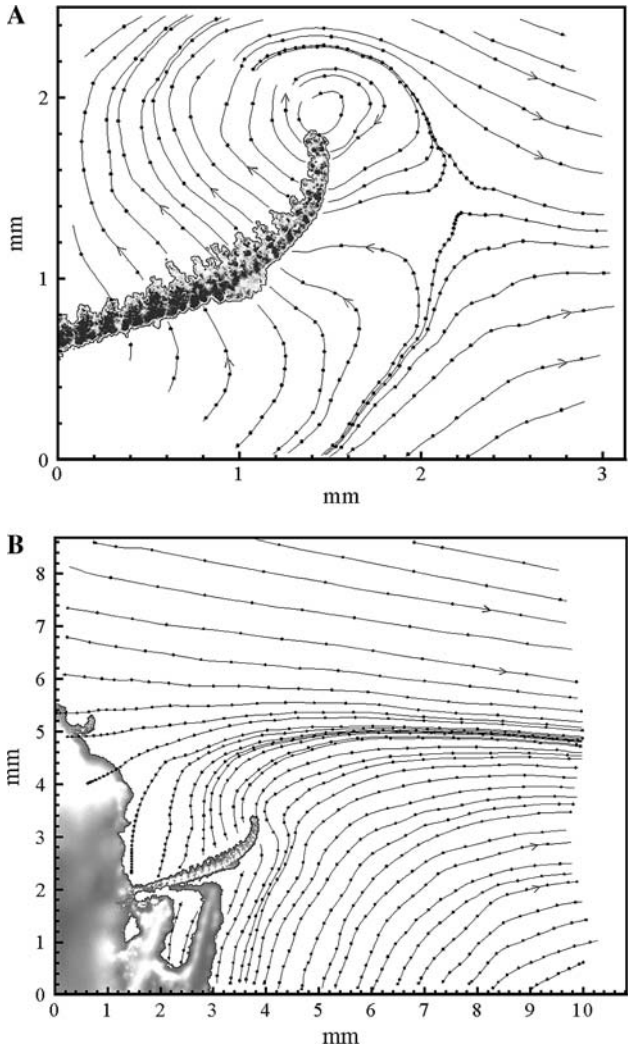

Fig. 3 **a** Flow field around a filtering *Zoothamnium niveum* in the backwater of a protruding bark channel. The same colony can be seen at $x = 37$ mm, $y = 8$ mm in Figs. 2 and 3b. The streak lines show the direction of the momentary flow. As the pattern was quasi stable, suspended particles in the seawater roughly followed these lines. The *dots* on the streak-lines correspond to water displacement during 1 s. Where the flow is diverging, as in the area around $x = 2$ mm, $y = 1$ mm, the flow in the depicted plane is replenished by an out-of-plane component. **b** Overview of the filtering *Zoothamnium niveum* also seen in Fig. 3a. The dots on the streak-lines corresponds to water displacement during 1 s

could imply that the feeding current is re-circulated in the distal 0.3 mm of the colony, but following single particles ejected at the tip until they left the laser sheet revealed that this was not the case.

The secondary current formed a toroid along the perimeter of the colony. Flow along the edges was similar to the vortex at the tip of the colony in Fig. 3a, but moved in the plane out of the paper. Smaller secondary toroidal flows could occasionally be seen as rapidly circulating particles at the edge of individual zooids. The spatial resolution of the camera setup did not allow quantitative description of these.

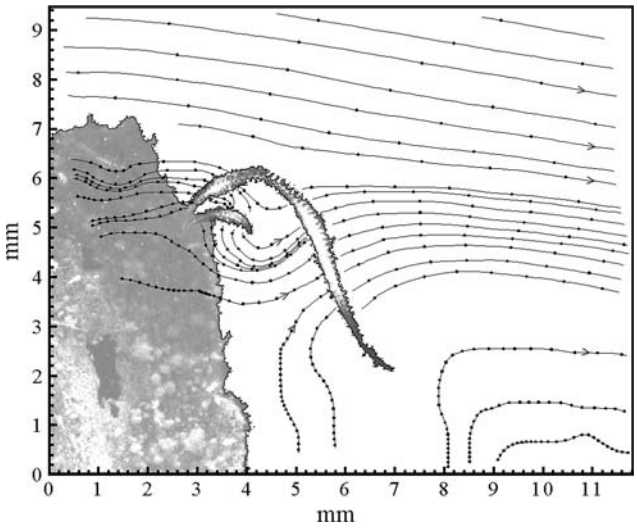

Fig. 4 Complex interactions between feeding currents of two *Zoothamnium niveum* colonies. The *dots* on the streak-lines corresponds to the water-displacement during 1 s. See text for details

Colonies larger than 4 mm often had side branches and were more or less twisted. The general flow patterns described for smaller colonies remained, but with the complication that the feeding- and secondary currents between different parts of the colony interacted (Fig. 4). Here, seawater passed through the zooids at the base of a large colony and was directly picked up by a smaller colony. The ejected seawater from the smaller colony was then drawn through another part of the large colony again, as the large colony now took in seawater at the other side due to a 180° twist. In situ, larger colonies were seen to bend back and forth in oscillating flow, which changed the orientation of the feeding currents continuously (see also Vopel et al. 2005).

Quantification of feeding current

Quantification of the flow through the colonies was complicated by the smooth transition between feeding current and secondary flow, but it can be constrained within narrow limits. A typical *Z. niveum* colony was 0.5 mm wide and 4 mm long, with the micro-zooids arranged in a single plane. It carried about 500 active microzooids, all on the outer 3 mm of the colony. Multiplying the 3 by 0.5 mm^2 cross-sectional area with the velocity of the ejected current (0.5 mm s^{-1}) suggests that a maximum 0.75 mm^3 of seawater passes through the colony each second. A minimal estimate was calculated as follows: Particles expelled in a 0.1 mm wide band along the centerline had approximately the same velocity, but particles dimly illuminated by scattered light along the light sheet often moved slower. If only the 0.1 mm thick zone with consistent velocities is considered

as the feeding current, then the seawater passed through the colony amounted to 0.15 $mm^3 s^{-1}$. The volume of 500 microzooids is 0.15 mm^{-3}. Thus, the volume-specific filtration rate of the zooids was 1–5 s^{-1}.

Flow patterns during ciliate contractions

Spontaneous contractions of *Z. niveum* were too fast to resolve with the camera used, but the fluid motion caused by the contractions could be followed (Fig. 5a). The ejected feeding current cannot be seen as it passed into the depicted plane. The colony was bending slightly away from the camera, so that the base of the colony was in the laser sheet, but the tip of the colony was behind it. A part of the secondary toroidal flow along the colony edges can therefore be seen as converging vectors around the colony. In the next image frame 0.1 s later the colony had contracted, leaving a swash of seawater in its wake (Fig. 5b). Note that the vector scale was reduced by one order of magnitude relative to Fig. 5a. The maximum velocity in Fig. 5b was about 13 mm s^{-1}, but velocities in excess of 30 mm s^{-1} were observed (data not shown). The seawater motion in the swash decayed almost to a standstill over the following ~0.7 s. The swash completely replaced the seawater around the contracted colony with seawater from above. The colony re-extended up through the decaying swash and, thus, into seawater reaching it from above rather than from the peat surface. During extension, the colony unfolded from the base upwards, and the zooids resumed cilliary pumping when the stretched position was achieved.

Modeled flow and sulfide uptake

The water volume forced directly by the cilia of the modeled zooid was 0.0004 $mm^3 s^{-1}$ while the total water volume transported was 0.0015 $mm^3 s^{-1}$. Volumes correspond to 0.21 and 0.75 $mm^3 s^{-1}$ for a colony with 500 zooids (0.15−0.75 $mm^3 s^{-1}$ was estimated from flow measurements). In both cases, the difference between the low and high estimate was due to inclusion of various amounts of secondary flow at the border of the feeding current (Fig. 6). Note that this part of the secondary flow contributed to the sulfide flux because of molecular diffusion towards the depleted feeding current. The resulting sulfide flux to the zooid is presented in Fig. 7. The vertical axis represents distance along the surface of the zooid from the base towards the centre of the oral surface. The starting point coincides with the lower boundary of Fig. 6, i.e. on the stalk 3 µm below the base of the zooid. In essence, the vertical axis could be wrapped around the perimeter of the zooid in Fig. 6. The flux-peak at 65 µm occurred at the edge of the oral surface. The sulfide uptake in Fig. 7, integrated across the surface of a feeding micro-zooid (scenario 1), is

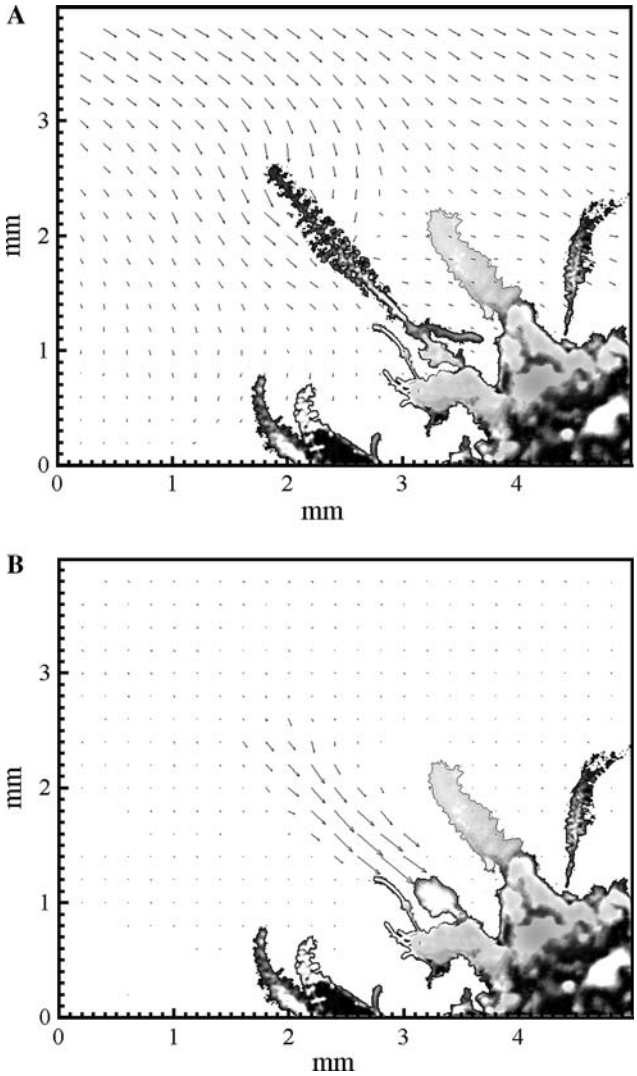

Fig. 5 **a** Flow field around a *Zoothamnium niveum* immediately before a contraction. Several non-contracting colonies are also seen. The vectors correspond to the seawater displacement during 0.25 s. **b** The flow field around a *Z. niveum* within 100 ms after a contraction. The vectors correspond to the seawater displacement during 0.025 s, one tenth of the vector length in Fig. 5b. The field of view is the same as seen in Fig. 4, which was recorded 0.1 s before. The contracted colony can be seen at $x = 3.5$ mm, $y = 1$ mm

2.0 × 10^{-15} mol s^{-1}, while the hypothetical situation without flow yields a total uptake of 1.1 × 10^{-15} mol s^{-1}. The cell specific sulfide uptake rate of *T. zoothamnicoli* in the two scenarios was 3.9 × 10^{-18} and 2.0 × 10^{-18} mol s^{-1} respectively, based on the fluxes on the distal 15 µm of the zooid and the "foot print" of the bacteria. To compare, the cell specific flux to the suspended bacterium was 38 × 10^{-18} mol s^{-1} (model scenario 3, geometry not shown). The maximum sulfide flux to a monolayer of bacteria on a planar surface under the same conditions as in the models can be calculated directly from the concentration in the seawater column and the thickness of the DBL. The planar DBL in marine environments ranges from 0.2 to 1.2 mm and is usually

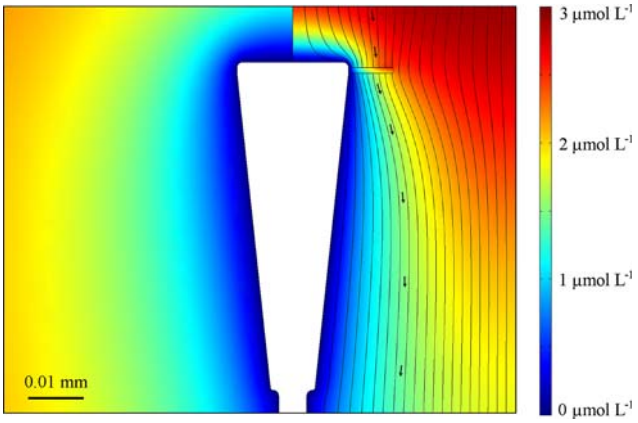

Fig. 6 Modeled sulfide concentration around a filtering (right half with streamlines) and a hypothetical non-filtering (*left half*) *Zoothamnium niveum* microzooid. The area where the flow was forced to 0.6 mm s^{-1} to simulate the cilia-generated current is marked by a box next to the zooid. *Arrows* indicate flow direction. The distance from the centerline to the right perimeter indicate the width of the domain modeled with flow while all other dimensions of the graph only shows a subsection of the modeled area

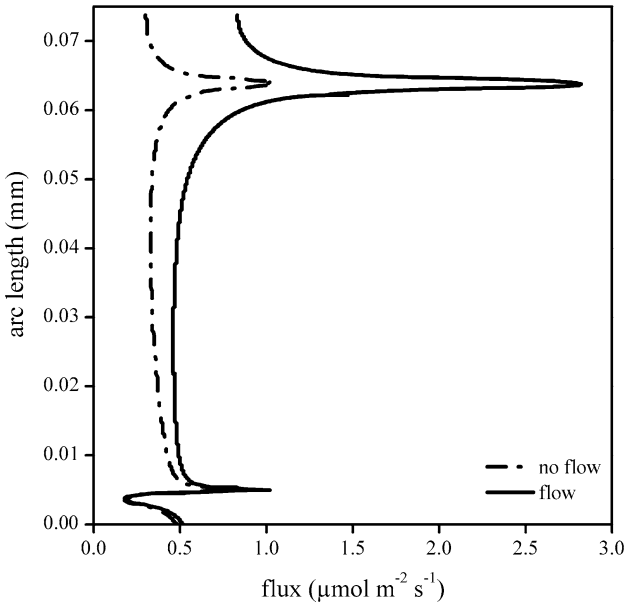

Fig. 7 Flux to the surface of a *Zoothamnium niveum* microzooid. The vertical axis in Fig. 7 represents distance along the surface of the protist from the base towards the center of the oral surface. The broken line represents the hypothetical non-filtering situation

close to 0.5 mm (Jørgensen 2001). This gives a maximum sulfide flux of 0.01 µmol m^{-2} s^{-1}, corresponding to 0.013×10^{-18} mol s^{-1} per cell the size of *T. zoothamnicoli,* if the bacteria cover the surface in a single layer.

Sulfur budget of *Z. niveum*

There are no published data on sulfide assimilation rates of the *Z. niveum* symbiosis. But the sulfur budget can be calculated from oxygen consumption rates published by Ott et al. (1998). These authors measured the oxygen flux to freshly collected *Z. niveum* in non-sulfidic medium to be 460 (SD 40) nL O_2 mm^{-2} of ciliate surface per hour (original units). The flux decreased to 140 (SD 16) nL O_2 mm^{-2} h^{-1} over 20 h, after which it remained stable. The time span over which the flux decreased corresponds to the time it takes *Z. niveum* to change from white to translucent when removed from its natural environment. We therefore assume that the difference between the initial flux and the stable flux can be attributed to oxidation of the sulfur globules in the symbionts. This assumption is supported by the observation of Ott et al. (1998), that a high flux could be re-established through incubation in sulfidic medium. As calculated from the difference between initial and stable flux and transferred to SI units, the oxygen flux going to sulfur oxidation is 3.97 (SD 0.53) µmol m^{-2} s^{-1}.

The oxidation of 2 mol of elemental sulfur to sulfuric acid requires 3 mol of O_2. By applying this stoichiometric relation to the O_2 flux, we get the initial rate of sulfur oxidation: 2.64 µmol m^{-2} s^{-1}. As the elemental sulfur only acts as an intermediate storage compound, the oxidation of S^0 must be coupled 1:1 to uptake and partial oxidation of ΣH_2S during normal growth conditions. One molecule of O_2 is required to oxidize two molecules of hydrogen sulfide to elemental sulfur, and this amount must be added to the 3.97 µmol O_2 m^{-2} s^{-1}, raising the O_2 flux required for sulfur oxidation to 6.61 µmol m^{-2} s^{-1}. During chemoautotrophic growth, a part of the electrons assimilated from hydrogen sulfide are channeled into carbon fixation and thereby are not reflected in the O_2 budget. In *Beggiatoa* this amounts to 20% of the electrons used for energy conservation (Nelson et al. 1986). Applying the same growth efficiency on the symbionts on *Z. niveum,* we must add 20% to the ΣH_2S flux calculated from the O_2 flux. Summing up, the bacteria on the surfaces of the *Z. niveum* for which Ott et al. (1998) measured the O_2 consumption must have sustained a ΣH_2S flux of 3.19 (SD 0.42) µmol m^{-2} s^{-1} and an O_2 flux of 6.61 (SD 0.88) µmol m^{-2} s^{-1} to be in steady state with respect to stored elemental sulfur. Compare this to the modeled flux in Fig. 7.

We consider a 4 mm tall *Z. niveum* colony with 50 side branches carrying a total of 500 microzooids as a standard colony, and that a typical white spot of 1 cm^2 contains 26 such colonies (Ott et al. 1998). According to the dimensions of the zooids given by Bauer-Nebelsick et al. (1996b), the surface area of one colony was about 2.5×10^{-6} m^2. Thus, the total sulfide oxidation of all *Z. niveum* within one spot was 2.07×10^{-10} mol sulfide s^{-1}, or 2.07 µmol sulfide m^{-2} s^{-1} for the area of the white spot. This is above the maximum sustainable flux to a *Beggiatoa* mat that is constrained by oxygen diffusion through the 0.2–1.2 mm thick DBL (Jørgensen 2001).

Discussion

Sulfide assimilation by *Z. niveum*

Ott et al. (1998) suggested that the swarmers (dispersion stage) of *Z. niveum* preferentially settle where the microbial mat leaks hydrogen sulfide. The attached swarmer has a diameter around 100 µm, and will be completely submerged in the DBL. It develops into young colonies in about 4 days. During this period, the parts of the colony that carry the ecto-symbionts will grow into the mixed seawater column. One way to explain the continued growth on sulfide oxidation as the colony grows away from the peat surface is periodic contraction into a sulfidic boundary layer as proposed by (Ott et al. 1998). As seen in Fig. 5b, however, the rapid contraction of a *Z. niveum* colony generates a swash of seawater towards the base area of the ciliate. This result confirms the observations of Vopel et al. (2001), that a contraction is followed by an increase in oxygen concentration at the base of the colony. Due to inertia, the fluid motion initiated by the contraction persists for a while after the driving force has vanished. As a result, the seawater surrounding the contracted colony is fully oxygenated seawater directly from the seawater column. During the following slower extension, most of the seawater that follows the colony back up has therefore spend less than one-second at the peat surface. The model proposed by Ott et al. (1998) suggested that more seawater should adhere to the colony when extending than during contraction. In this respect our measurements showed the opposite. This is explained by basic hydrodynamic principles: The drag on objects moved through a fluid at high velocities is proportional to the velocity squared. Therefore, more seawater is transported inwards via the fast contraction than what is drawn back out with the slow expansion of the *Z. niveum* colonies. Once back in the mixed seawater column, the resumption of cilliary pumping ejects the seawater from the colony. Thus, the exposure to seawater from the water layer near the peat surface is limited and the contractions do not supply sulfide via the mechanism proposed by Ott et al. (1998).

Sulfide dispersing from the bark conduits into the seawater column is a more likely source than a sulfidic boundary layer below the *Z. niveum* colonies. The gentle surge from surface waves results in an unstable mixture of fully oxygenated and sulfide-containing seawater in front of the conduit opening (Vopel et al. 2005). Turbulent mixing and advective transport will be controlling the concentration and distribution of sulfide, as these mechanisms will remove solutes much faster than the slow abiotic reaction between sulfide and O_2 (Zhang and Millero 1994; Visser et al. 1997; Zopfi et al. 2001). Turbulent diffusion is rapid in open water. We should therefore expect the sulfide concentration to drop very fast with increasing distance from the conduit opening, which is consistent with the sharp limits of the white spots. We propose that *Z. niveum* extracts the sulfide necessary to sustain the symbiosis from the mixture of small amounts of sulfidic water from the mouth of the bark conduits and air-saturated seawater. This view of the *Z. niveum* niche on the peat banks of Belizean barrier islands resembles the conditions in locations on Corsica, France, where it recently has been found. Here it lives attached to rock surfaces in the vicinity of decaying sea grass (Rinke et al. 2007). Micro-molar concentration of sulfide in norm-oxic seawater is also the medium in which *Z. niveum* has been successfully cultivated.

If the symbiotic bacteria on *Z. niveum* were growing on a two-dimensional surface instead of on a ciliate, then the maximum sulfide uptake rate would be about 1% of that calculated from the oxygen consumption rates and from the numerical model (see calculations above). This is possible because the dynamics of seawater motion over the surfaces of a zooid are drastically different than seawater moving over a microbial mat on a two-dimensional surface. At the zooid surface, the seawater motion is drawn from the surface via the cilliary motion, while the flow is retarded by friction with the seawater at further distance from the colony. In effect, it is a boundary layer turned inside out. Thus, the surface of the zooid comes in close contact with seawater carrying solutes at the concentration of the bulk seawater (Fig. 6, right). The modeled flux to the zooid surface (Fig. 7) is a conservative estimate since it is modeled without taking into account the ciliary activity on the oral surface. Nevertheless, there is agreement between the average flux in Fig. 7 and the flux calculated from oxygen consumption (3.19 µmol m^{-2} s^{-1}). By comparing the modeled flux with and without feeding current (Fig. 7), it appears that that a large part of the enhanced flux to the zooid can be explained by the slender radial geometry rather than to the feeding current, since the scenario modeled with active pumping is only twice as high as to passive diffusion. The purely diffusive calculation is, however, clearly an overestimation since it neglects competition for sulfide between neighboring microzooids. Thus, the main mechanism behind the high sulfide flux is the feeding current. The highest sulfide flux occurs near the ciliature, and this corresponds to the pattern of systematically large bacterial symbionts found on the oral parts of the zooids by Rinke et al. (2007).

The maximum sulfide uptake by suspended bacteria is still one order of magnitude higher than what is possible on the surface of *Z. niveum.* Thus, there would be a theoretical gain for the bacteria in pelagic life, but at an obvious disadvantage when relying on a point source of substrate located in a wave-swept environment.

Conclusions

The surfaces of *Z. niveum* are a much more favorable habitat for sulfide-oxidizing bacteria than a two-dimensional surface, when sulfide and oxygen coexist in the seawater around the colonies. Considering the consortia of *Z. niveum* with its ectosymbionts as specialized in acquiring low concentrations of sulfide from the seawater column agrees well with its occurrence on stones and vertical rocks adjacent to decomposing sea grass in the Mediterranean. Diffusive supply of sulfide from below can be excluded when the substrate is stone. But when thick layers of sea grass decompose in a wave-swept environment, it is likely that small amounts of H_2S are present in the seawater column. It is interesting to note that the larger the ciliate colony grows, the better it will come in contact with the seawater column. Any influence the bacteria have that increases the size of the ciliate colony will thereby be beneficial to bacteria depending on solutes from the seawater column. This sets a likely scenario for the evolution of a trophic symbiosis, as well as giving a possible explanation for the large size of the *Z. niveum* relative to other ciliates. The feature that makes the surfaces of *Z. niveum* a lucrative habitat for sulfide-oxidizing bacteria is the feeding current. So rather than being a special case, exploiting sharp, crossing gradients of sulfide and O_2, *Z. niveum* is more likely functionally equivalent to metazoans carrying symbionts in filtering organs such as the clams and tube worms of hydrothermal fields (e.g., Cavanaugh 1994).

Acknowledgments This work was supported by the Caribbean Coral Reef Ecosystems program of the Smithsonian National Museum of Natural History (Washington, DC), the Danish Research Academy and the Max Plank Society. We thank J. Ott for introducing us to the study *Z. niveum*, and M. Carpenter and D. Miller for support on Carrie Bow Cay. The manuscript was greatly improved by constructive reviews. This is contribution 658, Caribbean Coral Reef Ecosystems Program, Smithsonian Institution. The experiments comply with the current laws of Belize and Germany.

References

Bauer-Nebelsick M, Bardele CF, Ott JA (1996a) Electron microscopic studies on *Zoothamnium niveum* (Hemprich & Ehrenberg, 1831) Ehrenberg 1838 (Oligohymenophora, Peritrichida), a ciliate with ectosymbiotic, chemoautotrophic bacteria. Eur J Protistol 32:202–215

Bauer-Nebelsick M, Bardele CF, Ott JA (1996b) Redescription of *Zoothamnium niveum* (Hemprich & Ehrenberg, 1831) Ehrenberg, 1838 (Oligohymenophora, Peritrichida), a ciliate with ectosymbiotic, chemoautotrophic bacteria. Eur J Protistol 32:18–30

Cavanaugh CM (1994) Microbial symbiosis—patterns of diversity in the marine-environment. Am Zool 34:79–89

Fenchel T (1986) Protozoan filter feeding. Prog Protistol 1:65–113

Huettel M, Gust G (1992) Solute release mechanisms from confined sediment cores in stirred Benthic Chambers and Flume Flows. Mar Ecol Prog Ser 82:187–197. doi:10.3354/meps082187

Jørgensen BB (2001) Life in the diffusive boundary layer. In: Boudreau BP, Jørgensen BB (eds) The benthic boundary layer: transport processes and biogeochemistry. Oxford University Press, New York, pp 348–373

Klute A, Dirksen C (1986) Hydraulic conductivity and diffusivity: laboratory methods. In: Klute A (ed) Methods of soil analysis—part 1—physical and mineralogical methods. Am Soc Agron, Madison

Nelson DC, Jørgensen BB, Revsbech NP (1986) Growth-pattern and yield of a chemoautotrophic *Beggiatoa* sp in oxygen-sulfide microgradients. Appl Environ Microbiol 52:225–233

Ott JA, Bright M, Schiemer F (1998) The ecology of a novel symbiosis between a marine peritrich ciliate and chemoautotrophic bacteria. Mar Ecol-Pubbl Stn Zool Napoli 19:229–243

Rinke C, Schmitz-Esser S, Stoecker K, Nussbaumer AD, Molnar DA, Vanura K, Wagner M, Horn M, Ott JA, Bright M (2007) "Candidatus thiobios zoothamnicoli" an ectosymbiotic bacterium covering the giant marine ciliate *Zoothamnium niveum*. Appl Environ Microbiol 72:2014–2021. doi:10.1128/AEM.72.3.2014-2021.2006

Rützler K, Macintyre IG (1982) The habitat distribution and community structure of the barrier reef complex at Carrie Bow cay, Belize. In: Rützler K, Macintyre IG (eds) The Atlantic barrier reef ecosystems at Carrie Bow Cay, Belize, I: structure and communities. Smithsonian Institution Press, Washington, pp 9–45

Visser JM, Robertson LA, VanVerseveld HW, Kuenen JG (1997) A novel membrane-bound flavocytochrome C sulfide dehydrogenase from the colourless sulfur bacterium *Thiobacillus* sp. W5. Arch Microbiol 167:295–301. doi:10.1007/s002030050447

Vopel K, Pöhn M, Sorgo A, Ott JA (2001) Ciliate-generated advective seawater transport supplies chemoautotrophic ectosymbionts. Mar Ecol Prog Ser 210:93–99. doi:10.3354/meps210093

Vopel K, Thistle D, Ott JA, Bright M, Røy H (2005) Wave-induced H_2S flux sustains a chemoautotrophic symbiosis. Limnol Oceanogr 50:128–133

Vopel K, Reick CH, Arlt G, Pöhn M, Ott JA (2002) Flow microenvironment of two marine peritrich ciliates with ectobiotic chemoautotrophic bacteria. Aquat Microb Ecol 29:19–28. doi:10.3354/ame029019

Zhang JZ, Millero FJ (1994) Kinetics of oxidation of hydrogen sulfide in natural waters. In: Alpers CN, Blowes DW (eds) Environmental geochemistry of sulfide oxidation. Am Chem Soc, Washington, pp 393–409

Zopfi J, Ferdelman T, Jørgensen BB, Teske A, Thamdrup B (2001) Influence of water column dynamics on sulfide oxidation and other major biogeochemical processes in the chemocline of Mariager Fjord (Denmark). Mar Chem 74:29–51. doi:10.1016/S0304-4203(00)00091-8

CSIRO PUBLISHING

www.publish.csiro.au/journals/mfr *Marine and Freshwater Research*, 2008, **59**, 1101–1110

Modification of sediment–water solute exchange by sediment-capping materials: effects on O_2 and pH

K. Vopel[A,B,C], *M. Gibbs*[A], *C. W. Hickey*[A] *and J. Quinn*[A]

[A]National Institute of Water and Atmospheric Research, PO Box 11-115, Hamilton, New Zealand.
[B]Present address: Auckland University of Technology, School of Applied Sciences and Earth and Oceanic Sciences Research Institute, Mail No C43, Private Bag 92006, Auckland, New Zealand.
[C]Corresponding author. Email: kay.vopel@aut.ac.nz

Abstract. The release of phosphorus from sediments can stimulate algal blooms in eutrophic water bodies worldwide. One technique to reduce this release involves capping the sediment with millimetre-thick layers of chemically active materials such as aluminium hydroxide floc (alum), and the mineral-based products Phoslock and modified zeolite. The effects of this technique on transport and reaction of diagenetically important sediment compounds other than phosphorus are unknown. The present study used microelectrodes to measure the apparent gas diffusivity of capping layers derived from different doses of these capping materials and their effects on pore water pH and dissolved molecular oxygen. The apparent O_2 diffusivity of alum capping layers (1.58×10^{-5} cm^2 s^{-1}) was constant with depth and higher than that of mineral-based capping layers ($\sim 1.15 \times 10^{-5}$ cm^2 s^{-1} and decreasing with depth in the capping layer). The capping materials raised the depth of the oxic–anoxic interface and associated pH minimum and altered the sediment O_2 consumption as functions of the capping-layer thickness and apparent diffusivity. Modified zeolite layers decreased pore water pH slightly (0.3–0.5 units); alum layers decreased pH by 1–2.2 units. It is proposed that capping layers derived from doses >200 g m^{-2} can alter benthic process rates and solute fluxes.

Additional keywords: apparent diffusivity, diffusion, mass transport, oxygen and pH microprofiles, sediment–water interface.

Introduction

Eutrophication of inland water bodies frequently results from increased flux of plant nutrients from the catchment to the receiving water bodies. Although remedial changes to catchment use that reduce this external load may reverse eutrophication, this process is often slowed or prevented where substantial internal loads are present. Internal loads are derived from the sediment release of inorganic nitrogen (N) and phosphorus (P) generated by microbial decomposition of organic material. The P-binding capacity of the sedimentary iron(III) oxide–hydroxide may prevent the release of P from the sediment but during stratification, bottom-water hypoxia leads to the reduction of Fe(III) to Fe(II) and the release of P from the sediment. Where internal loads are advected into the photic zone, they can fuel further algal production. If this algal production returns to the sediments, it can create a cycle that retains high nutrient levels within the aquatic system (Rowe *et al.* 1975; Cooke *et al.* 1993). One technique often advocated to break this cycle, and thus expedite the reversal of eutrophication, is to capture P released from the sediment by capping the sediment surface with materials capable of chemically precipitating P. Aluminium hydroxide (alum) (Reitzel *et al*. 2003, 2005) and the mineral-based products Phoslock (Robb *et al.* 2003) and modified zeolite (Jacobs and Förstner 1999) are examples of such materials.

Alum is usually applied in the form of aluminium sulfate that dissociates in water. A subsequent series of hydrolysis reactions leads to the liberation of hydrogen ions and, in the appropriate pH range, the formation of aluminium hydroxide, $Al(OH)_3$, a colloidal, amorphous floc with high coagulation and P adsorption properties that settles through the water column to the sediment surface. Phoslock is a lanthanum (La) modified bentonite clay developed by the Australian Commonwealth Scientific and Industrial Research Organisation (CSIRO). The mechanism of P removal by Phoslock involves the reaction of phosphate anions with La, leading to formation of a single insoluble species of lanthanum phosphate or rhabdophane ($La^{3+} + PO_4^{3-} \rightarrow LaPO_4$) (Douglas *et al.* 1999; Douglas 2002). Modified zeolite is a pre-commercial product developed by Scion in New Zealand by treating raw zeolite – crystalline, hydrated aluminosilicates that contain alkali and alkaline-earth metals – with aluminium-based substances. Owing to their high cation exchange capacity, unmodified zeolites are widely used in water and sewage treatment (Colella 1999), and for capping chemically contaminated sediments (Jacobs and Förstner 1999). Scion's proprietary method for partially converting the zeolite to a cationic form enhances uptake of anionic pollutants, such as phosphorus, while retaining its cationic exchange properties.

Although there have been studies of the efficacy of sediment surface deposits (hereafter capping layers) of some of these materials in immobilising dissolved phosphate (e.g. Sakadevan and Bavor 1998; Welch and Cooke 1999; Robb *et al.* 2003; Akhurst *et al.* 2004), a comprehensive understanding of the ecological

 10.1071/MF08130 1323-1650/08/121101

consequences of using capping materials requires knowledge of how they interact with natural sedimentary transport and reaction processes. In particular, the effects of capping layers in terms of their composition and thickness on the distributions and fluxes of reactive solutes are not well known. We investigated how capping layers modify the distribution of two pore water solutes. We first characterised properties of the capping layers that affect the diffusive sediment–water solute exchange; we then determined how these capping layers modify pore water micro-gradients in concentrations of hydrogen ions (pH) and dissolved molecular oxygen (hereafter $[O_2]$) on representative natural lake sediment. We studied these solutes because they are critical components of most biogeochemical processes that occur close to sediment–water interfaces (Stumm and Morgan 1996; Burdige 2006).

Materials and methods

Experimental design

All experiments involved the use of Unisense A/S microelectrodes and a Unisense A/S microelectrode positioning system (www.unisense.com) to record solute concentration profiles normal to the sediment surface from a position in the overlying lake water through capping layers to some depth in the sediment. Sediments and lake water were from Lake Rotorua, a eutrophic, polymictic lake in the central volcanic plateau, North Island, New Zealand (79.8 km^2, mean depth 10.5 m).

Three capping materials were used: 0.5–2-mm granule Phoslock (Phoslock Water Solutions, Waterloo, NSW, Australia), 1–3 mm granule modified zeolite (Scion, Rotorua, New Zealand) and alum floc made by adding aluminium sulfate, $Al_2(SO_4)_3 \times 16\,H_2O$, to lake water. Before application, Phoslock and modified zeolite were ground to a fine powder with a mortar and pestle and passed through a 125-μm sieve to standardise their granule size (Fig. 1).

Two series of experiments were undertaken. The first series (Series 1) was to estimate the thicknesses and apparent gas diffusivities, ϕD_S, of capping layers derived from addition of different doses of the three capping materials to lake water. The apparent gas diffusivity combines the parameter porosity (ϕ) and the effective diffusion coefficient (D_S), and is used to describe the diffusive sediment–water exchange of solutes with Fick's law of diffusion. We added five doses of each of the three capping materials to lake water overlying standardised fine sand and then measured the diffusion of hydrogen gas in the pore water of the capping layers using a hydrogen-gas-filled microelectrode (Revsbech *et al.* 1998). We used fine sand as substrate because we expected its diffusivity to be much lower than that of the capping layer; a large difference in the diffusivity of the two substrates will cause a distinct discontinuity in the diffusivity profile at the depth of the capping layer–sand interface that can be used to estimate the thickness of the capping layer.

The second series of measurements (Series 2) investigated the effects of such capping layers on the distribution of solutes in the underlying lake sediments. We added three doses of the three capping materials to water above sediment cores collected in Lake Rotorua and measured pore water pH (two doses) and $[O_2]$ (three doses) in their capping layers and the lake sediment. Reference for Series 2 was uncapped lake sediment.

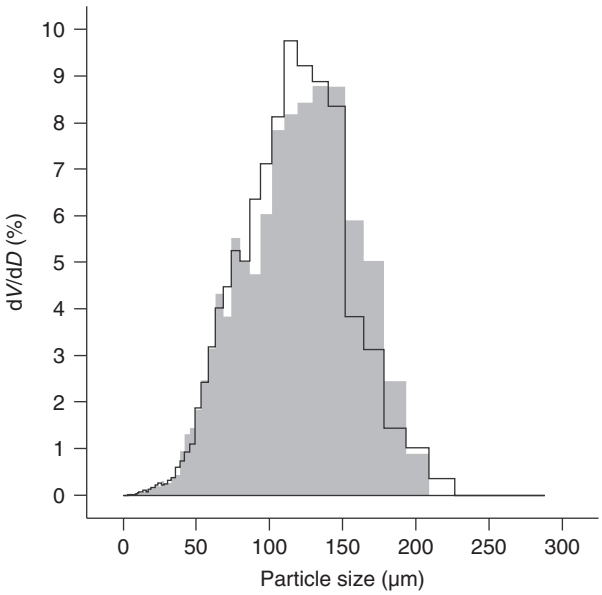

Fig. 1. Graph showing similar size distributions of particles in Phoslock (grey) and modified zeolite capping layers. Before suspension and deposition, both capping materials were passed though a 125-μm mesh to remove large particles. The median size of Phoslock particles was 104.3 μm (mean = 103.6 μm, s.d. = 38.1 μm) and that of modified zeolite particles was 101.8 μm (mean = 101.3 μm, s.d. = 36.4 μm). The grain-size composition (% volume) was measured with a Galai particle analyser (Galai Cis–100; Galai Productions, Migdal Haemek, Israel).

Sediment sampling and incubation

We collected 12 sediment cores from Lake Rotorua at 17-m water depth (lake water temperature = 14°C) in June 2006 using a Jenkins corer and clear acrylic tubes (41 $cm^2 \times 20$ cm). The sediment cores and ~50 L of surface lake water were transported to a constant-temperature laboratory (18°C) within 2 h. In the laboratory, we wrapped the sediment-filled part of the tubes (~13 cm) with black foil to avoid illumination of subsurface sediment and submerged them in aerated lake water.

Measurement setup, capping material dosing and microelectrode profiling

Series 1

To make capping layers of the three materials, we filled each of 15 50-mL vials (5.93 $cm^2 \times 11.5$ cm) with 25 cm^3 fine sand (Ajax Chemicals, http://ajaxchem.com) and 20 mL Lake Rotorua water (conductivity = 97.3 $\mu S\,cm^{-1}$ at 17.2°C, pH = 6.9). Thereafter, we added 5-mL suspensions of five doses of each of the capping materials to the vials and left the suspended mineral particles (Phoslock, modified zeolite) or alum floc to settle for 12 h. We then measured one microprofile of apparent hydrogen-gas diffusivity in each vial from a position above the capping layer into the underlying fine sand.

To create realistic thicknesses of sediment capping layers, we calculated doses according to usual lake applications (Cooke *et al.* 1993). The upper 4-cm-thick layer of Lake Rotorua sediment contained ~2.9 g TP m^{-2} (TP, total phosphorus). Assuming that 100 g Phoslock removes 1–1.2 g P, the treatment

required to bind this P would be ~300 g Phoslock m^{-2}. To cover a range of possible applications, we used the following doses for the Phoslock and modified zeolite treatments: 135, 270, 405, 540 and 674 g m^{-2}. Addition of the mineral-based capping materials to the lake water in the vials affected the pH of the lake water to differing degrees. The lowest doses of Phoslock and modified zeolite decreased the pH from 6.9 to 6.8 and 4.7, respectively. The high dose caused a pH of 6.7 (Phoslock) and 4.4 (modified zeolite).

Following Cooke *et al*. (1993), an application of 290 g m^{-2} Al to the lake sediment would bind ~2.9 g TP m^{-2}. Adding $Al_2(SO_4)_3 \times 16\,H_2O$ at this rate to the small volume (25 mL) of lake water overlying the sediment in the vials decreased the lake water pH below 4.2 and, consequently, no alum floc was formed. Preliminary tests showed that in Lake Rotorua water, alum floc forms under conditions of pH >4.2. Maximum formation of $Al(OH)_3$ occurs in the 6–8 pH range (Cooke *et al*. 1993). Consequently, we applied a range of much lower doses: 17, 34, 51, 67 and 84 g $Al_2(SO_4)_3 \times 16\,H_2O$ m^{-2}, equivalent to 1.5, 2.9, 4.4, 5.7 and 7.2 g Al m^{-2}. The lowest dose decreased the lake water pH to 4.43; the highest dose caused a pH of 4.06. No flocculation occurred in the vials that received aluminium sulfate at a rate of 67 and 84 g m^{-2}. Addition of $NaHCO_3$ buffer raised the pH to 7.02 (67 g m^{-2}) and 6.05 (84 g m^{-2}) and initiated flocculation in these vials.

Series 2

After the Lake Rotorua sediment cores had been submerged in the laboratory for 24 h, we raised them so that the upper rims of the acrylic tubes were above the surface of the water bath. We then exchanged 50 mL of lake water in nine of the tubes with lake water to which capping materials were added. Each of the three capping materials was applied at three doses: 200, 400 and 600 g m^{-2} (0.77, 1.54 or 2.31 g capping material in 50 mL of lake water). Before application, $NaHCO_3$ buffer was added to those 50-mL aliquots containing modified zeolite or aluminium sulfate to raise the lake water pH and to initiate the formation of alum floc. As a control, three tubes received 50 mL of lake water that contained no capping materials. The capping materials were allowed to settle for 12 h. Thereafter, we submerged all tubes to mix the sediment overlying lake water with the water in the incubation bath for another 12 h, after which we commenced the measurements. We measured two $[O_2]$ microprofiles in each of the 12 sediment cores. Microprofiles of pore water pH were measured only in the sediment cores treated with 200 and 600 g m^{-2} capping material and in two reference cores.

Parameter estimation and data analysis

We used the measured apparent hydrogen gas diffusivity to derive the apparent O_2 diffusivity. The rates of the diffusive O_2 uptake of the reference sediment and of those sediments capped with mineral-based capping materials were derived from the $[O_2]$ gradient in their diffusive boundary layers with Fick's law of diffusion. For a one-dimensional case, this is $J = -D_0 \delta C(x)/\delta x$, where J is the diffusion flux, D_0 is the free-solution diffusion coefficient of O_2 and $C(x)$ is the concentration at depth x. The rate of the diffusive O_2 uptake of the sediment capped with alum floc, however, was derived from the $[O_2]$ gradient in the capping layer, using the measured apparent diffusivity, ϕD_S, of the capping layer and the equation $J = -\phi D_S \delta C(x)/\delta x$.

Results

Series 1: capping layer thickness and apparent gas diffusivity

The capping layers derived from Phoslock doses of 135–674 g m^{-2} measured 0.6–3.1 mm (Fig. 2). Similar-dose capping layers of modified zeolite were significantly thicker (1.5–3.9 mm *t*-test, $P = 0.001$). Addition of 17–84 g m^{-2} aluminium sulfate to the vials resulted in 1.6–6.0-mm-thick capping layers of alum floc.

The apparent O_2 diffusivity (hereafter referred to as apparent diffusivity) of the Phoslock and the modified zeolite capping layers decreased with depth, whereas that of alum remained nearly constant with depth in the layer (mean $= 1.58 \pm 0.02 \times 10^{-5}$ $cm^2\,s^{-1}$, $n = 5$, Fig. 3). The decrease in apparent diffusivity was most pronounced in Phoslock capping layers; the apparent diffusivity of its uppermost layer was $1.14 \pm 0.06 \times 10^{-5}$ $cm^2\,s^{-1}$ ($n = 4$) and decreased towards the surface of the underlying sand by minimal 17% (135 g m^{-2}) and maximal 59% (540 g m^{-2}). A similar trend was observed for modified zeolite capping layers; their diffusivity decreased from $1.16 \pm 0.15 \times 10^{-5}$ $cm^2\,s^{-1}$ in the uppermost layer by 42 ± 9% ($n = 5$).

Series 2: capping layer thickness

By fitting an exponential regression model to the dose–thickness relationships seen in Series 1 (Phoslock: $R^2 = 0.998$, modified zeolite: $R^2 = 0.935$), we estimated that the doses applied in Series 2 (200, 400 and 600 g capping material m^{-2} sediment) should have resulted in 0.80, 1.5 and 2.7 mm capping layers of Phoslock and 1.3, 2.1 and 3.3 mm capping layers of modified zeolite (Table 1). Inspection of the $[O_2]$ profiles (Fig. 4) for discontinuities indicating the capping layer–sediment interface revealed that the thicknesses of the Phoslock and modified zeolite capping layers that derived from doses of 200 g m^{-2} were within the estimated range of 0.8–1.3 mm. The thicknesses of capping layers that derived from doses of 400 and 600 g m^{-2} could not be estimated using $[O_2]$ microprofiles because the majority of the $[O_2]$ gradient was within the capping layer so that no clear discontinuity in the $[O_2]$ profile was apparent at the capping layer–sediment boundary.

Because the doses of alum applied to the lake sediment cores were outside the range of those used in Series 1, we could not reliably estimate the thicknesses of the resulting capping layers. Extrapolation of the observed dose–layer thickness relationship suggested that capping layers from the lowest dose (200 g m^{-2}) would measure >6 mm, and the higher doses would be correspondingly thicker.

Series 2: $[O_2]$ gradients and O_2 flux

Reference sediment

The reference sediment consumed 492 ± 188 μmol O_2 m^{-2} h^{-1} ($n = 6$) (Table 1). The thickness of the diffusive boundary layer separating the reference sediment from the bulk water

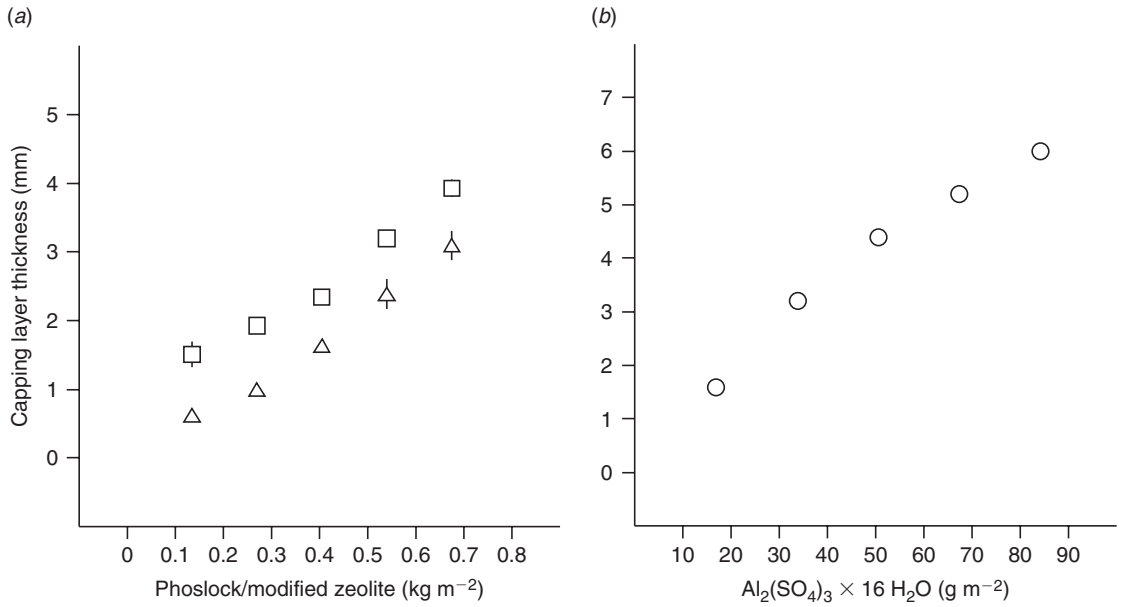

Fig. 2. Series 1. Graph showing the relationship between dose of (*a*) Phoslock (triangles) and modified zeolite (squares), and (*b*) aluminium sulfate (circles) and the thickness of their capping layers.

phases was ~0.8 mm. From the sediment surface, O_2 became undetectable at 4.4 ± 0.8 mm depth ($n = 6$, Fig. 5); the pore water O_2 saturation decreased from 68.0 ± 6.2% at the sediment–water interface to <5% at 2.3 ± 0.5 mm depth.

Mineral based capping materials

Relative to the reference sediment, capping layers of Phoslock and modified zeolite derived from the lowest dose (200 g m^{-2}) decreased the O_2 saturation at the sediment surface (now the capping layer–sediment interface) to 36–37% and 8–22% and the sediment O_2 penetration to 3.4–4.2 mm and 1.8–3.8 mm, respectively (Fig. 4). The higher dose of 400 g m^{-2} Phoslock and modified zeolite decreased the O_2 saturation at the capping layer–sediment interface to 3–4% and 2% and the sediment O_2 penetration to 2.0–2.2 and 0.8–1.4 mm, respectively. Application of 600 g capping material m^{-2} placed most of the [O_2] gradients into the capping layers so that the pore water O_2 saturation at the capping layer–sediment interfaces were ~1% and the sediment O_2 penetration 0.6–1.0 mm.

We found a similar trend for both mineral-based capping materials with respect to effects of their capping layers on sediment O_2 flux. Increasing the capping material dose from 200 to 400 g m^{-2} raised the O_2 flux from 95 to 138% (Phoslock) and from 165 to 201% (modified zeolite) of the reference O_2 flux (Table 1). A further dose increase to 600 g m^{-2}, however, lowered the O_2 flux to 114% (Phoslock) and 134% (modified zeolite) of the reference O_2 flux.

Alum

The high apparent diffusivity of the alum floc (see above) resulted in deep O_2 penetration and lower O_2 gradients in the high-dose alum capping layers (Fig. 4). The exact thickness of the floc could not be estimated from the [O_2] profile because no distinct discontinuity was apparent except in one profile and so the oxygenation of the capping layer underlying sediment remained uncertain. Our estimate of >6 mm of capping layer from the lowest alum dose (see above) would place the oxic–anoxic interface within the capping layer. However, the discontinuity in one of the two profiles measured across this capping layer indicated that, at this point of measurement, the capping layer was only 2.4 mm thick. Capping layers derived from doses of 200, 400 and 600 g m^{-2} decreased the O_2 flux from 92 to 31% of the reference flux (Table 1).

Series 2: pH

The pH in the reference sediment decreased from 6.8 at the surface to 6.4 at a depth of 2 mm, the depth corresponding to the steep part of the O_2 gradient (Fig. 5). Below this depth, the pH was constant for ~1 mm in a region where [O_2] approached zero. Deeper in the core sediment profile, the pH gradually increased, reaching 6.5 at 9 mm, the maximum depth measured.

The low-dose capping layer of Phoslock did not affect the shape of pH profile measured in the reference sediments: the depth of the pH minimum relative to the sediment surface was still ~2 mm. In contrast, the thicker low-dose capping layer of modified zeolite raised the depth of the pH minimum towards the sediment surface by ~1 mm so that the majority of the pH gradient occurred within the capping layer (Fig. 6).

A capping layer derived from addition of 600 g m^{-2} Phoslock not only altered the shape of the pH profile but also shifted the position of the minimum upwards out of the sediment and into the capping layer. Further down, the pH increased towards the capping layer–sediment interface and then further decreased towards the maximum depth measured of 9 mm. The high-dose capping layer of modified zeolite caused a similar upwards shift

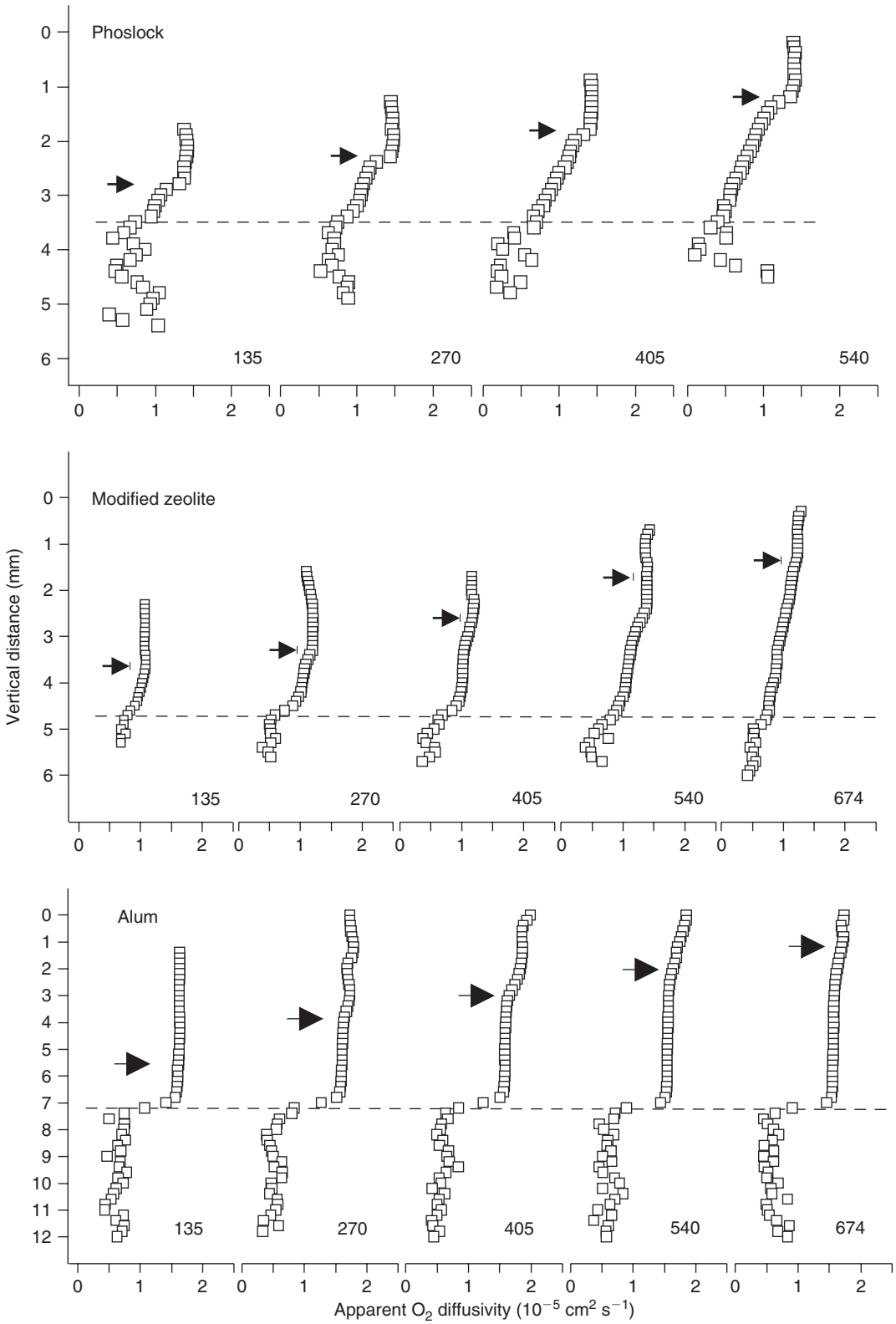

Fig. 3. Series 1. Microprofiles of apparent O_2 diffusivity through capping layers of Phoslock, modified zeolite and alum. Arrows indicate the approximate position of the capping layer surface. Numbers (135, 270, 405, 540, 674) are quantities ($g\,m^{-2}$) of capping materials added to each vial to create layers of different thickness.

Table 1. Capping layer properties, diffusive O_2 flux (J), sediment oxygen penetration depth (OPD) and pore water [O_2] at the sediment surface (reference sediment) or the sediment–capping layer interface

Dose ($g\,m^{-2}$)	Median capping layer particle size (μm)	Layer thickness (mm)	J ($\mu mol\,O_2\,m^{-2}\,h^{-1}$)	Sediment OPD (mm)	$[O_2]_{z0}$ (% saturation)
Reference sediment ($n = 6$)					
0	–	–	492 ± 188	4.4 ± 0.8	68.0 ± 6.2
Phoslock					
200	104.34	0.8	437/498	4.2/3.4	36.9/36.2
400		1.5	737/622	2.0/2.2	3.4/3.7
600		2.7	502/621	1.0/0.6	1.3/0.6
Modified zeolite					
200	101.75	1.3	774/848	3.8/1.8	21.9/7.8
400		2.1	1041/941	1.4/0.8	2.2/1.9
600		3.3	629/685	1.0/0.6	0.5/0.7
Alum					
200	–	>6	521/385	–	–
400		–	228/193	–	–
600		–	183/124	–	–

of the pH minimum but a much steeper decrease in pH. The pH at the minimum decreased by 0.3 and 0.5 units compared with the reference sediment. In contrast to the mineral-based capping materials, the alum floc decreased the pH substantially by ~1 unit (low dose) and 2.2 units (high dose).

Discussion

Our results demonstrate that capping layers of the three materials raised the oxic–anoxic interface and the associated pH minimum from within the sediment to near or above the capping layer–sediment interface and so decreased the thickness of the oxic sediment layer and the oxygenation of its pore water and altered the sediment O_2 uptake rates. These effects were functions of the thickness and apparent diffusivity of the capping layer. The apparent diffusivities of alum capping layers were higher than those of mineral-based capping layers. However, alum capping layers were at least five times thicker than those derived from similar-dose applications of the mineral-based capping materials. That is, although exhibiting higher apparent diffusivity, alum capping layers will not necessarily differ in their impedance of the sediment–water solute exchange from similar-dose capping layers of the mineral-based capping materials.

The steep [O_2] gradient in the uppermost sediment layer results both from a depth-dependent aerobic activity and the impedance of the sediment and the diffusive boundary layer to the transport of O_2 molecules. The capping layers increased the distance for the diffusion of molecular O_2 from the bottom water to the sediment pore water. This has consequences for the complex kinetics of the O_2-consuming processes: aerobic heterotrophic respiration by benthic microorganisms, leading to mineralisation of organic matter in the uppermost sediment layer (hereafter O_2 respiration), and microbial and non-biological catalysed oxidations of reduced products from anaerobic mineralisation (NH_4^+, H_2S, Fe^{2+} and Mn^{2+}) at the oxic–anoxic interface. Increasing the capping material doses from 200 to $600\,g\,m^{-2}$ shifted the oxic–anoxic interface from a position in the sediment into the capping layer. Such a shift can change the share of the O_2 consumption processes described above on the total sediment O_2 consumption; that of the O_2 respiration presumably decreased, whereas that of microbial and non-biological catalysed oxidations of reduced compounds increased. In organic matter-rich sediment in which the latter oxidation processes dominate the O_2 consumption, an upwards shifting oxic–anoxic interface may not necessarily translate into a decrease in the total sediment O_2 uptake; this is because the oxidation zone for reduced compounds may simply migrate closer to the sediment surface as the sediment O_2 supply decreases (Boudreau and Jørgensen 2001). Our flux estimates indicated that this may have applied to the low-dose capping layer of Phoslock (~1 mm thick); this layer decreased both the [O_2] at the sediment–capping layer interface and the sediment O_2 penetration, but not the rates of the sediment O_2 uptake (Table 1). However, an increase in the thickness of both mineral-based capping layers increased, and in the case of modified zeolite approximately doubled, the O_2 flux compared with that of the reference sediment. This increase may be explained, first, by benthic O_2 oxidation of reduced solutes that in the reference sediment may have been oxidised in the overlying water rather than in the sediment and, second, by a stimulation of anaerobic organic carbon mineralisation resulting in a higher rate of the production of reduced byproducts for subsequent abiotic oxidation. The lower capping layer boundary may have constrained the upwards diffusion of reduced solutes owing to its low apparent diffusivity (Fig. 3), whereas the high apparent diffusivity of the uppermost capping layer supported the supply of O_2 for the oxidation of these solutes. The capping layer gradients in apparent diffusivity were due to an increase in particle size towards the capping layer–sediment interface. Larger particles settled first at the sediment surface, making a layer of relatively low apparent diffusivity, whereas smaller particles settled last, causing the high diffusivity of the uppermost layer.

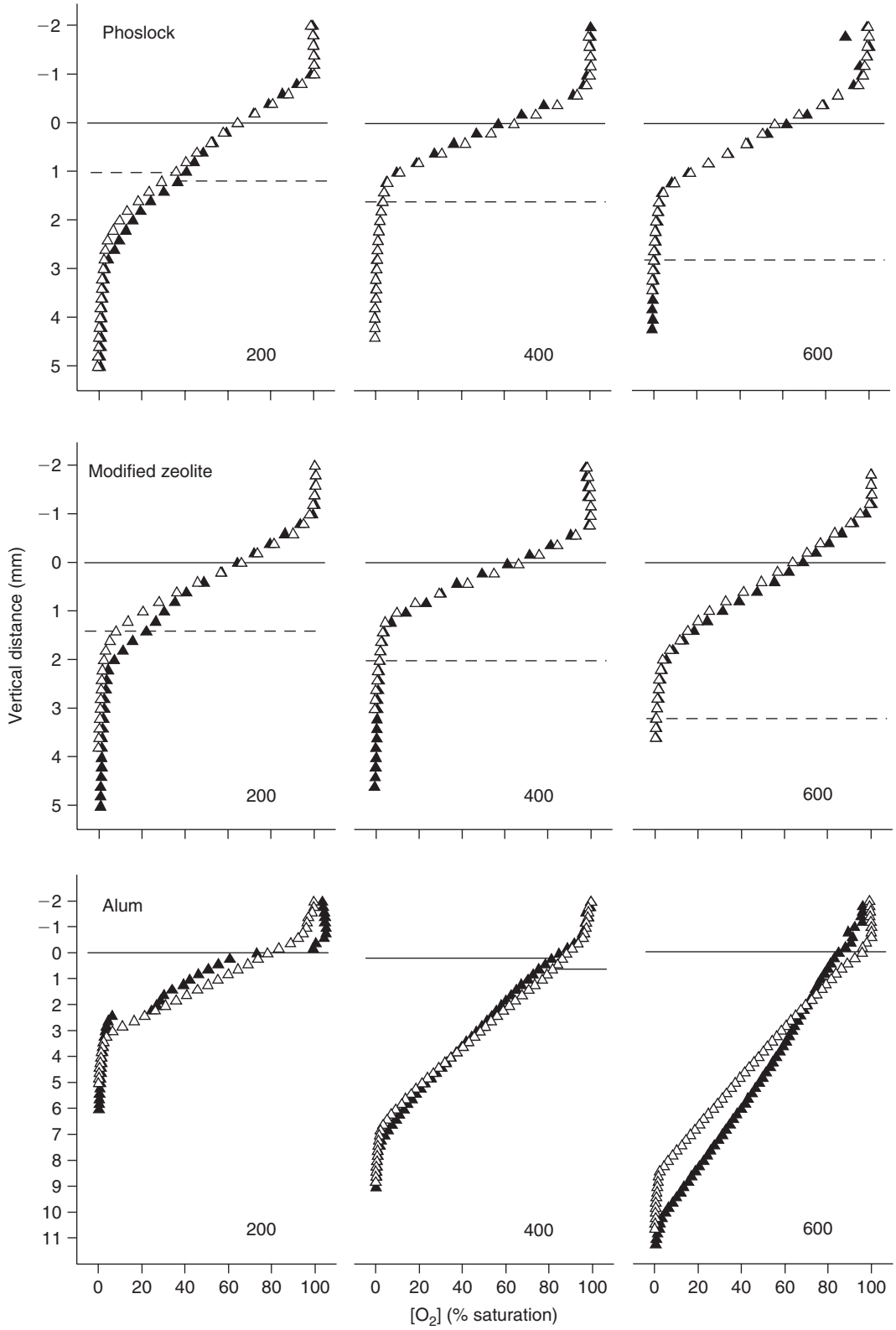

Fig. 4. Series 2. Vertical [O_2] microprofiles of lake sediment capped with layers of Phoslock, modified zeolite and alum. Two profiles (solid and hollow triangles) were measured in each of nine cores. Numbers (200, 400 and 600) are quantities ($g\,m^{-2}$) of capping materials added to each sediment core to create layers of different thickness. Solid and dashed lines indicate approximate positions of the surfaces of the capping layers and the sediments respectively. Dashed line not shown when position of the sediment surface was uncertain.

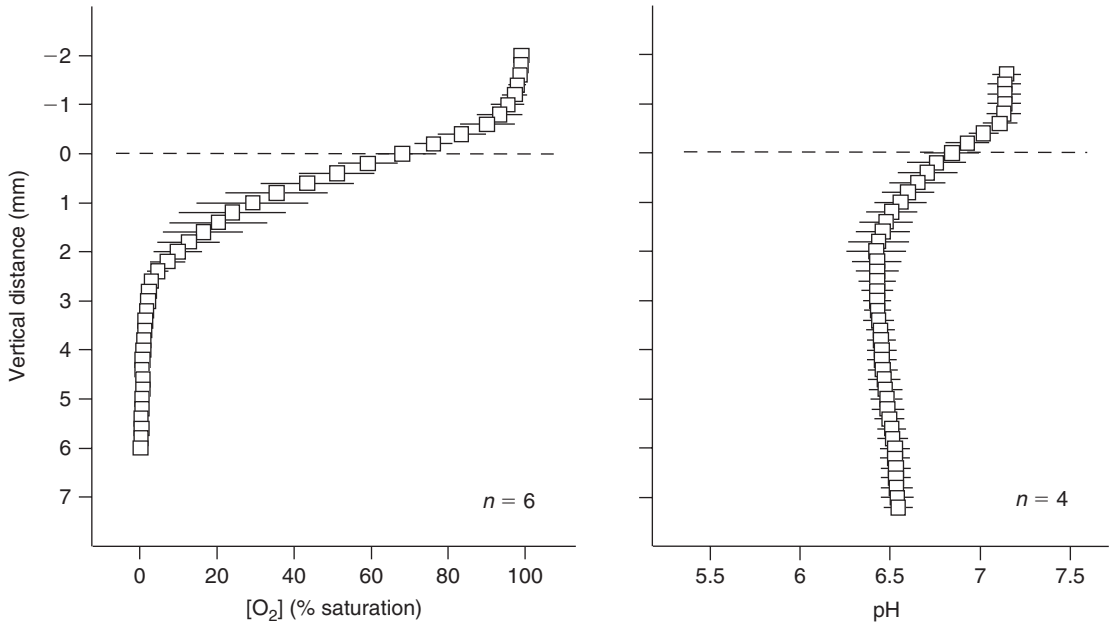

Fig. 5. Series 2. Average vertical microprofiles of $[O_2]$ (means ± s.d., $n = 6$) and pH ($n = 4$) in Lake Rotorua sediment. The dashed line indicates the sediment surface.

A further increase in thickness of the mineral-based capping layers shifted the oxic–anoxic interface into the capping layer, impeding O_2 respiration in the sediment and, presumably, the microbially catalysed oxidation of reduced solutes if the physicochemical conditions in the capping layer were suboptimal for microbial metabolism. If this was the case, then the non-biological oxidation of reduced solutes by O_2 was the main process to counteract the loss of these solutes to the bottom water. A shift of the oxidation zone was also indicated by the measured pH profiles. The steep decrease in pH in the uppermost sediment (Fig. 5) is a feature of many diagenetic active sediments (marine and freshwater) and usually ascribed to oxidation of upward-migrating reduced compounds (e.g. NH_4^+, Mn^{2+}, Fe^{2+} and HS^-) and, to a lesser extend, to carbonic acid production by O_2 respiration (Jourabchi *et al.* 2005). The reversal in the pH-versus-depth trend in the deeper sediment indicates reductive dissolution of iron and manganese (hydr)oxides coupled to organic matter and sulfide oxidation. We showed that the high-dose capping layers of the mineral-based capping materials shifted the position of the pH minimum upwards out of the sediment and into the capping layer (Fig. 6), confirming that reduced solutes diffused upwards into the capping layer to be oxidised by O_2.

In contrast to the mineral-based capping layers, the alum capping layers gradually decreased the sediment O_2 uptake rates with increasing dose. The apparent diffusivity of the alum floc was high and constant with depth in the capping layer, which may have supported O_2 consumption processes beneath the low-dose capping layer, explaining why the relatively thick layer did not alter the sediment O_2 uptake substantially. However, further increases in the thickness of the capping layers must have decreased the sediment O_2 consumption and, consequently, the O_2 flux. The alum capping layers cannot retain upwards-diffusing reduced solutes as proposed for the mineral-based capping layers because their apparent diffusivity was high throughout the layer.

The pH of the capping layers derived from alum and modified zeolite (high dose) was lower than that of the upper reference sediment or similar-dose capping layers of Phoslock. We believe that such decrease was due to the generation of protons by the capping layer rather than a result of O_2-consuming processes. Low pH in the capping layer will support the diffusive loss of reduced sulfur from the underlying sediment into the bottom water. At a pH of <5, dissolved reduced sulfur occurs in the form of H_2S gas, which will diffuse across the capping layer into the overlying lake water. Low pH will not only affect the speciation of reduced sulfur but also that of Al in the capping layer. Between pH 6 and 8, most of the Al occurs in the form of solid $Al(OH)_3$. As pH falls below pH 6.0, other forms, including $Al(OH)_2^+$ and Al^{3+}, become important; these are toxic in varying degrees, particularly dissolved Al^{3+} (Cooke *et al.* 1993; and literature cited therein).

It is important to emphasise that the results of our study cannot readily be used to predict consequences of large-scale applications of the tested capping materials, but rather show principal responses of diagenetically active sediment. Predicting *in situ* effects is not straightforward because capping layers will vary in thickness if particle/floc deposition is uneven or the bottom water flow resuspends and redistributes the deposited material. Both the alum floc and the uppermost fraction of the mineral-based capping layers may be removed from the surface of elevated sediment by even slow bottom water currents and this material may eventually accumulate in sediment depressions. Furthermore, sediment infauna can, through particle mixing and burrow irrigation (bioturbation), modify the distribution of the sediment-capping material; this mixing was not observed in our study but will certainly be of importance in sediments more

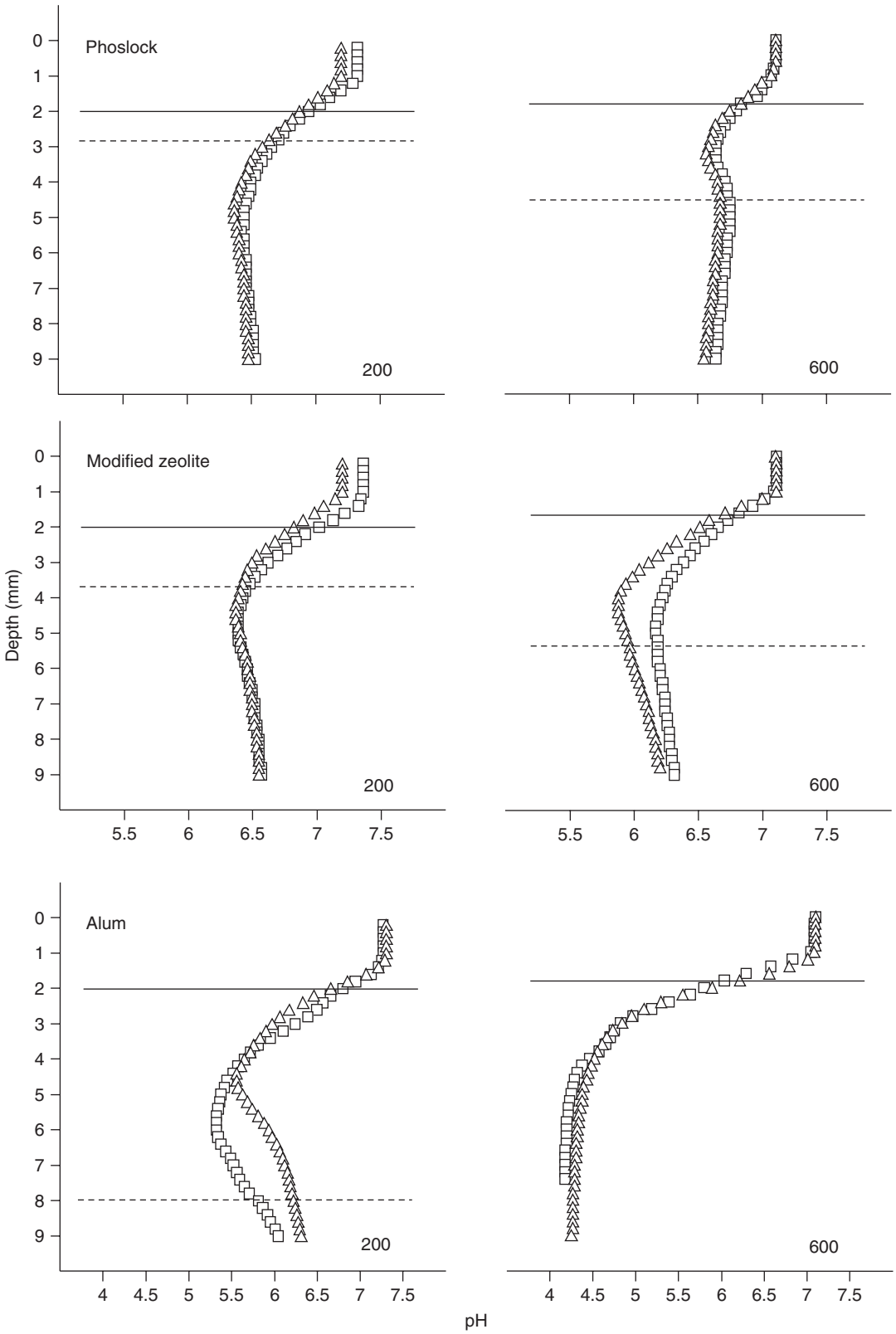

Fig. 6. Series 2. pH microprofiles of Lake Rotorua sediment capped with layers of Phoslock, modified zeolite and alum. Numbers (200 and 600) are quantities ($g\,m^{-2}$) of capping materials added to each sediment core to create layers of different thickness. Solid and dashed lines indicate approximate positions of the surfaces of capping layers and the sediments respectively. Dashed line not shown when position of the sediment surface was uncertain.

densely populated by macroinvertebrates. Finally, the size distribution of the grains in the mineral-based capping layers, and so the apparent diffusivity of the layer, will depend on the product formulation and techniques used to apply the capping material.

Acknowledgements

I. Hawes, I. Klawonn, J. Meadows, T. Stuthridge and A. Vopel commented on earlier drafts. Scion supplied the pre-commercial formulation of modified zeolite. We are grateful for the constructive criticism of G. Douglas and one other anonymous reviewer. The New Zealand Foundation for Research, Science and Technology funded the research (CO1X0305).

References

Akhurst, D., Jones, G. B., and McConchie, D. M. (2004). The application of sediment capping agents on phosphorus speciation and mobility in a sub-tropical dunal lake. *Marine and Freshwater Research* **55**, 715–725. doi:10.1071/MF03181

Boudreau, B. P., and Jørgensen, B. B. (2001). 'The Benthic Boundary Layer.' (Oxford University Press: Oxford.)

Burdige, D. J. (2006). 'Geochemistry of Marine Sediments.' (Princeton University Press: Princeton, NJ.)

Colella, C. (1999). Natural zeolite in environmentally friendly processes and applications. *Studies in Surface Science and Catalysis* **125**, 641–655. doi:10.1016/S0167-2991(99)80270-5

Cooke, G. D., Welch, E. B., Peterson, S. A., and Newroth, P. R. (1993). 'Restoration and Management of Lakes and Reservoirs.' (CRC Press: Boca Raton, FL.)

Douglas, G. B. (2002). Remediation material and remediation process for sediments. US Patent: US 6530383.

Douglas, G. B., Adeney, J. A., and Robb, M. S. (1999). A novel technique for reducing bioavailable phosphorus in water and sediments. In 'Proceedings of the International Association Water Quality Conference on Diffuse Pollution'. pp. 517–523.

Jacobs, P. H., and Förstner, U. (1999). Concept of subaqueous capping of contaminated sediments with active barrier systems (ABS) using natural and modified zeolites. *Water Research* **33**, 2083–2087. doi:10.1016/S0043-1354(98)00432-1

Jourabchi, P., Van Cappellen, P., and Regnier, P. (2005). Quantitative interpretation of pH distributions in aquatic sediments: a reaction–transport modeling approach. *American Journal of Science* **305**, 919–956. doi:10.2475/AJS.305.9.919

Reitzel, K., Hansen, J., Jensen, H. S., Andersen, F. O., and Hansen, K. S. (2003). Testing aluminum addition as a tool for lake restoration in shallow, eutrophic Lake Sonderby, Denmark. *Hydrobiologia* **506–509**, 781–787. doi:10.1023/B:HYDR.0000008624.54844.2D

Reitzel, K., Hansen, J., Andersen, F. O., Hansen, K. S., and Jensen, H. S. (2005). Lake restoration by dosing aluminum relative to mobile phosphorus in the sediment. *Environmental Science & Technology* **39**, 4134–4140. doi:10.1021/ES0485964

Revsbech, N. P., Nielsen, L. P., and Ramsing, N. B. (1998). A novel microsensor for determination of apparent diffusivity in sediments. *Limnology and Oceanography* **43**, 986–992.

Robb, M. R., Greenop, B., Goss, Z., Douglas, G. B., and Adeney, J. A. (2003). Application of Phoslock™, an innovative phosphorus binding clay, to two Western Australian waterways – preliminary findings. *Hydrobiologia* **494**, 237–243. doi:10.1023/A:1025478618611

Rowe, G. T., Clifford, C. H., Smith, K. L., and Hamilton, P. L. (1975). Benthic nutrient regeneration and its coupling to primary productivity in coastal waters. *Nature* **255**, 215–217. doi:10.1038/255215A0

Sakadevan, K., and Bavor, H. J. (1998). Phosphate adsorption characteristics of soils, slags and zeolite to be used as substrates in constructed wetland systems. *Water Research* **32**, 393–399. doi:10.1016/S0043-1354(97)00271-6

Stumm, W., and Morgan, J. J. (1996). 'Aquatic Chemistry – Chemical Equilibria and Rates in Natural Waters.' (John Wiley & Sons: New York.)

Welch, E. B., and Cooke, G. D. (1999). Effectiveness and longevity of phosphorus inactivation with alum. *Lake and Reservoir Management* **15**, 5–27.

Manuscript received 23 April 2008, accepted 24 September 2008

Limnol. Oceanogr., 51(4), 2006, 1801–1812

Photosynthetic performance of benthic microbial mats in Lake Hoare, Antarctica

Kay Vopel[1]
National Institute of Water and Atmospheric Research, P.O. Box 11-115, Hamilton, New Zealand

Ian Hawes
World Fish Center, Nusa Tupe, P.O. Box 77, Western Province, Solomon Islands

Abstract

We measured in situ photosynthesis of benthic microbial mats at various depths in Lake Hoare, a permanently ice-covered lake of the McMurdo Dry Valleys, Antarctica, using oxygen (O_2) microelectrodes. We further investigated the vertical distribution and activity of pigments in the microbial mats using an imaging pulse-amplitude-modulated fluorometer. Microbial mats to at least 16.6-m water depth are net producers of O_2 during the summer period. Net O_2 production ranges from 100–500 μmol m^{-2} h^{-1} at incident downwelling irradiances of photosynthetically active radiation (PAR) of 1.0–4.6 μmol quanta m^{-2} s^{-1}. Photosynthesis of mat-forming cyanobacteria and diatoms occurs at all lake depths at or close to maximum efficiency. We measured absorption by the pigment arrays at a single water depth and, by assuming that absorption is water-depth invariant, we estimated an area-specific maximum community quantum yield of 0.073 mol carbon per mol photons. A community compensation irradiance of 0.1 μmol quanta m^{-2} s^{-1} was estimated, reflecting extreme shade acclimation. These results confirm estimates previously derived from laboratory gas-exchange measurements and imply that even minor changes in the intensity of the incident downwelling irradiance of PAR caused by, for example, changes in the transparency of the ice cover or the optical properties of the water column can significantly alter rates of benthic carbon fixation. In situ measurements were confined to mats with flat surfaces. Laboratory measurements at the surface of mats with pinnacled surfaces revealed a complex small-scale chemical structure at the mat–water interface.

The largest ice-free region of Antarctica, the Dry Valley Region of Southern Victoria Land, is among the coldest and driest deserts in the world (Heywood 1984). The dry valley mean annual temperature ranges from −14.8°C to −30.0°C (Doran et al. 2002*a*). The low mean annual temperature allows perennial, 3–6-m-thick ice covers to persist on numerous meltwater lakes in the valley systems. The ice covers have profound effects on these lakes: they eliminate turbulent mixing of the water column by wind-generated currents, reduce light penetration, and restrict gas exchange between the atmosphere and the water column. Among the unique features of these lakes that have developed as a consequence of ice cover is the oxygen (O_2) supersaturation of the water column (Parker et al. 1981; Craig et al. 1992). A second unusual feature is the occurrence of modern and nascent stromatolites: laminated photosynthetic communities, dominated by cyanobacteria, which cover much of the lake floors (Wharton et al. 1983; Hawes and Schwarz 1999).

Whereas numerous studies of photosynthetic production in the dry valley lakes have focused on planktonic microbial communities (e.g., Vincent 1981; Priscu et al. 1987; Dore and Priscu 2001), few studies have dealt with benthic communities (Wharton et al. 1994; Hawes and Schwarz 1999, 2000; Hawes et al. 2001). The study of Wharton et al. (1994) revealed evidence for benthic photosynthesis. These authors found significant differences in pore water [O_2] profiles measured in sediment cores taken from Lake Hoare in January and October; they suggested that this difference is due to a seasonal cycle resulting from the long photoperiod and photosynthesis by mat-forming benthic microbial communities. Subsequent laboratory gas-exchange measurements demonstrated that mats taken in Lake Hoare from water depths of up to 22 m are capable of photosynthesizing at the low irradiance they would experience under ambient conditions (Hawes and Schwarz 1999, 2000). Hawes and Schwarz (1999) suggested that, in this diffusion-dominated lake, benthic biomass accumulation is favored by retention of nutrients in close proximity to growing cells, with minimal expenditure of energy in swimming or loss to grazers. In a modeling exercise, Hawes et al. (2001) then used their experimentally derived observations of mat photosynthesis and respiration, with data on incident downwelling irradiance of photosynthetically active radiation (PAR; *see Table 1*) and the optical properties of the ice and water column (Howard-Williams et al. 1998), to predict net photosynthetic production from October to February, net respiration at other times, and a maximum annual rate of carbon fixation of 12 g carbon m^{-2}, equating to approximately 0.1–4-mm vertical accumulation of mat each year. Finally, using the experimental observations of Hawes and Schwarz (1999, 2000) and a mathematical model, Moorhead et al.

[1] Corresponding author (k.vopel@niwa.co.nz).

Acknowledgments

R. Ellwood assisted in the field. Two anonymous reviewers, the Associate Editor R. N. Glud, P. Doran, C. Howard-Williams, J. Meadows, and A. Vopel commented on an earlier draft.

The New Zealand Foundation for Research, Science and Technology (CO1605), Antarctica New Zealand, and the McMurdo Dry Valley Long Term Ecological Research Program of the U.S. National Science Foundation (OPP–9814972) funded and provided facilities and support for the research.

Table 1. Abbreviations.

Symbol	Definition
ϕ	Mat porosity
ϕ_p	Quantum yield of charge separation in photosystem complex II
ΔF	Variable fluorescence (the difference between F_0 and F_m or F and F'_m)
AOI	Area of interest
D_0	Free-solution diffusion coefficient ($cm^2\ s^{-1}$)
DBL	Diffusive boundary layer
D_S	Sediment diffusion coefficient ($cm^2\ s^{-1}$)
E_d	Incident downwelling irradiance of photosynthetically active radiation (mol quanta $m^{-2}\ s^{-1}$)
E_k	Irradiance above which photosynthesis is light saturated (mol quanta $m^{-2}\ s^{-1}$)
ETR	Rate of photosynthetic electron transport between photosystem complex II and I (mol electrons $m^{-2}\ s^{-1}$)
F	Current fluorescence yield of light-adapted sample
F_0, F_m	Minimal and maximal fluorescence yield of dark-adapted sample, respectively
F'_m	Maximal fluorescence yield of light-adapted sample
J	Diffusive flux of O_2 (mol $m^{-2}\ h^{-1}$)
K_L	Diffuse attenuation coefficient of scalar irradiance (mm^{-1})
LED	Light-emitting diode
PAR	Photosynthetically active radiation (mol quanta $m^{-2}\ s^{-1}$)
PSI and PSII	Photosystem complex I and II
$rETR_{max}$	Maximum relative rate of photosynthetic electron transport between photosystem complex II and I (mol electrons $m^{-2}\ s^{-1}$)
RLC	Rapid light curve
A	Slope of irradiance versus rETR as irradiance approaches zero ([mol electrons $m^{-2}\ s^{-1}$] × [mol quanta $m^{-2}\ s^{-1}$]$^{-1}$)
σ_a	Absorption cross section of photosystem complex II

(2005) simulated whole-lake, annual net primary production of benthic microbial mats in Lake Hoare and compared these estimates to observed phytoplankton production. These authors suggested that benthic microbial mats have the capacity to fix quantities of carbon that rival or exceed carbon fixation by planktonic communities; on average, simulated benthic mat production represented >85% of the combined benthic and planktonic carbon fixation.

Moorhead et al. (2005) noted that 79–99% of the uncertainty in the behavior of their model was attributed to uncertainties in estimates of the maximum photosynthetic rate, the initial slope of photosynthetic-light response, and the maximum respiration rate. These parameters were estimated from measurements of the rate of evolution or consumption of O_2 in laboratory mat enclosures (Hawes and Schwarz 1999). Hawes and Schwarz (1999) discussed the limitations of this method and noted methodological necessities that may have altered the nutrient supply of the mats and the mat–water O_2 exchange. For example, incubating mat explants altered the thickness of the diffusive boundary layer (DBL) between the mat surface and the overlying lake water and enabled solute exchange across the cut side and bottom of the cores, which would not occur naturally. Thus, the photosynthetic parameters require confirmation under in situ conditions.

The aims of this study are to estimate in situ, for the first time, the magnitude of benthic photosynthesis in a permanently ice-covered lake of the McMurdo Dry Valleys, to reassess photosynthetic parameters, and to resolve benthic photosynthesis vertically. To do so, we measured, with the aid of surface-air-supply diving, O_2 microprofiles across the mat–water interface at various depths in Lake Hoare. To obtain supplement data to help interpret O_2 microprofiles, we investigated mat cross sections in the laboratory using an imaging pulse-amplitude-modulated fluorometer (Imaging-PAM).

Material and methods

Study site—Lake Hoare (77°38′S, 162°53′E) is a closed-basin lake near the eastern end of Taylor Valley in southern Victoria Land, Antarctica. The lake is 4.2-km long and 1-km wide, and has maximum and mean depths of 34 m and 14 m. Lake Hoare is dammed to the northeast by the Canada Glacier, which provides an inflow of glacial meltwater. Other inflow comes from Andersen Creek entering the northeast corner of Lake Hoare, and drainage is from Lake Chad in the southeast. No outflows from Lake Hoare exist, so water loss is restricted to sublimation of ice and evaporation of meltwater during summer. The average mean annual temperature at Lake Hoare between 1985 and 2000 was −17.7°C (Doran et al. 2002*a*). The ice cover of this lake is perennial, except for small areas at the lake margin that melt during most summers. The thickness of the ice cover was 3.5 m in 1983 (Wharton et al. 1993), ~5 m in 2002 (Doran et al. 2002*b*), and <4 m in 2004. There are 3 months of complete darkness during winter and 3 months of continuous light during summer. Net transmission of solar radiation through the ice cover is <1–3%, with a spectral transmission peak at wave lengths of 450–550 nm. Vertical extinction coefficients for PAR within the water column from beneath the ice to a depth of 33 m were typically 0.12–0.22 m^{-1} (Howard-Williams et al. 1998). The lake has a density-stabilized water column, with

a pronounced inflection in the density–depth profile at 13–15 m from the surface (the depth of the lake varies temporally), which divides the lake into upper and lower compartments. The upper compartment is characterized by lower concentrations of dissolved nutrients, particularly nitrate (Lizotte and Priscu 1992), higher concentrations of O_2 (0.94–1.25 mmol L^{-1} compared to 0.63–0.94 mmol L^{-1} below, Wharton et al. 1986), lower bicarbonate, and higher pH (up to 8.6 compared to 7.9 below, Cathey et al. 1981). The lake is anoxic below 25–26 m depth.

Benthic microbial mats—Benthic microbial mats in different zones of Lake Hoare differ in structure and species composition; the quantity and quality of the incident downwelling irradiance of PAR are apparently the most important factors that regulate these differences (Wharton et al. 1983). Three mat morphologies are common: moat mats, columnar lift-off mats, and prostrate mats; the surface of the last can be smooth (Fig. 1A) but surface irregularities can occur in the form of pinnacles up to 3-cm high (Fig. 1B). Columnar lift-off mats and prostrate mats comprise a matrix of filamentous cyanobacteria and pennate diatoms, whereas moat mats are dominated by cyanobacteria (Wharton et al. 1983). Lift-off mats occur in shallow under-ice environments, where both N_2 and O_2 approach their saturation concentrations. Gas ebullition within lift-off mats makes them buoyant; hence they lift away from the underlying sediment until they rise up and freeze into the ice (Wharton et al. 1986). Prostrate mats occur in deeper water where gas ebullition does not occur. Moat mats, which freeze solid during winter and experience high quantities of incident downwelling irradiance of PAR during the brief ice-free period in summer, are different than the other types; they are <3-cm thick, weakly stratified, and have smooth surfaces that follow the contours of underlying sediments and rocks.

In situ measurements—In November 2004, a surface-supplied tethered diver measured a total of 10 in situ high-resolution [O_2] profiles across the mat–water interface at four depths along a transect away from a 1-m diameter hole melted through the ice (Table 2). The profiles were measured in areas devoid of pinnacles (e.g., *see Fig. 1A*). To do so, the diver attached a Clark-type underwater O_2 microelectrode (Revsbech 1989, Unisense) to a manually operated micromanipulator (Märzhäuser Wetzlar) mounted on an aluminum post that had been driven into the lake sediment. An underwater picoammeter PA 3000U (Unisense) placed onto the sediment surface provided the polarization voltage for the O_2 microelectrode, which had an outside tip diameter of 50 μm, a 90% response time of ~1 s, and a stirring sensitivity of <2%. The diver used the micromanipulator to move the electrode in 0.2-mm increments normal to the mat surface from a position above the DBL to a depth of 6–7 mm into the mat and further in 0.5-mm increments to a maximum depth of 21 mm. After each depth interval the diver verbally relayed the electrode reading to the support person at the surface of the ice, who recorded the data.

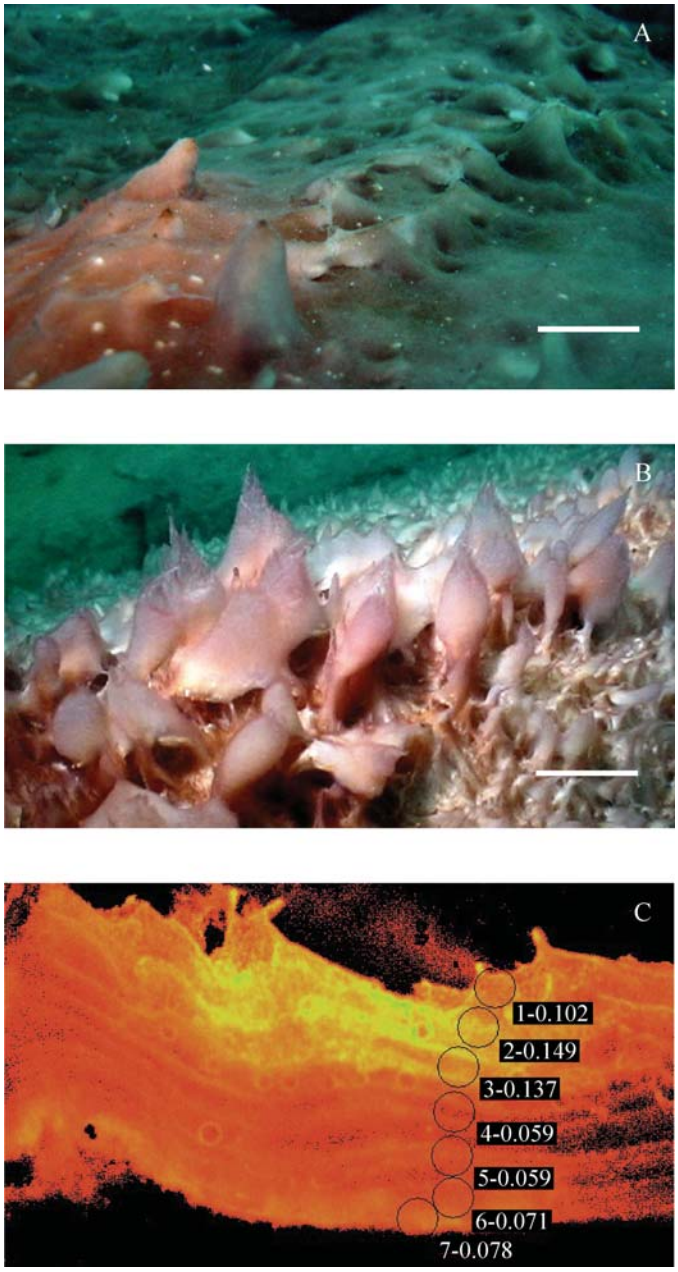

Fig. 1. (A, B) Underwater photographs of prostrate microbial mats at ~8-m water depth. The surface of the mats can be (A) smooth or (B) structured by pinnacles. Scale bars, 10 mm, apply to the center of the photograph. (C) Chlorophyll fluorescence image of a mat cross section. Areas of interest (AOI) were defined to provide a continuous vertical transect through the cross section.

We determined the downwelling irradiance of PAR incident to the surface of the microbial mat once before every in situ profiling measurement using a newly calibrated LI-COR LI 192 underwater quantum sensor and LI-189 light meter in a waterproof housing. A StowAway Tidbit miniature temperature data logger (Onset Computer Cooperation) placed onto the surface of a microbial mat at 8-m water depth measured and logged the bottom water temperature once every minute from 18 to 24 November 2004.

Table 2. In situ profiling along a depth profile away from the ice hole.

Date	Depth (m)	PAR (μmol quanta m^{-2} s^{-1})	Number of profiles
21 Nov 2004	8.1	4.6	4
22 Nov 2004	9.2	3.5	2
23 Nov 2004	16.3	2.2	2
24 Nov 2004	16.6	1.0	2

To estimate the mean spectral transmission of the ice cover, on 22 November 2004 we measured spectra immediately beneath the ice at seven random points, all well clear of the anomalous light field close to the dive hole, using a hyperspectral irradiance sensor (RAMSES-ACC-UV/VIS, TriOS). The diver then deployed the sensor at 4 m, 7 m, 10 m, and 13 m below the ice cover for estimation of spectral attenuation coefficients for downwelling irradiance by log-linear regression of irradiance-versus-depth profiles.

Sampling—To collect mats the diver cut a random series of core samples, 10 cm in diameter by 3-cm deep, of the ''active layer'' (sensu Hawes and Schwarz 1999) of microbial mats from within 3-m-diameter sampling areas, at water depths ranging from 8–16 m. These discs were carefully separated from underlying materials and transferred into an opaque polyethylene box with a watertight sealed lid. Additionally, five 150-mL water samples were collected from ~3 cm above the surface of the microbial mats at water depths of 5 m, 8 m, 12 m, and 16 m, and underwater photographs of the mat surface were taken using a Sony Cyber-shot DSCP-8 digital camera. The mat and water samples were moved to a dark tent–laboratory next to the ice hole for chemical analyses or to a lakeside laboratory for fluorescence measurements (*see* below).

Laboratory measurements—Salinity, pH, and [O_2] of the bottom water were measured with two PortaMess 913 meters, the picoammeter PA 3000U, the conductivity sensor SE 204, the pH/Pt1000 electrode SE 102 (Knick), and a Clarke-type O_2 microelectrode. Thereafter the O_2 microelectrode was mounted on a motorized micromanipulator attached to a stand to record three [O_2] microprofiles across the mat–water interface of a pinnacle mat from 12-m water depth at 200-μm resolution. The mat was fixed at the bottom of the sampling box to ensure a constant distance between micromanipulator and mat. Pieces of ice were added to the water surrounding the mat to control temperature. The profiles were measured vertically and normal to the mat surface starting at different vertical distances from a fixed position in the overlying water. The position of the mat surface was determined visually as the depth at which the tip of the microelectrode first penetrated the mat. The PC Windows program PROFIX (Unisense) controlled the stepwise movement of the micromanipulator via a motor controller and read the data from the microsensor amplifiers via an A/D converter (ADC-216USB, Unisense) that was connected to the parallel port of a personal computer. The O_2 microelectrode was calibrated in 100% air-saturated lake water and in lake water that had been deoxygenated with sodium sulfite.

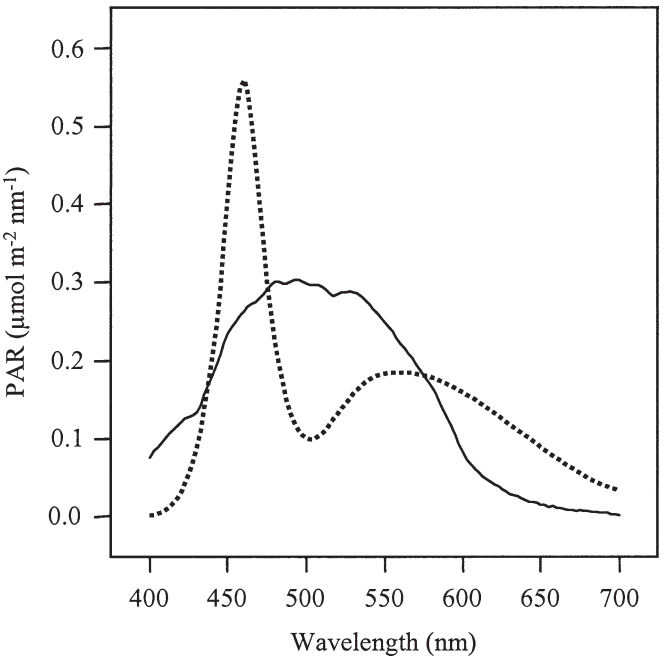

Fig. 2. Under-ice PAR spectrum (solid line) and spectrum of LED light source (dotted line).

Appropriate levels of PAR were supplied to the surface of the mat with battery-powered light-emitting diode (LED) at a previously determined distance from the surface. This distance was determined by measuring the downwelling irradiance of PAR supplied by the LED to a quantum sensor in a water-filled plastic tube so that 5 cm of water were above the sensor head. The spectrum of this irradiance was measured by submerging the hyperspectral irradiance sensor in lake water and clamping it in place a similar distance from the LED source to that used during profiling measurements. The spectrum of the under-ice downwelling irradiance of PAR was compared with that of the LED by calculating the spectrum of downwelling irradiance of PAR for 8-m water depth from ice transmission and water-column attenuation. The under-ice spectrum was dominated by a single peak spanning wave lengths of 450–570 nm. The spectrum of the LED showed two peaks within this range, at 460 nm and 560 nm, although both spectra tailed off above 600 nm (Fig. 2).

The attenuation of scalar irradiance through a microbial mat from 8-m water depth was measured by means of a scalar fiber-optic microprobe connected to a spectrometer (S2000, Ocean Optics) fitted with a diffraction grating that allowed coverage between 350 nm and 850 nm. The microprobe was constructed following Lassen et al. (1992), and the scalar detector at the tip of the probe had a diameter of 0.3 mm. The probe was inserted into the mat with the micromanipulator at an angle of 15 degrees from vertical. A blue-enhanced quartz-halogen light source provided PAR from above via a fiber-optic bundle. Spectra just above the mat surface, just below the surface, and in 1-

mm increments to a maximal depth of 9 mm were recorded. Data were integrated across four, 10-nm wavebands, 575–585, 625–635, 670–680, and 740–750 nm. The diffuse attenuation coefficient of scalar irradiance in each waveband was calculated as the rate of change of log-transformed irradiance values with depth using $K_L = -d(\ln L) \times dz^{-1}$ (Kirk 1983).

Imaging-PAM (Walz Mess- und Regeltechnik) and the saturation pulse method were used to determine the two-dimensional (horizontal or vertical) distribution and activity of pigments, measuring the minimal (F_0) and maximal (F_m) fluorescence yields of dark-adapted mat samples. For a detailed description of the saturation pulse method see, for example, Schreiber et al. (1996) or Kühl et al. (2001) and literature cited therein. Use of the Imaging-PAM to obtain spatially resolved measures of fluorescence is described by Ralph et al. (2005) and Grunwald and Kühl (2004). Measurements of F_0 were to obtain a proxy for the distribution of chlorophyll. Comparing the distribution of F_0 with that of the maximal photochemical yield, $(F_m - F_0) \times F_m^{-1}$, gave us an index of chlorophyll connectivity to photosystem complex II (PSII) electron transport chains. The primary goal of F_m measurements was to determine whether F_0 was attributable to pigments connected to competent electron transport systems. The Imaging-PAM output these two parameters as false-color images that could then be compared with photographic images of the same section.

The Imaging-PAM was set up to image an area of 30 mm × 25 mm. A millimeter scale was imaged at intervals during sampling runs. Using a scalpel, we cut 2–3-mm-thick cross sections, running for the full thickness of the active layer and each approximately 40-mm long, from freshly collected material. These sections were then laid on their sides in a Petri dish and immersed in fresh lake water. At this thickness, the laminations in the mat could be easily seen, while sufficient chlorophyll was still viewed in cross section by the Imaging-PAM to obtain acceptable fluorescence intensities (we aimed for at least 200 fluorescence units across the pigmented areas of the image) and replicable measurements. Actinic light from the Imaging-PAM was provided by a bank of blue-white LEDs. The spectrum of this light has two peaks, at 450 and 550 nm—blue and blue-green. Different absorption spectra for diatoms, which can be expected to show strongest fluorescence in response to the blue peak, and the phycoerythrin-rich cyanobacteria from Lake Hoare, which absorb maximally close to the blue-green peak (Hawes and Schwarz 2000), will result in different fluorescence responses per unit biomass for the two groups of phototrophs. Thus, while F_0 will remain a proxy for chlorophyll fluorescence in the microbial mats, care must be taken in interpreting the false color images.

The Imaging-PAM facility for defining areas of interest (AOIs) was used to provide insight to the photoadapted status of the microbial mats using rapid light curves (RLCs). First we defined AOI to provide a vertical transect through a mat cross section (Fig. 1C). The Imaging-PAM had a restricted spatial resolution when used with AOI; the diameter of the circles in Fig. 1C is ~2 mm. The instrument was therefore best suited to the thicker mats, where the size of AOI was similar to lamina thickness. Accordingly, only RLC data from mats from 12-m depth were reported. RLCs for AOIs were recorded by exposing mat cross sections to a sequence of actinic irradiances in 14 discrete PAR steps from 0 μmol quanta m^{-2} s^{-1} to 52 μmol quanta m^{-2} s^{-1}. To control for hysteresis effects, the order of PAR was not fully sequential, but ran 0, 3.6, 6.9, 10.9, 3.6, 27.9, 38, 52, 3.6, 27.9, 19, 3.6, 6.8, 0 μmol quanta m^{-2} s^{-1}. In practice, no hysteresis effects were observed. The incident downwelling irradiance of PAR supplied by blue-white LEDs (*see* above) was measured using a recently calibrated LI-COR 190 quantum sensor connected to a LI-COR Li 1000 digital meter, set to average over 5-s intervals, positioned in place of the Petri dish. Each period of actinic light lasted for 30 s, leading to a quasi-steady-state level of fluorescence, F. This period is longer than is commonly used for RLCs (10–15 s, *see* e.g., Hawes et al. 2003, Ralph and Gademann 2005). We found that a slightly longer actinic exposure of microbial mats from Lake Hoare produced more repeatable measures of variable fluorescence, ΔF, and the absence of hysteresis effects suggests that this exposure was not affecting the photoadaptive state. At the end of each actinic period, a saturation pulse of white light (0.6 s at >500 μmol quanta m^{-2} s^{-1}) was applied to determine the maximal fluorescence yield, F'_m, and the quantum yield of charge separation in PSII, $\phi_p = (F'_m - F) \times F'_m{}^{-1}$. We were unable to measure the intensity of the saturation pulse with the instrumentation available, but preliminary trials were undertaken to ensure that the width and intensity of this saturation pulse was adequate to attain maximum fluorescence yield. The photosynthetic electron transport rate (ETR) between PSII and PSI can be estimated as $ETR = \phi_p \times \sigma_a \times E_d$, where σ_a is the absorption cross section of PSII, and E_d is the incident downwelling irradiance of PAR. Assuming that σ_a is an unknown constant during the measurements, the relative ETR was estimated as $rETR = \phi_p \times E_d$ (Hofstraat et al. 1994). A modification of the Jassby and Platt (1976) equation was used to calculate the irradiance above which photosynthesis is light saturated, E_k, using least-squares regression (SigmaPlot 8.0, SPSS Inc.), as $rETR = rETR_{max} \times \tanh(E_d \times E_k^{-1})$, where $E_k = rETR_{max} \times \alpha^{-1}$ and α is the slope of the light-limited portion of the PAR versus ETR relationship. To avoid biasing the regression, repeat measures of ϕ_p at 3.6 μmol quanta m^{-2} s^{-1} in the actinic light sequence were excluded.

Analysis of in situ microprofiles—The diffusive flux (J) of O_2 from the microbial mat into the overlying bottom water was calculated from the measured steady-state O_2 gradients ($dC \times dz^{-1}$) in the DBL according to $J = -D_0\, dC \times dz^{-1}$, where D_0 is the free-solution diffusion coefficient of O_2, C is $[O_2]$, and z is depth. Values of D_0 were taken from Broecker and Peng (1974) and were recalculated to the experimental temperature with the Stokes–Einstein relation (Li and Gregory 1974). The position of the mat surface was determined by a break in the $[O_2]$ profile. This inflection is required for mass conservation in the diffusive flux, because of the shift in apparent diffusivity between the

DBL and the matrix of the mat. Vertical zones of metabolic activity were detected with a numerical procedure for the interpretation of steady-state microprofiles (Berg et al. 1998). We used one in situ [O_2] profile measured at 8.1-m and 16.6-m water depth to calculate depth profiles of volumetric net O_2 production rates (unit: nmol cm^{-3} s^{-1}) and area-specific depth-integrated net O_2 production rates for each activity zone and for the upper 21 mm of the mats (unit: μmol m^{-2} h^{-1}). Mat porosity, $\phi = 0.80 \pm 0.08$ ($n = 7$), was estimated following the approach described in Epping et al. (1999) assuming the sediment diffusion coefficient $D_S = D_0 (1 + 3 \times (1 - \phi))^{-1}$ and conservation of O_2 flux across the mat–water interface. We assumed ϕ and D_S to be depth invariant.

Results

Bottom water chemistry, attenuation of scalar irradiance within the mat, and benthic production—The bottom water salinity increased with depth from 0.30 ± 0.00 to 0.62 ± 0.04, whereas the pH decreased from 8.97 ± 0.03 to 7.59 ± 0.09 (Fig. 3A,B). The [O_2] of the bottom water was highest at 8-m depth (337 ± 16% saturation) and lowest at 16-m depth (134 ± 5% saturation, Fig. 3C). The temperature of the bottom water at 8-m water depth was constant: 0.11°C.

The diffuse attenuation coefficients of scalar irradiance, K_L, in four 10-nm wavebands (575–585, 625–635, 670–680, and 740–750 nm) were highest just below the surface of a mat from 8-m water depth (4.72, 3.83, 5.54, and 1.59 mm^{-1}) and decreased to a minimum at about 1.2-mm depth within the mat (0.005, 0.005, 0.010, and 0.0004 mm^{-1}). Further down, K_L increased asymptotically, reaching its maxima at a depth of 4 mm at 0.76, 0.64, and 0.77 mm^{-1} in the 575–585-nm, 625–635-nm, and 670–680-nm wavebands, respectively, and at 0.37 mm^{-1} at wave lengths between 740 nm and 750 nm.

The incident downwelling irradiance of PAR (hereafter irradiance of PAR) reaching microbial mats at water depths of 8.1, 9.2, 16.3, and 16.6 m varied between 1 μmol quanta m^{-2} s^{-1} to 5 μmol quanta m^{-2} s^{-1} (Table 2). Low irradiance of PAR of 1.0 μmol quanta m^{-2} s^{-1} at 16.6-m water depth caused an average O_2 efflux of 93 μmol m^{-2} h^{-1}. The efflux increased linearly with irradiance of PAR; the highest average efflux of 482 μmol m^{-2} h^{-1} was calculated from profiles measured at 8.1-m water depth under conditions of irradiance of PAR = 4.6 μmol quanta m^{-2} s^{-1} (Fig. 4). Note that estimates of O_2 flux were on the basis of area, integrated across the depth of the photosynthetic active mat plus the underlying organic material, which is different for each water depth.

Analysis of a profile measured across the upper 21 mm of a mat from 8.1-m water depth under conditions of irradiance of PAR = 4.6 μmol quanta m^{-2} s^{-1} (Fig. 5A) revealed depth-integrated net O_2 production of 441 μmol m^{-2} h^{-1}. Calculation of the O_2 flux across the DBL revealed a similar value of 493 μmol m^{-2} h^{-1}. We found three distinct zones of net O_2 production/consumption: high production (399 μmol O_2 m^{-2} h^{-1}) in the upper 3-mm-thick layer, low production (93 μmol O_2 m^{-2} h^{-1}) between 3-mm and 6-mm depth, and consumption of 51 μmol O_2 m^{-2} h^{-1} between 6-mm and 21-mm depth. Note that rates in the production profiles shown in Fig. 5 are given per volume of mat/sediment.

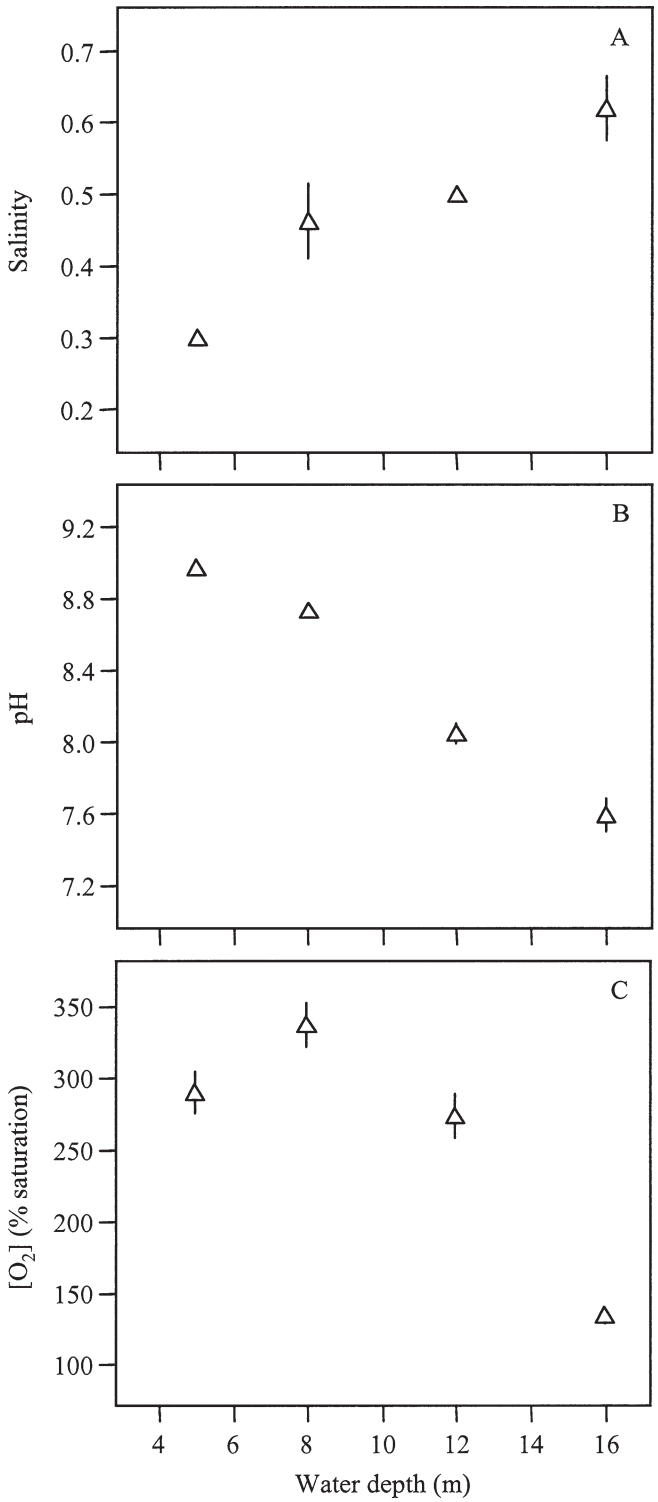

Fig. 3. (A) Bottom-water salinity, (B) pH, and (C) [O_2] measured along a transect from beneath the ice hole to 16-m depth. Symbols indicate the mean ($n = 5$), and vertical lines indicate standard deviations.

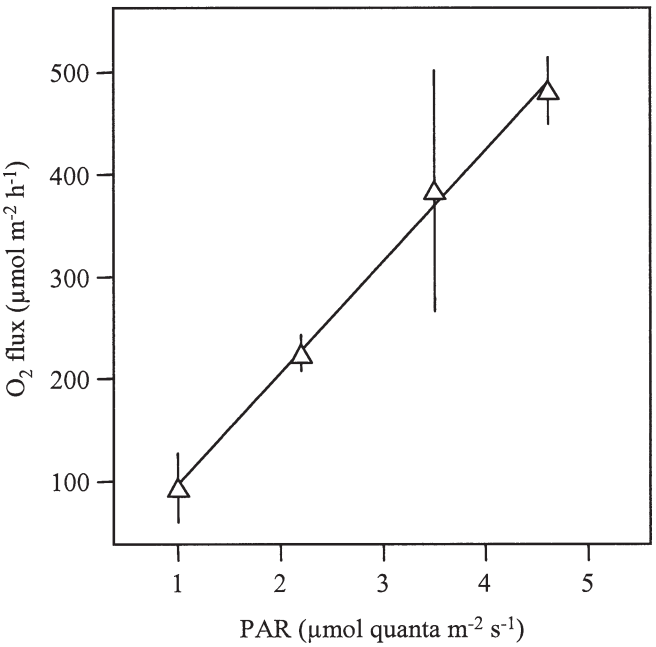

Fig. 4. Relationship between diffusive flux of O_2 across the mat–water interface and PAR. Linear fit, $R^2 = 0.9967$.

Depth-integrated net O_2 production in the upper 21 mm of a mat at 16.6-m water depth was 120 μmol m^{-2} h^{-1} under conditions of irradiance of PAR of 1 μmol quanta m^{-2} s^{-1}. The flux of O_2 across the DBL was similar, 118 μmol m^{-2} h^{-1}. There were four distinct zones of depth-integrated net O_2 production/consumption in the upper 21-mm-thick layer (Fig. 5B). Net O_2 production in the first 1.6-mm-thick layer was 117 μmol m^{-2} h^{-1}; the underlying 3.4-mm-thick layer produced 11 μmol O_2 m^{-2} h^{-1}. Note that, in contrast to the profile measured at 8.1-m water depth, the O_2 consumption profile shown in Fig. 5B describes a large fraction of the laminated, non-pigmented base of the mat. O_2 consumption in the non-pigmented zone of the mat was 4.1 μmol m^{-2} h^{-1} at depths between 5 mm and 6.6 mm and below 6.6 mm, was 3.6 μmol m^{-2} h^{-1}.

Pinnacle mats—Densely spaced valleys, holes, and ridges at scales ranging from millimeters to centimeters structured the surface of pinnacle mats at 12-m water depth (Fig. 1B). Our chlorophyll fluorescence images indicate high concentration of chlorophyll along edges of pinnacles and, in some cases, at the very tips (Fig. 6A). Vertical $[O_2]$ profiles measured from a position above the mat into the valleys revealed steep gradients within the mat boundary and two characteristic peaks (Fig. 6B,C). The bottom water above the mat was O_2 oversaturated; concentrations ranged between 1.3 mmol O_2 L^{-1} and 1.6 mmol O_2 L^{-1} (285–350% saturation). $[O_2]$ peaked in the water surrounding the pinnacle tips, decreased rapidly towards the surface of the mat, and then increased again within the mat matrix.

RLC and rETR—Mats from 8.1-m water depth comprised a pigmented gelatinous matrix (20–25-mm thick) of

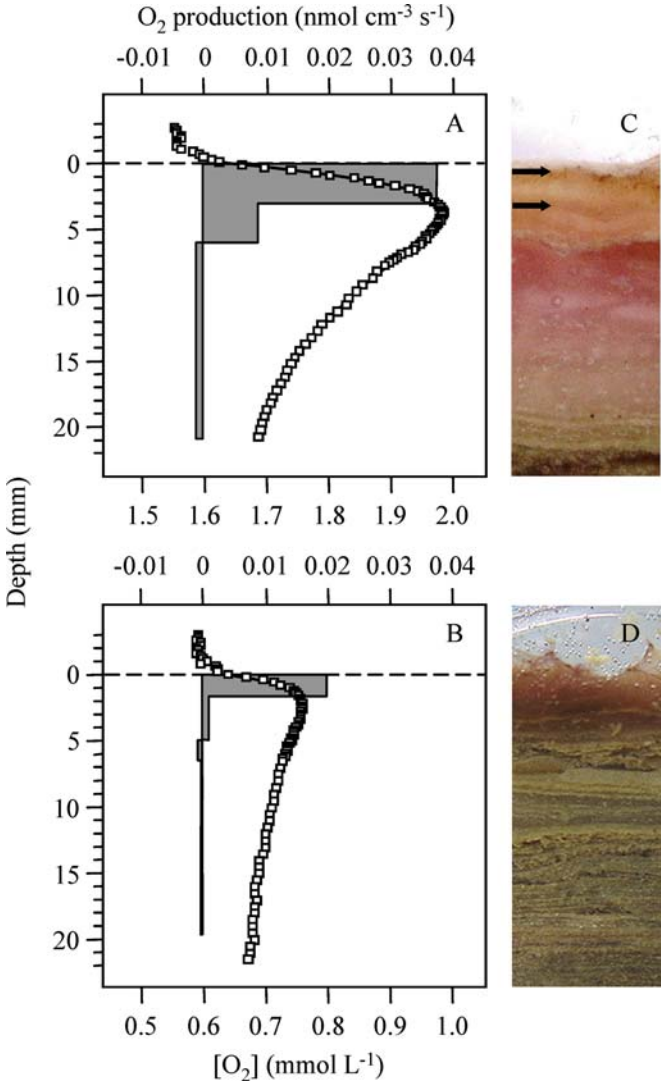

Fig. 5. (A, B) Two vertical in situ $[O_2]$ profiles (squares, lower scales) measured across mats at (A) 8.1-m and (B) 16.6-m water depth. At the time, irradiance was 4.6 μmol quanta m^{-2} s^{-1} and 1.0 μmol quanta m^{-2} s^{-1}. The fits indicate the calculated best-fitting concentration profile (lower scale) and the bars indicate the connected net O_2 production profile (upper scales). R^2 for the best-fitting concentration profiles in (A) and (B) were 0.9990 and 0.9943, respectively. The dashed lines indicate the surface of the mats. The equilibrium atmospheric solubility for O_2 was 0.457 mmol L^{-1}. (C, D) Digital photographs of cross sections of mats from (A) 8.1-m and (B) 16.4-m water depth. Horizontal arrows on panel (C) indicate the location of the two most recent growth layers.

alternating optically dense (<1 mm thick) and hyaline (2–3-mm thick) layers overlying a base (several centimeter thick) composed of 0.5–1-mm-thick alternating bands of organic material and sand (Fig. 7C). The pigmented matrix consisted of an uppermost brownish layer (5-mm thick) followed by a pink layer and contained numerous sand grains and calcite crystals. In contrast to mats from 8.1-m water depth, the upper pigmented gelatinous matrix of mats from 16.6-m water depth was only 3–5-mm thick and

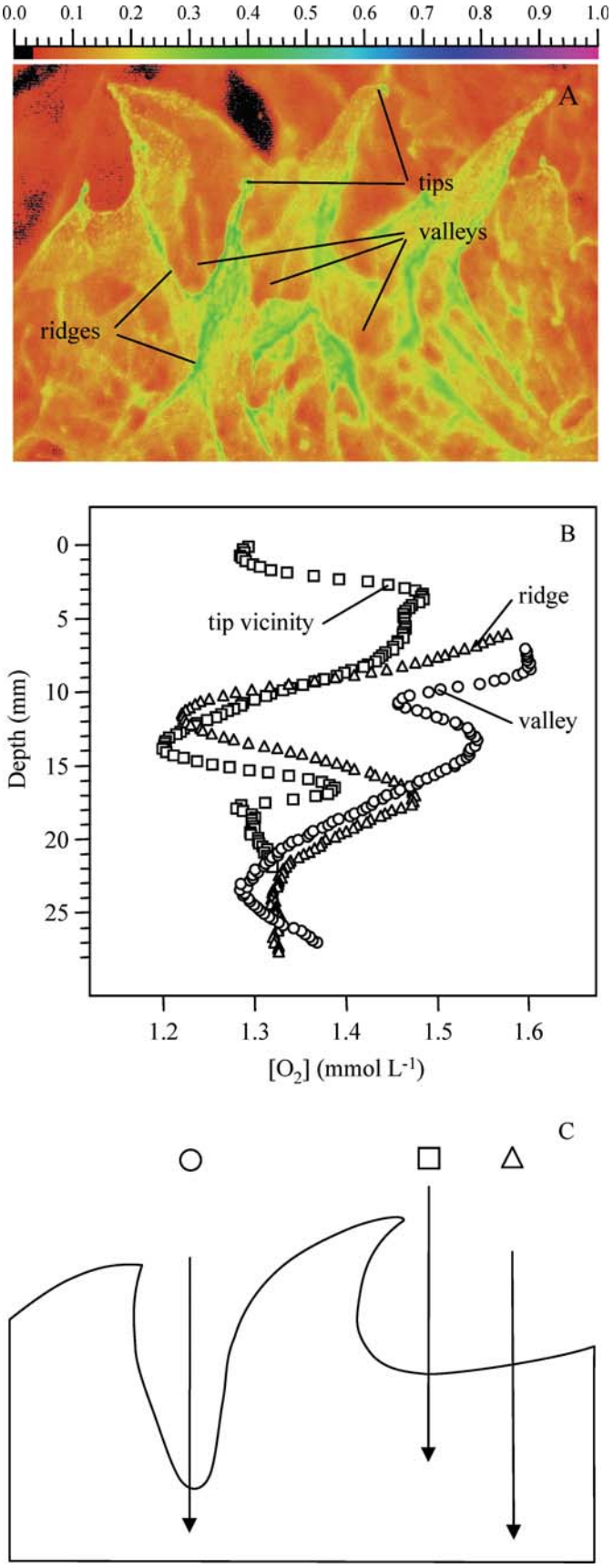

alternating optically dense and hyaline layers were ~1-mm thick.

The two vertical panels in Fig. 7 illustrate the contrasting thickness of the chlorophyll-containing layer and the lamination of these layers at two depths. They show the same field of view of cross sections of mats from 8.1 m and 16.6 m, imaged with the PAM (as F_0 and as ϕ_p) and with a digital camera. Inspection of the F_0 images (Fig. 7A,D) revealed three laminae of pigments in the upper layer of the mats from 16.6-m water depth, but at least six laminae in the pigmented layer of mats from 8.1-m water depth. Chlorophyll fluorescence was maximal in the upper laminae of the mat from 8.1-m water depth and, with increasing depth into the mat, the chlorophyll fluorescence was associated with the optically dense layers. Inspection of the false color images of ϕ_p in Fig. 7B,E revealed little structure to this parameter.

Our two profiling PAM measurements across the cross sections of the upper pigmented layer of mats from 12-m water depth yielded similar values of all photosynthetic parameters, and showed a similar decline in E_k and $rETR_{max}$ with increasing depth into the mat (Table 3).

Discussion

We have demonstrated, for the first time, in situ benthic photosynthesis in a permanently ice-covered lake of the McMurdo Dry Valleys. We showed that microbial mats in Lake Hoare to at least 16.6-m water depth are net producers of O_2 during the summer period. To estimate the rates of O_2 evolution from in situ, steady-state $[O_2]$ profiles we used two different approaches: we calculated the efflux of O_2 across the DBL from the $[O_2]$ gradient in the DBL, and we used $[O_2]$ profiles in the upper 21-mm-thick layer of the mat to model the net O_2 production rate profile (Fig. 5) and the area-specific depth-integrated net O_2 production. It should be noted that the net O_2 production rate profiles were calculated assuming ϕ and D_s to be depth invariant, which may not be the case given the laminated structure of the mats, and that microelectrodes can affect the DBL when introduced from above and, thereby, the derived solute exchange rates (Glud et al. 1994). Furthermore, the calculation of net O_2 production rates and area-specific depth-integrated net O_2 production only includes the metabolic activity within the upper 21 mm of the mats, whereas estimates of the O_2 flux from the concentration profiles in the DBL integrate the total benthic activity, including O_2 consumption in the deeper (>21 mm depth) laminated sediment. General agreement

←

Fig. 6. (A) Chlorophyll fluorescence image showing the concentration of pigments associated with the small pinnacles (1–2 cm high) in the center of the picture. The false-color image shows low concentrations as red and higher concentrations as yellow, then green. (B) Three $[O_2]$ profiles across the surface of a pinnacle mat taken from 12-m water depth. (C) Sketch showing an outline of a section of a pinnacle mat and the approximate path of the microelectrode during measurements of the profiles shown in (B). Note the sketch is not in scale.

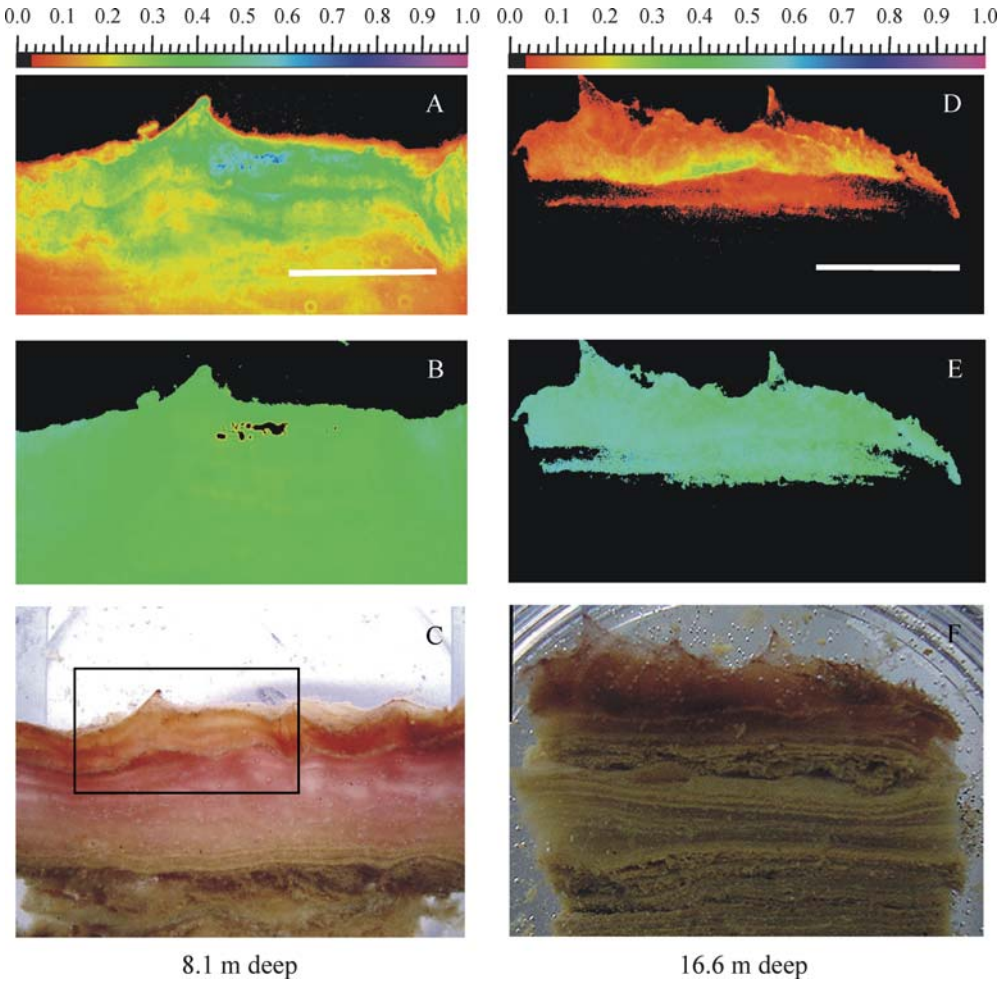

Fig. 7. Representative images of (A, D) the minimal fluorescence, F_0, and (B, E) maximal photochemical yield, $(F_m - F_0) \times F_m^{-1}$, and (C, F) digital photograph of cross sections of the photosynthetic active zones. (A, B, C) Mat from 8.1-m water depth; (D, E, F) mat from 16.6-m water depth. The color-gradient scale indicates the magnitude of the fluorescence signal. Bar, 10 mm.

between the two estimates, however, indicates that the respiration in the deeper unpigmented laminated zone of the mat must be negligible. The production profile in Fig. 5B, which covers the upper part of the laminated unpigmented zone of the mat, actually indicates a very low volume specific consumption (respiration) of 7.61×10^{-5} nmol O_2 cm^{-3} s^{-1} at depths below 6.6 mm. Assuming a 10-cm-thick column of unpigmented laminated sediment, the area specific consumption in this zone would be 27.69 μmol m^{-2} h^{-1} (= 0.089 μg cm^{-2} h^{-1}), which is more than three times lower than the rates estimated for mats in Lake Hoare by Hawes and Schwarz (2000) based on the laboratory gas-exchange measurements. Such low decomposition rates, in combination with the lack of grazing and bioturbation by metazoans, the lack of strong internal currents, the continuous influx of sediment through the ice cover, and the accumulation of carbonates, may promote the formation and preservation of modern stromatolites that will eventually become lithified, resulting in lacustrine carbonate sedimentary deposits. This process may contribute significantly to water-column O_2 supersaturation because it isolates fixed carbon from the lake's metabolism. Additional sources of O_2 may come from microbial mats that leave Lake Hoare after freezing into the ice cover (lift-off mats) and meltstreams carrying O_2 into this lake that is exsolved when water freezes onto the bottom of the ice cover (Wharton et al. 1986).

For mats from 7-m and 10-m water depth in Lake Hoare, Hawes et al. (2001) estimated rates of irradiance-saturated gross photosynthesis of 2.32 μg O_2 cm^{-2} h^{-1} and 2.06 μg O_2 cm^{-2} h^{-1} and maximum respiration rates of 0.58 μg O_2 cm^{-2} h^{-1} and 0.34 μg O_2 cm^{-2} h^{-1}, respectively. Hence irradiance-saturated net photosynthesis would be 1.74 μg O_2 cm^{-2} h^{-1} and 1.72 μg O_2 cm^{-2} h^{-1}, which translates to 543.8 μmol O_2 m^{-2} h^{-1} and 537.5 μmol O_2 m^{-2} h^{-1}. These rates are 22–23% higher than the O_2 flux calculated from our in-situ measurements at 8.1-m water depth. This suggests that benthic photosynthesis was light-limited, and this was supported by our profiling RLC measurements. Phototrophs throughout the pigmented layer of the mat were photosynthetically competent, with E_k values that indicated that, at all irradiances likely to be experienced under ice, photosynthesis at all depths in the mat was light-limited, therefore operating at or close to

Table 3. Photosynthetic parameters estimated from RLC measurements using cross sections of mats from 8-m, 12-m, and 16-m water depth. E_k (μmol m^{-2} s^{-1}); $rETR_{max}$, (μmol electrons m^{-2} s^{-1}); α, ([mol electrons m^{-2} s^{-1}] × [mol quanta m^{-2} s^{-1}]$^{-1}$); $(F_m - F_0) \times F_m^{-1}$, maximal photochemical yield.

Position	R^2	$rETR_{max}$	E_k	α	$(F_m - F_0) \times F_m^{-1}$
12 m A					
1	0.9962	14.23±0.36	28	0.507±0.012	0.569
2	0.9959	9.42±0.15	20	0.466±0.012	0.527
3	0.9920	8.00±0.18	20	0.389±0.014	0.485
4	0.9907	8.58±0.23	26	0.335±0.013	0.441
5	0.9924	7.48±0.17	23	0.322±0.011	0.427
6	0.9908	6.67±0.15	18	0.363±0.014	0.465
7	0.9821	5.60±0.16	15	0.381±0.020	0.503
12 m B					
1	0.9974	15.12±0.24	31	0.484±0.009	0.545
2	0.9968	12.18±0.19	25	0.470±0.011	0.530
3	0.9963	11.93±0.21	26	0.456±0.011	0.526
4	0.9953	11.54±0.34	34	0.343±0.009	0.438
5	0.9954	10.27±0.21	29	0.349±0.009	0.453
6	0.9932	8.90±0.19	23	0.384±0.012	0.502
7	0.9925	6.85±0.13	17	0.392±0.013	0.533

maximum quantum efficiency. Inferences on photoadaptive state from the RLC measurements are not definitive in this context. Given that the measurements were made on vertical sections of mat, with deeper mat layers exposed to non-ambient conditions, the estimates of E_k must be viewed with caution.

Our analysis of in situ [O_2] profiles measured across mats at 16.6-m water depth lead to a similar conclusion of light limitation of photosynthesis. The depth-integrated net O_2 production was lower than the irradiance-saturated rates of net photosynthesis calculated by Hawes et al. (2001) for mats at 13-m and 19-m depth in Lake Hoare (375 μmol O_2 m^{-2} h^{-1} and 116 μmol O_2 m^{-2} h^{-1}). We conclude that, in Lake Hoare, photosynthesis always occurs at or close to maximum efficiency, at all depths in the mat, and at all depths in the lake. That is, even minor changes in the intensity of the incident downwelling irradiance of PAR due to, for example, changes in the transparency of the ice cover or the optical properties of the water column (*see*, e.g., Howard-Williams et al. 1998) would significantly alter the rates of benthic carbon fixation.

The Imaging-PAM depictions of the minimal chlorophyll fluorescence yield, F_0, and peaks in the profiles of attenuation of scalar irradiance within the mat indicate layering of the photosynthetic community. F_0 is, however, only a proxy for chlorophyll *a* and is affected by the efficiency of the light harvesting systems in intercepting and transferring energy within the various chlorophyll-containing organisms in microbial mats (Schreiber 2004). Banding of F_0 may indicate layering of those organisms that respond most to the excitation wavelengths used (diatoms, for example) rather than of the entire photosynthetic assemblage. Further support for layering of all phototrophs, however, is provided by the observation of bands within the mat where attenuation of diffuse irradiance in wavebands sensitive to both algal and cyanobacterial pigments increases proportionally more than that of the waveband 740–750 nm, where algal and cyanobacterial pigments show little absorbance. We note that bacteriochlorophylls absorb in the 740–750-nm waveband, but authors' unpublished analyses of mat pigments using high-performance liquid chromatography have detected bacteriochlorophylls only below 23-m water depth. Absorption in the 740–750-nm waveband can therefore be attributed primarily to non-pigmented materials such as sediment and organic debris. In contrast, attenuation of scalar irradiance at wavelengths of 575–585 nm, 625–635 nm, and 670–680 nm will include contributions from chlorophyll, phycoerythrin, and phycocyanin of diatoms and cyanobacteria. We found maxima in the attenuation coefficient of these wavebands at the same depths of 0–0.5 mm and 4 mm, coincident with maxima in F_0 (Fig 7A) and with the position of dense portions of the photograph in Fig. 5C (arrows). Note that our optical sensor had a relatively low spatial resolution, so the attenuating layers were only distinguishable in the uppermost zone of the mat where the thickness of the most recent annual layers was large enough. Layers at greater depths were compacted, and the spatial resolution of the sensor was too low to detect small-scale changes in attenuation.

The alternation between 5 months of growth and 7 months of no growth perhaps explains the origin of the horizontal alternating layers of hyaline and dense material in mats of Lake Hoare (Hawes et al. 2001). Hyaline layers apparently form during summer growth, while as growth slows in late summer, sedimentary material, which enters this lake during late summer meltwater flow and through cracks in ice cover (Priscu et al. 1999), may settle on the mat surface. Optically dense layers form in winter when photosynthesis and growth stop, and the phototrophs and sediments accumulate at the surface. With the onset of daylight, renewed growth of surviving trichomes initiates a new hyaline layer. Trichomes that survive but do not grow vertically may remain as the horizontal layer in a way

analogous to that described by Doemel and Brock (1977) for warm-water laminated mats.

Hawes et al. (2001) estimated that the growth of mats in Lake Hoare at water depth between 7 m and 19 m results in an annual increase in mat thickness between 2.5 mm and 0.2 mm. Consequently, the uppermost zone of high net photosynthesis shown in Fig. 5A,B (bars) likely constituted the recent (2004) annual layer, whereas photosynthesis in the underlying zone would have been caused by the activity of the previous-year layers. Hence, photosynthesis, and potentially therefore growth, in mats from 8–16-m water depth may not be confined to the most recent annual layer. The images in Fig. 7B,E revealed no vertical structure to the parameter ϕ_p, which indicates that all of the fluorescing chlorophyll in the previous-year layers was connected to fully competent photosystems. As discussed above, slicing the mat vertically and exposing the cross section to air-saturated water will have altered conditions for photosynthesis, and while these images do indicate the potential for high efficiency in the deeper mat layers, they do not show this to occur in situ. Another experimental uncertainty is the fact that the operational depth/volume from which fluorescence signals are obtained rely on the optical density of the mat. During the saturation, pulse fluorescence from deeper layers can contribute to the signal, while measurements of *F*-values, especially at low actinic irradiances, sample from shallower layers. Thus, yield measurements represent averages over an unknown volume, which can lead to artifacts (*see* e.g., Grunwald and Kühl 2004).

Assuming a molar ratio of C : O = 1.2 : 1 and that the absorption efficiency is the same for pigment arrays at different water depths, we used the slope of our irradiance-versus-O_2-flux curve (Fig. 4) to estimate an area-specific maximum community quantum yield of 0.073 mol carbon (C) per mol photons incident to the mat surface (1 mol of carbon fixed for every 13.7 mol incident photons). This yield is similar to that calculated by Hawes and Schwarz (1999) for mats from 10-m water depth in Lake Hoare: 0.06 mol C mol^{-1} quanta. (Our calculation still underestimates the actual yield because we do not partition photon absorption between pigments and other matter.) Extrapolation of the irradiance-versus-O_2-flux curve in Fig. 4 revealed a low compensation irradiance of 0.1 μmol quanta m^{-2} s^{-1}, reflecting high shade acclimation. Again, this result supports the low compensation-irradiance estimates of <0.5 μmol quanta m^{-2} s^{-1} for mats in Lake Hoare from >13-m water depth published by Hawes and Schwarz (1999, 2000).

Our measurements within the boundary of pinnacle mats revealed a complex small-scale chemical landscape. These measurements and the images in Figs. 1B and 6A indicate that a one-dimensional approach to quantification of solute exchange and reaction rates may not be a good approximation for this type of mat (*see* also Jørgensen and Des Marais 1990, and Glud et al. 1999). We selected areas devoid of pinnacles for measuring in situ O_2 profiles (e.g., *see Fig. 1A*) and this methodological necessity may have resulted in an underestimation of areal production in heavily pinnacled areas. The origin and function of the pinnacles in such pinnacle mats is unknown, but may be caused by positive phototaxis similar to that reported on pinnacle mats in hot springs (Walter 1977). However, the formation of pinnacles does not automatically imply photomovement. In many low-flow or stagnant environments, mats with pinnacle structures develop. This can in some cases be due to formation of internal gas bubbles that are overgrown and in other cases be a strategy to overcome or minimize diffusion limitation of solute exchange. Also, largely non-motile mats in other environments can develop conspicuous pinnacles over time (Kühl et al. 2003).

In conclusion, we have shown that microbial mats in Lake Hoare to at least 16.6-m water depth are net producers of O_2 during the summer period. We confirmed key parameters of benthic photosynthesis previously derived only from laboratory gas-exchange measurements, and we present evidence that photosynthesis in the mats occurs, at all depths in the mat and at all lake depths, at or close to maximum photosynthetic efficiency. This simplifies modeling simulations of benthic photosynthesis in the lake, and implies that annual production will be related to ice and water transparency, which vary from year to year (Howard-Williams et al. 1998). Our high-resolution laboratory measurements at the surface of pinnacle mats revealed a complex small-scale chemical structure of the mat–water interface. We propose manipulative in-situ experiments to understand the mechanisms that lead to the formation of pinnacles and to reveal the implications of such structures for light-limited growth in the diffusion-dominated permanently ice-covered lakes.

References

Berg, P., N. Risgaard-Petersen, and S. Rysgaard. 1998. Interpretation of measured concentration profiles in sediment pore water. Limnol. Oceanogr. **43:** 1500–1510.

Broecker, W. S., and T.-H. Peng. 1974. Gas exchange rates between air and sea. Tellus **26:** 185–190.

Cathey, D. D., B. C. Parker, G. M. Simmons, W. H. Yongue, and M. R. Van Brunt. 1981. The microfauna of algal mats and artificial substrates in Southern Victoria Land lakes of Antarctica. Hydrobiologia **85:** 3–15.

Craig, H., R. A. Wharton, Jr., and C. P. McKay. 1992. Oxygen supersaturation in ice-covered Antarctic lakes: Biological versus physical contributions. Science **255:** 318–321.

Doemel, W. N., and T. D. Brock. 1977. Structure, growth, and decomposition of laminated algal-bacterial mats in alkaline hot springs. Appl. Environ. Microbiol. **34:** 433–452.

Doran, P. T., C. P. McKay, G. D. Clow, G. L. Dana, A. G. Fountain, T. Nylen, and W. B. Lyons. 2002*a*. Valley floor climate observations from the McMurdo dry valleys, Antarctica, 1986–2000. J. Geophys. Res. **107:** 4772.

———, and others. 2002*b*. Recent climate cooling and ecosystem response in the McMurdo Dry Valleys, Antarctica. Nature **415:** 517–520.

Dore, J. E., and J. C. Priscu. 2001. Phytoplankton phosphorus deficiency and alkaline phophatase activity in the McMurdo Dry Valley lakes, Antarctica. Limnol. Oceanogr. **46:** 1331–1346.

Epping, E. H. G., A. Khalili, and R. Thar. 1999. Photosynthesis and the dynamics of oxygen consumption in a microbial mat as calculated from transient oxygen microprofiles. Limnol. Oceanogr. **44:** 1936–1948.

GLUD, N. G., J. K. GUNDERSEN, N. P. REVSBECH, AND B. B. JØRGENSEN. 1994. Effects on the benthic diffusive boundary layer imposed by microelectrodes. Limnol. Oceanogr. **39:** 462–467.

———, M. KÜHL, O. KOHLS, AND N. B. RAMSING. 1999. Heterogeneity of oxygen production and consumption in a photosynthetic microbial mat as studied by planar optodes. J. Phycol. **35:** 270–279.

GRUNWALD, B., AND M. KÜHL. 2004. A system for imaging variable chlorophyll fluorescence of aquatic phototrophs. Ophelia **58:** 79–89.

HAWES, I., D. MOORHEAD, D. SUTHERLAND, J. SCHMELING, AND A-M. SCHWARZ. 2001. Benthic primary production in two perennially ice-covered Antarctic lakes: patterns of biomass accumulation with a model of community metabolism. Antarctic Science **13:** 18–27.

———, AND A.-M. SCHWARZ. 1999. Photosynthesis in an extreme shade environment: benthic microbial mats from Lake Hoare, a permanently ice-covered Antarctic lake. J. Phycol. **35:** 448–459.

———, AND ———. 2000. Absorption and utilization of irradiance by cyanobacterial mats in two ice-covered Antarctic lakes with contrasting light climates. J. Phycol. **37:** 5–15.

———, D. SUTHERLAND, AND D. HANELT. 2003. The use of pulse amplitude modulated fluorometry to determine fine-scale temporal and spatial variation of in situ photosynthetic activity within an *Isoetes*-dominated canopy. Aquat. Bot. **77:** 1–15.

HEYWOOD, R. B. 1984. Antarctic inland waters, p. 279–344. *In* R. M. Laws [ed.], Antarctic ecology, v. 1. Academic.

HOFSTRAAT, J. W., J. C. H. PEETERS, J. F. H. SNEL, AND C. GEEL. 1994. Simple determination of photosynthetic efficiency and photoinhibition of *Dunaliella tertiolecta* by saturating pulse fluorescence measurements. Mar. Ecol. Prog. Ser. **103:** 187–196.

HOWARD-WILLIAMS, C., A.-M. SCHWARZ, AND I. HAWES. 1998. Optical properties of the McMurdo Dry Valley Lakes, Antarctica. Antarctic Research Series **72:** 189–203.

JASSBY, A. D., AND T. PLATT. 1976. Mathematical formulation of the relationship between photosynthesis and light for phytoplankton. Limnol. Oceanogr. **21:** 540–547.

JØRGENSEN, B. B., AND D. J. DES MARAIS. 1990. The diffusive boundary layer of sediments: Oxygen microgradients over a microbial mat. Limnol. Oceanogr. **35:** 1343–55.

KIRK, J. T. O. 1983. Light and photosynthesis in aquatic ecosystems. Cambridge.

KÜHL, M., T. FENCHEL, AND J. KAZMIERCZAK. 2003. Growth, structure and calcification potential of an artificial cyanobacterial mat, p. 77–102. *In* W. E. Krumbein, D. Paterson, and G. Zavarzin [eds.], Fossil and recent biofilms, a natural history of life on Earth. Kluwer.

———, R. N. GLUD, J. BORUM, R. ROBERTS, AND S. RYSGAARD. 2001. Photosynthetic performance of surface-associated algae below sea ice measured with a pulse-amplitude-modulated (PAM) fluorometer and O_2 microsensors. Mar. Ecol. Prog. Ser. **223:** 1–14.

LASSEN, C., PLOUGH., AND B. B. JØRGENSEN. 1992. A fiber-optic scalar irradiance microsensor: Application for spectral light measurements in sediments. FEMS Microbial Ecol. **86:** 247–254.

LI, Y.-H., AND S. GREGORY. 1974. Diffusion of ions in sea water and in deep-sea sediments. Geochim. Cosmochim. Acta **38:** 703–714.

LIZOTTE, M. P., AND J. C. PRISCU. 1992. Photosynthesis-irradiance relationship from the physically stable water column of a perennially ice-covered lake (Lake Bonney, Antarctica). J. Phycol. **28:** 179–185.

MOORHEAD, D., J. SCHMELING, AND I. HAWES. 2005. Modeling the contribution of benthic microbial mats to net primary production in Lake Hoare, McMurdo Dry Valleys. Antarctic Science **17:** 33–45.

PARKER, B. C., G. M. SIMMONS, JR., F. G. LOVE, R. A. WHARTON, JR., AND K. G. SEABURG. 1981. Modern stromatolites in Antarctic dry valley lakes. BioScience **31:** 656–661.

PRISCU, J. C., L. R. PRISCU, W. F. VINCENT, AND C. HOWARD-WILLIAMS. 1987. Photosynthate distribution by microplankton in permanently ice-covered Antarctic desert lakes. Limnol. Oceanogr. **32:** 260–270.

———, AND OTHERS. 1999. Carbon transformations in a perennially ice-covered Antarctic lake. BioScience **49:** 997–1007.

RALPH, P. J., AND R. GADEMANN. 2005. Rapid light curves: A powerful tool to assess photosynthetic activity. Aquat. Bot. **82:** 222–237.

———, U. SCHREIBER, R. GADEMANN, M. KÜHL, AND A. D. W. LARKUM. 2005. Coral photobiology studied with a new imaging pulse amplitude modulated fluorometer. J. Phycol. **41:** 335–342.

REVSBECH, N. P. 1989. An oxygen microelectrode with a guard cathode. Limnol. Oceanogr. **34:** 474–478.

SCHREIBER, U. 2004. Pulse-amplitude (PAM) fluorometry and saturation pulse method, p. 279–319. *In* G. Papageorgiou and Govindjee [eds.], Chlorophyll fluorescence: A signature of photosynthesis. Advances in photosynthesis and respiration series, Kluwer.

———, M. KÜHL, I. KLIMANT, AND H. REISING. 1996. Measurement of chlorophyll fluorescence within leaves using a modified PAM fluorometer with a fiber-optic microprobe. Photosynth. Res. **47:** 103–109.

VINCENT, W. F. 1981. Production strategies in Antarctic inland waters: Phytoplankton eco-physiology in a permanently ice-covered lake. Ecology **62:** 1215–1224.

WALTER, M. R. 1977. Interpreting stromatolites. American Scientist **65:** 563–571.

WHARTON, JR., R. A., W. B. LYONS, AND D. J. DES MARAIS. 1993. Stable isotopic biogeochemistry of carbon and nitrogen in a perennially ice-covered Antarctic lake. Chemical Geology (Isotope Geoscience Section) **107:** 159–172.

———, C. P. MCKAY, G. M. SIMMONS, JR., AND B. C. PARKER. 1986. Oxygen budget of a perennially ice-covered Antarctic lake. Limnol. Oceanogr. **31:** 437–443.

———, M. A. MEYER, C. P. MCKAY, R. L. MANCINELLI, AND G. M. SIMMONS, JR. 1994. Sediment oxygen profiles in a superoxygenated Antarctic lake. Limnol. Oceanogr. **39:** 839–853.

———, B. C. PARKER, AND G. M. SIMMONS, JR. 1983. Distribution, species composition and morphology of algal mats in Antarctic dry valley lakes. Phycologia **22:** 355–365.

Received: 13 October 2005
Accepted: 23 February 2006
Amended: 7 March 2006

Limnol. Oceanogr., 50(1), 2005, 128–133

Wave-induced H_2S flux sustains a chemoautotrophic symbiosis

Kay Vopel[1]
National Institute of Water & Atmospheric Research, Hamilton, New Zealand

David Thistle
Department of Oceanography, Florida State University, Tallahassee, Florida 32306-4320

Jörg Ott and Monika Bright
Institute of Ecology and Conservation Biology, University of Vienna, 1090 Vienna, Austria

Hans Røy
Max Planck Institute for Marine Microbiology, 28359 Bremen, Germany

Abstract

Symbioses involving sulfur-oxidizing bacteria and invertebrate hosts require a source of reduced sulfur, a source of O_2, and transport mechanisms that ensure them a supply of both. We investigated these mechanisms using the symbiosis between the sessile ciliate *Zoothamnium niveum* (Hemprich and Ehrenberg 1831) and bacteria living on its surface. The stalked colonies of *Z. niveum* grow on peat walls around the openings of centimeter-scale conduits created when mangrove rootlets decompose. Using in situ, time-series measurements with fast-responding amperometric microelectrodes, we found that the conduits were charged with H_2S by diffusion from the decaying rootlets during periods of low boundary-layer flow speed. During these times, the feeding current of the zooids transported oxygenated seawater from outside the peat wall toward the ectobiotic bacteria. During periods of high flow speed, H_2S-rich seawater from the conduits was drawn along the colonies and over the bacteria. We conclude that this symbiosis exploits a combination of two transport mechanisms: (1) venting of H_2S-rich seawater due to pulsating boundary-layer current over ciliate groups and (2) the continuous and rapid feeding current generated by the host's cilia. This discovery raises the possibility that other systems in which pockets of decay are exposed to pulsating flow could support similar symbioses.

Symbioses involving sulfur-oxidizing bacteria and various invertebrates or protists are found in many habitats, ranging from the ''hot vents'' along the axes of midoceanic ridges to the ''cold seeps'' of deep-sea and continental slope sediments (Paull et al. 1984; Suess et al. 1985) and shallow-water habitats, such as sheltered sediments in inter- and subtidal zones (Ott 1995), organic-rich mud (Reid 1980), and mangrove peat (Ott et al. 1998). These symbiotic associations show great diversity. For example, Vestimentifera (Jones 1984), Pogonophora (Southward 1982), and the nematode *Astomonema* (Ott et al. 1982; Giere et al. 1995) have intracellular symbionts. In gastropods and the bivalves, the symbiotic bacteria are associated with gill tissue, either intracellularly in special bacteriocytes or enclosed in intercellular spaces (Windoffer and Giere 1997). In *Rimicaris* (Polz and Cavanaugh 1995), the Stilbonematinae (Ott and Novak 1989), and ciliates (Fenchel and Finlay 1989; Bauer-Nebelsick et al. 1996*a*,*b*), the bacteria are ectosymbionts; they cover parts of the external surface of the host. Such associations, in which the morphological modifications are often minor and the physiological dependences are presumably less strict, can serve as model systems to study the circumstances that set the stage for the development of the early evolutionary stages of endosymbiosis (Smith 1979).

Symbioses involving sulfur-oxidizing bacteria require a source of reduced sulfur, a source of O_2, and transport mechanisms that ensure a supply of both. Because such symbioses often exploit a spatially and temporally complex chemocline, where oxic and sulfidic conditions may change over a few millimeters and within seconds, mechanisms that let the sulfur-oxidizing bacteria overcome the diffusion limitation of nutrient supply are difficult to study and are therefore largely unknown. In this study, we used a sessile symbiosis from a shallow-water habitat, the *Zoothamnium niveum* (Hemprich and Ehrenberg 1831) ectosymbiosis, as an example to investigate these mechanisms.

The *Z. niveum* symbiosis was discovered in coves and channels of red mangrove (*Rhizophora mangle* Linnaeus) islands of the barrier reef off Dangriga, Belize (Ott et al.

[1] Corresponding author (k.vopel@niwa.co.nz).

Acknowledgments

G. Arlt assisted with previous laboratory studies and underwater measurements, G. Cocco helped with analyses of time series measurements, and A. Vopel contributed to the model. The comments of P. Jumars, L. Mullineaux, A. B. Thistle, and one anonymous reviewer improved the manuscript. D. Oliff built the underwater housing for the data logger. M. Carpenter and D. Miller provided technical service at the field station of the Caribbean Coral Reef Ecosystems program of the Smithsonian National Museum of Natural History (Washington, DC).

This study was supported by the Austrian Science Foundation, the CCRE program of the Smithsonian National Museum of Natural History, and Unisense A/S (Aarhus, Denmark).

Contribution 657 of the CCRE program.

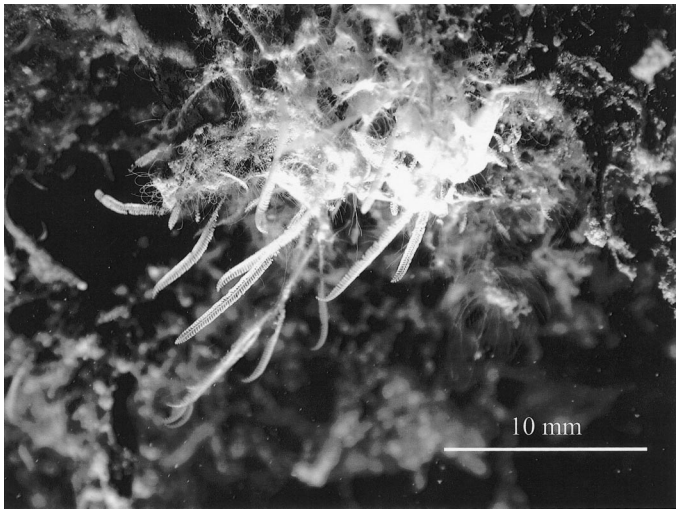

Fig. 1. A H_2S microvent at the surface of a vertically overhanging wall of red mangrove (*R. mangle* Linnaeus) peat at the mangrove island Twin Cays, Tobacco Reef section, Belize (16°48′N, 88°05′W). The tissue of a mangrove rootlet has rotted and partially fallen out, creating a conduit whose opening is surrounded by mats of unicellular and filamentous sulfur bacteria and the feather-shaped colonies of the peritrich ciliate species *Z. niveum*. The surrounding, intact surface of the peat is overgrown with diatoms and cyanobacteria.

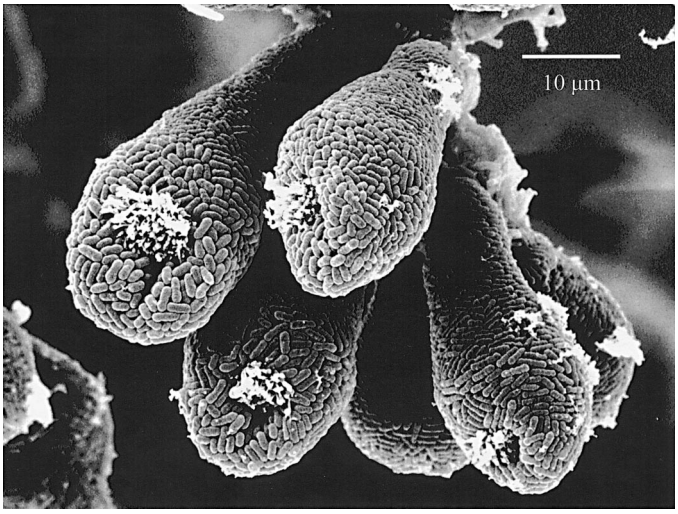

Fig. 2. *Z. niveum.* Scanning electron microscope picture of six contracted microzooids attached to a branch of a ciliate colony. The microzooids are overgrown by coccoid sulfur bacteria.

1998). The stalked colonies of *Z. niveum* grow on vertical walls of peat banks around the openings of centimeter-scale conduits (Fig. 1). The conduits form when mangrove rootlets die and decay, leaving only tubes of bark in the peat. The large (up to 15 mm) conspicuous colonies of *Z. niveum* occur in groups (~10 groups m^{-2}) of up to 100 colonies. The average life span of a group is ~3 weeks (Ott et al. 1998). The feather-shaped colonies are composed of polymorphic zooids (filter-feeding microzooids, dividing terminal zooids, and motile macrozooids) attached to a branched stalk. A single layer of coccoid and rod-shaped, sulfur-oxidizing bacteria covers all but the most basal parts of the colonies (Bauer-Nebelsick et al. 1996*a,b;* Fig. 2). Their white appearance stems from intracellular sulfur globules associated with the oxidation of sulfur compounds (Bauer-Nebelsick et al. 1996*b*).

Because of their white appearance, the colonies stand out from the surrounding brownish peat, which may also be covered by thin films of diatoms and cyanobacteria (Fig. 1). Ciliary movement of their zooids transports seawater, which is filtered for suspended particles (clearance rate ≈ 0.45 mm^3 s^{-1}). The joint action of all zooids of a colony results in unidirectional flow through the colony, perpendicular to the longitudinal axis of the stalk, from the convex to the concave side of the feather-like colony (Vopel et al. 2002). The inflowing current comes from a broad area; the exiting jet leaves the colony as a narrow band along its center line at 0.3–0.6 mm s^{-1} (H.R. and K.V. unpubl. data). Filter feeding of the zooids is frequently interrupted (1.7 min^{-1}) by rapid stalk contractions, during each of which the mass of zooids bunches together and whips downward at 520 mm s^{-1} (Reynolds number [Re] ≈ 10^2). After a contraction, the colony extends slowly (Re ≈ 10^{-1}). High shear stress during stalk contraction, cell shrinkage, and bunching of the zooids presumably detach ectobiotic bacteria that, once suspended, can be transported with the feeding current toward the cytostome (Vopel et al. 2002).

Our previous laboratory studies failed to discover how reduced sulfur released by the decaying rootlets is transported to the ectosymbiotic bacteria of *Z. niveum*. In the present study, we used fast-responding, amperometric microelectrodes in situ to investigate the mechanisms that generate the physicochemical microenvironment for rapid symbiotic growth.

Study site and methods

Microelectrode measurements of $[O_2]$ and $[H_2S]$ were carried out by SCUBA divers at overhanging vertical walls of red mangrove peat at the north entrance (Batfish Point) of the main channel of the mangrove island Twin Cays, Belize, in April 2002. Twin Cays is situated inside the Tobacco Reef section of the Belize barrier reef (16°48′N, 88°05′W). Detailed information about the site and a description of the area are available in Rützler and Macintyre (1982) and Ott et al. (1998). The average temperature of the seawater recorded from February 2001 through January 2002 was 28.1 ± 1.7°C (maximum = 32.1°C, minimum = 22.3°C). The water depth was <2 m, the average salinity was 35.4 ± 1.4 (n = 25), and the pH was 8.2 ± 0.1 (n = 18). The maximum flow speed measured by tracking the movement of particles in the water 5 cm away from the peat wall over a horizontal distance of 10 cm was 2.4 cm s^{-1}. Flow along the peat wall oscillated as a result of infragravity waves in the sea surrounding the mangrove islands. That is, seawater alternately moved into and out of coves or channels at a period of 50–200 s. These oscillations were superimposed on higher-frequency oscillations resulting from a variety of mechanisms related to specific hydrodynamic conditions and geometry of the cove or channel.

A H_2S microelectrode (Jeroschewski et al. 1996) and a Clark-type O_2 microelectrode with internal reference and guard cathode (Revsbech 1989) were mounted on a manually operated micromanipulator (Märzhäuser Wetzlar) such that their movement (250- or 500-μm increments) was normal to the vertical peat surface. The amperometric microsensor for dissolved H_2S is based on the same principle as the Clarke-type O_2 microsensor. The sensor is equipped with a glass-coated platinum working electrode and a platinum guard electrode. Both the working electrode and the guard electrode were polarized at +85 mV with respect to a counter electrode. The sensor was sealed with a thin silicone membrane and filled with a buffered electrolyte solution that contained ferricyanide ($K_3[Fe(CN)_6]$) as redox mediator. Driven by the external partial pressure, H_2S from the environment penetrates the silicone membrane and is oxidized by ferricyanide, which results in the formation of elemental sulfur and ferrocyanide ($K_4[Fe(CN)_6]$). The latter is electrochemically reoxidized at the platinum working electrode, creating an electrical current that is directly proportional to the $[H_2S]$ at the sensor tip. Note that this sensor detects the partial pressure of H_2S gas, which is only one component of the total equilibrium system. Both microelectrodes had outside tip diameters of 40–60 μm; the 90% response time was <1 s, the stirring sensitivity was $<2\%$, and the detection limit was 0.3×10^{-6} mol L^{-1}. The micromanipulator was attached to an aluminum post that had been driven into the mangrove peat. Sensor signals, measured and digitized by an underwater picoammeter (PA 3000U; Unisense), were logged at a frequency of 3.3 Hz (data logger OM-3000 and measurement analysis software OM-3000 MAS version 4.01; Omega Engineering).

At four randomly chosen locations, we measured one $[O_2]$ and one $[H_2S]$ profile across the intact surface of the peat near the opening of a rootlet conduit and repeated the measurements through the interface between the seawater and the opening of that conduit. We made four simultaneous time-series measurements of $[O_2]$ and $[H_2S]$ at one conduit opening on each of two consecutive days in April 2002. For these measurements, the two microelectrodes were positioned at an angle of 80° to the surface of the peat wall, so that their tips were both at the same distance from the opening of the rootlet conduit. The distance between the electrode tips was <1 mm. We measured at 1 mm inside the conduit, at the opening of the conduit, and 1 and 2 mm outside the opening. The measurements at each position required 10 min. During the time series on April 7, we observed that changes in the signals of the two microelectrodes correlated with changes in the displacement of the colonies from the vertical by the flow. During the time series measurements the following day, we estimated relative flow speed as follows. Using the method of La Fond (1967), we imagined a colony as hanging at the center of a clock face. The colony pointed to 6 o'clock when the water was still. As flow speed increased, the colony was deflected toward 3 or 9 o'clock. At regular intervals ($\sim$4 times min^{-1}), the diver wrote on a slate the clock position of a colony and the record number from the data logger. We used the recording number to match the $[O_2]$ and $[H_2S]$ values to estimated flow speed. Because our visual observations of deflection angles may misrepresent both the upper and lower flow speeds because of the inertia of the colony (low speed) and asymptotic relationship between flow and deflection (high speed), we used the data qualitatively.

The O_2 microelectrode was calibrated in fully oxygenated seawater and in seawater that had been deoxygenated with sodium sulfite. Microelectrodes were calibrated before each time series measurement at in situ temperature. The H_2S microelectrode was calibrated in a flow-through system that consisted of a peristaltic pump (Ismatec), a coulometric sulfide generator (AMT), and a flow-through chamber. The coulometric sulfide generator was equipped with a mixing cell for preparations of standard solutions in the micromolar range. H_2S was generated by cathodic reduction at an electrode made of HgS, S, and C in an oxygen-free, acid solution (0.01 mol L^{-1} H_2SO_4). This solution was pumped continuously through the coulometric cell and the flow-through chamber that enclosed the tip of the H_2S microelectrode. The $[H_2S]$ in the carrier solution was precisely adjustable through the flow rate (0.25–5 ml min^{-1}) and/or the current at the coulometric cell (0–4 mA). This technique allowed fast and accurate calibrations in the field and limited the loss of H_2S due to wall adsorption or exchange between the liquid and gas phases.

Spectral analyses of the time series measurements were done with the data analysis software system STATISTICA (StatSoft). The time series were transformed by simple exponential smoothing (no trend, no season, $\alpha = 0.1$), and the periodogram values were smoothed using a weighted moving average (Tukey window). Underwater photographs of groups of colonies of *Z. niveum* were made with a Nikon Coolpix 4500 digital camera. For scanning electron microscopy, specimens were fixed in 2.0% osmium tetroxide in natural seawater for 15 min at $\sim$30°C, then dehydrated in a graded series of ethanol-distilled water solutions, critical-point dried in CO_2 in a Polaron E3000 Series II critical-point drying apparatus, sputter-coated with gold/palladium with a Balzer SCD 030 Sputter-Coater, and viewed with a Cambridge Stereoscan 250 Mk2.

Results and discussion

Our in situ measurements showed that, under incident sunlight, the peat surface surrounding the openings of the conduits was supersaturated with O_2 (up to 724×10^{-6} mol L^{-1}) because of photosynthesis by mat-forming diatoms and cyanobacteria (Fig. 3A). Dissolved O_2 diffused through an $\sim$0.75-mm-thick diffusive boundary into the surrounding seawater. No H_2S was detected in the peat to a depth of 4 mm (Fig. 3A). In contrast, the seawater in the rootlet conduits was deoxygenated and contained up to 739×10^{-6} mol H_2S L^{-1} (Fig. 3B). The conduits were charged with H_2S by diffusion from the decomposing tissue and bark of the rootlets, where $[H_2S]$ was $>10^{-3}$ mol L^{-1}. At the peat-seawater boundary at the openings of the conduits, a maximum $[H_2S]$ of 639×10^{-6} mol L^{-1} was detected. $[H_2S]$ and $[O_2]$ outside the conduits and at the opening of the conduits varied rapidly. Simultaneous time series measurements of $[O_2]$ and $[H_2S]$ 1 mm outside of the conduit opening (Fig. 4A) and at

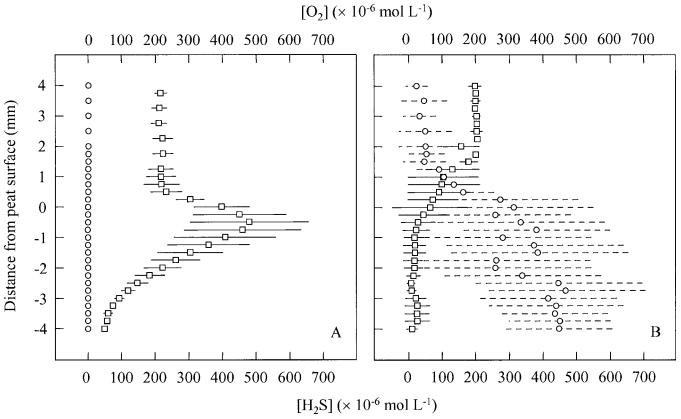

Fig. 3. Average $[O_2]$ (rectangles) and $[H_2S]$ (circles) profiles measured in situ normal to (A) the intact surface of the mangrove peat or (B) the opening of a rootlet conduit. The peat-water interface is located at 0 mm. Symbols indicate the mean ($n = 4$), and horizontal lines indicate standard deviations.

the conduit opening (Fig. 4B) showed alternating periods when $[H_2S]$ was high and $[O_2]$ was low and when $[H_2S]$ was low and $[O_2]$ was high. Measurements 1 mm inside the conduits revealed high $[H_2S]$ and low $[O_2]$; measurements 2 mm outside revealed high $[O_2]$ and low $[H_2S]$. Spectral analyses of the relatively short time series of $[H_2S]$ and $[O_2]$ revealed

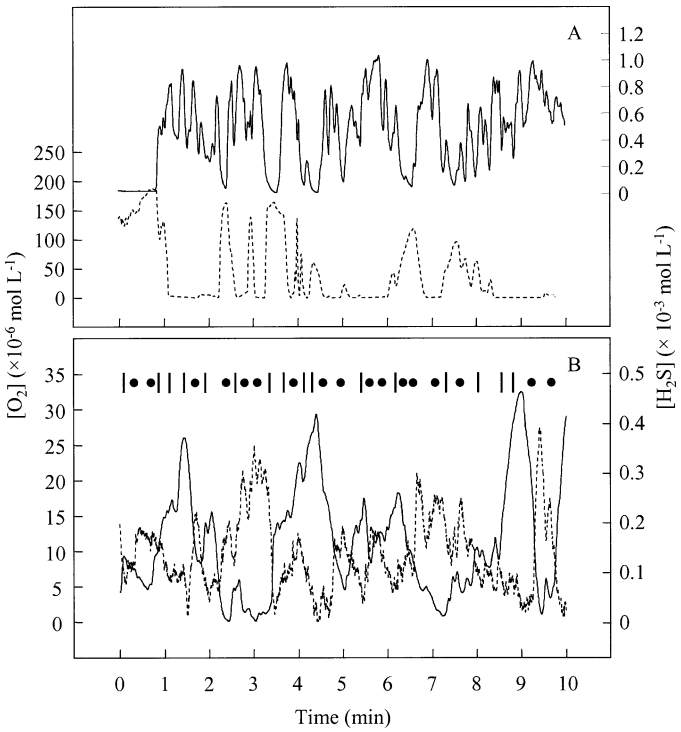

Fig. 4. Simultaneous time series of $[O_2]$ and $[H_2S]$ measured at the mouth of two mangrove-rootlet conduits on 2 consecutive d in April 2002. The two microelectrode tips were positioned at an angle of 80° to the surface of the peat wall at (A) 1 mm distance from the opening of the conduit and (B) the conduit opening. Dashed lines represent $[O_2]$. Filled circles indicate periods of relatively low flow speed, and vertical lines indicate periods of high flow speed.

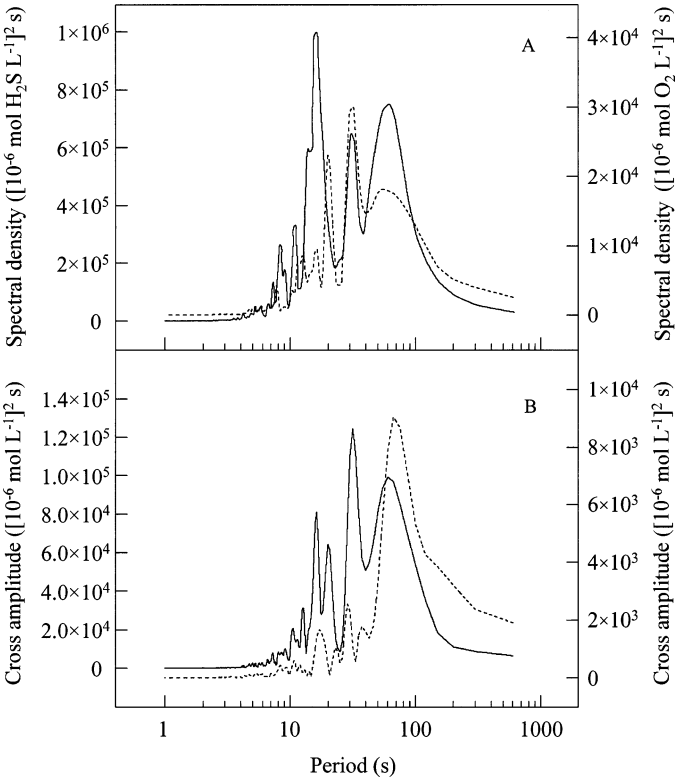

Fig. 5. (A) Spectral analyses of time series of $[O_2]$ (dashed line) and $[H_2S]$ presented in Fig. 4A. (B) Cross-spectrum of the two series shown in Fig. 4A (solid line, left *y*-axis) and 4B (dashed line, right *y*-axis).

peaks at periods of 10–100 s (*see Fig. 5 for examples*). The period with the greatest spectral density of the time series of $[H_2S]$ shown in Fig. 4A was 16 s (Fig. 5A). Smaller peaks occurred at periods of 31.7 and 61.4 s. The analysis of the simultaneously measured time series of $[O_2]$ (Fig. 4A) revealed a high spectral density at a period of 31.6 s (Fig. 5A). Cross-spectrum analysis confirmed the covariance between the respective frequency components in the two series (Fig. 5B). The measurement shown in Fig. 4B revealed temporal variation in seawater $[O_2]$ and $[H_2S]$ at periods of 18, 55, and 67 s that is superimposed over variation of shorter period. The cross-amplitude of these time series peaked at a period of 67 s (Fig. 5B, dashed line).

Our visual underwater observations revealed that the signals of the H_2S electrode were highest when colonies were horizontal (i.e., during periods of maximal flow speed) and lowest when colonies were hanging vertically (i.e., during periods of minimal flow speed). Matching the recorded $[O_2]$ and $[H_2S]$ values and the displacement of the ciliate colonies from the vertical confirmed this observation: $[H_2S]$ 1–2 mm outside the conduit opening was high during periods of high flow speed and low during periods of low flow speed. In contrast, measurements 1 mm inside the conduit revealed that $[H_2S]$ decreased and $[O_2]$ increased during periods of high flow speed. We conclude that fluctuations in $[H_2S]$ and $[O_2]$ at the openings of the conduits are caused by pulsed exchange of the deoxygenated, H_2S-containing seawater in

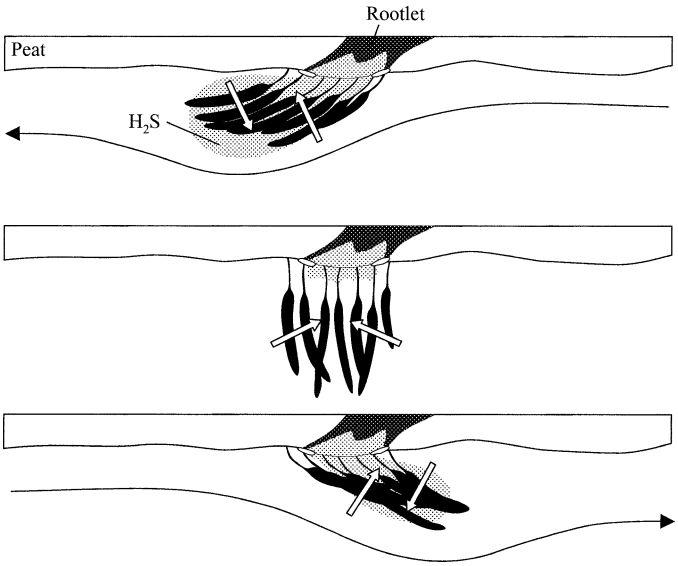

Fig. 6. Schematic drawing of cross section of peat matrix, a rootlet that had partially fallen out, and the attached group of *Z. niveum* colonies. Black arrows indicate boundary-layer flow. Arrows within the group of ciliate colonies indicate the feeding currents of the zooids.

the conduits with fully oxygenated seawater adjacent to the peat surface.

Given our results, we envision these stages in colony development. Flow across a sulfide-rich conduit that is not surrounded by ciliate colonies will draw some sulfide out of the conduit by viscous entrainment (Vogel 1996), attracting the motile swarmer stages of *Z. niveum*, which settle preferentially in the chemocline around such sources of reduced sulfur (M. Pöhn, K.V., and J.O. unpubl. data). As colonies grow larger, they interact more strongly with boundary-layer flow. By continuity, the flow will accelerate as it passes over and around the colonies. Resulting pressure differences should cause upwelling on the downstream face of the groups. As a result, the deoxygenated, H_2S-containing seawater in the conduit is transported along the ciliate colonies (Fig. 6). Flux of H_2S from a conduit should increase with the size and number of colonies around the conduit opening, because pressure differences would increase. The periods of reduced speed during flow reversals facilitate the transport of oxygenated seawater toward the outer surface of the zooids by the feeding current of the ciliates and allow recharge of the conduit void with H_2S by molecular diffusion from the tissue and the bark of the decomposing rootlet. In this model, the ectobiotic bacteria of *Z. niveum* are exposed to a rapid, cilium-generated current (the feeding current of the zooids) that alternately transports H_2S-rich and O_2-rich seawater. We suggest that these bacteria overcome the diffusion limitations of their substrate supply by a combination of two transport mechanisms: (1) a pulsed advection of H_2S-rich seawater caused by interaction of the boundary-layer flow with the ciliate groups and (2) the continuous and rapid feeding current of the host. We hypothesize that the recharge of the conduits with H_2S during periods of reduced flow speed is crucial for the maintenance of this symbiosis, so continuous flow artificially applied to ciliate groups would remove the colonies' white appearance. The fact that the flow in this particular mangrove habitat is oscillating is not necessary to our model. All that is required is quiescent periods between distinct flow periods—that is, this type of symbiosis can occur in habitats that do not have reversing flow.

Small-scale, pulsed microcirculations of oxygenated near-bottom water and sulfidic pore fluid have also been reported from the hydrothermal vent fields of Guaymas Basin, Gulf of California (Gundersen et al. 1992). In that case, the advective transport is driven by magmatic intrusion below 400-m-thick deposits. It increases the supply of substrate to communities of the sulfur-oxidizing bacterium *Beggiatoa* spp. Increased nutrient supply can also result from mass flow caused by the behavior of bacteria. For example, the sulfur-oxidizing bacterium *Thiovulum majus* forms veils on the sediment that generate the transport of oxygenated seawater through the 0.5-mm-thick water layer above the veil at rates ~40 times higher than that of molecular diffusion (Fenchel and Glud 1998). In the case we report, a combination of behaviorally and physically mediated transport mechanisms—the feeding current generated by the ciliate host and the pulsed release of sulfide due to distinct periods of flow over ciliate groups interrupted by periods quiescence—can sustain rapid growth of both the ciliate host and its ectosymbiotic sulfur-oxidizing bacteria. This discovery raises the possibility that other shallow-water systems where pockets of decay are bathed in pulsating flow could support similar symbioses.

References

BAUER-NEBELSICK, M., C. F. BARDELE, AND J. A. OTT. 1996*a*. Electron microscopic studies of *Zoothamnium niveum* (Hemprich & Ehrenberg, 1831) Ehrenberg 1838 (Oligohymenophora, Peritrichida), a ciliate with ectosymbiotic, chemoautotrophic bacteria. Eur. J. Protistol. **32:** 202–215.

———, ———, AND ———. 1996*b*. Redescription of *Zoothamnium niveum* (Hemprich & Ehrenberg, 1831) Ehrenberg, 1838 (Oligohymenophora, Peritrichida), a ciliate with ectosymbiotic, chemoautotrophic bacteria. Eur. J. Protistol. **32:** 18–30.

FENCHEL, T., AND B. J. FINLAY. 1989. *Kentrophoros:* A mouthless ciliate with a symbiotic kitchen garden. Ophelia **30:** 75–93.

———, AND R. N. GLUD. 1998. Veil architecture in a sulphide-oxidizing bacterium enhances countercurrent flux. Nature **394:** 367–369.

GIERE, O., R. WINDOFFER, AND E. C. SOUTHWARD. 1995. The bacterial endosymbiosis of the gutless nematode *Astomonema southwardorum:* Ultrastructural aspects. J. Mar. Biol. Assoc. U.K. **75:** 153–164.

GUNDERSEN, J. K., B. B. JØRGENSEN, E. LARSEN, AND W. JANNASCH. 1992. Mats of giant sulphur bacteria on deep-sea sediments due to fluctuating hydrothermal flow. Nature **360:** 454–456.

JEROSCHEWSKI, P., C. STEUCKART, AND M. KÜHL. 1996. An amperometric microsensor for the determination of H_2S in aquatic environments. Anal. Chem. **68:** 4351–4357.

JONES, M. L. 1984. The giant tube worms. Oceanus **27:** 47–52.

LA FOND, E. C. 1967. Movements of benthonic organisms and bottom currents as measured from the bathyscaph Trieste, p. 295–302. *In* J. B. Hersey [ed.], Deep-sea photography. Johns Hopkins Univ. Press.

OTT, J. A. 1995. Sulfide symbioses in shallow sands, p. 143–147.

In A. Eleftheriou, A. D. Ansell, and C. H. J. Smith [eds.], Biology and ecology of shallow coastal waters. Olsen & Olsen.

———, M. BRIGHT, AND F. SCHIEMER. 1998. The ecology of a novel symbiosis between a marine peritrich ciliate and chemoautotrophic bacteria. PSZN Marine Ecology **19:** 229–243.

———, AND R. NOVAK. 1989. Living at an interface: Meiofauna at the oxygen/sulfide boundary of marine sediments, p. 415–422. *In* J. S. Ryland and P. A. Tyler [eds.], Reproduction, genetics and distribution of marine organisms. Olsen & Olsen.

———, G. RIEGER, R. RIEGER, AND F. ENDERES. 1982. New mouthless interstitial worms from the sulfide system: symbiosis with prokaryotes. PSZN Marine Ecology **3:** 313–333.

PAULL, C. K., AND OTHERS. 1984. Biological communities at the Florida escarpment resemble hydrothermal vent taxa. Science **226:** 965–967.

POLZ, M. F., AND C. M. CAVANAUGH. 1995. Dominance of one bacterial phylotype at a midatlantic ridge hydrothermal vent site. Proc. Natl. Acad. Sci. USA **92:** 7232–7236.

REID, R. G. B. 1980. Aspects of the biology of a gutless species of *Solemya* (Bivalvia; Protobranchia). Can. J. Zool. **58:** 386–393.

REVSBECH, N. P. 1989. An oxygen microsensor with a guard cathode. Limnol. Oceanogr. **34:** 474–478.

RÜTZLER, K., AND I. G. MACINTYRE. 1982. The habitat distribution and community structure of the barrier reef complex at Carrie Bow Cay, Belize, p. 9–45. *In* K. Rützler and I. G. Macintyre [eds.], The Atlantic barrier reef ecosystem at Carrie Bow Cay, Belize, I: Structure and communities. Smithsonian Institution Press.

SMITH, D. C. 1979. From extracellular to intracellular: The establishment of a symbiosis. Proc. R. Soc. Lond. B **204:** 115–130.

Southward, E. C. 1982. Bacterial symbionts in Pogonophora. J. Mar. Biol. Assoc. U.K. **62:** 889–906.

SUESS, E., B. CARSON, S. D. RITGER, J. C. MOORE, M. L. JONES, L. D. KULM, AND G. R. COCHRANE. 1985. Biological communities at vent sites along the subduction zone off Oregon. Bull. Biol. Soc. Wash. **6:** 475–484.

VOGEL, S. 1996. Life in moving fluids. The physical biology of flow, 2nd ed. Princeton Univ. Press.

VOPEL, K., C. H. REICK, G. ARLT, M. PÖHN, AND J. A. OTT. 2002. Flow microenvironment of two marine peritrich ciliates with ectobiotic chemoautotrophic bacteria. Aquat. Microb. Ecol. **29:** 19–28.

WINDOFFER, R., AND O. GIERE. 1997. Symbiosis of the hydrothermal vent gastropod *Ifremeria nautilei* (Provannidae) with endobacteria—structural analyses and ecological considerations. Biol. Bull. Mar. Biol. Lab. Woods Hole **193:** 381–392.

Received: 4 December 2003
Amended: 6 July 2004
Accepted: 28 August 2004

Limnol. Oceanogr., 49(3), 2004, 884–889

The timing of benthic copepod emergence

Abstract—We investigated emergence of marine benthic harpacticoid and cyclopoid copepods from subtidal sediment into the bottom water. Previous studies that used traps in the field found that copepods emerged from the sediment within 2 h of dusk. We examined emergence in 20-min sampling periods over 13 h from 1200 to 0100 h in a laboratory flume under conditions of constant flow speed. The light intensity was adjusted to field conditions every 20 min. We observed a peak in emergence during the 20-min sampling period after the onset of darkness, greatly increasing the accuracy with which the timing of emergence is known. This result will help to set the stage for studies of emergence cues.

Temporary emergence of benthic animals into the water column (hereafter emergence) characterizes many taxa, including amphipods (DeWitt 1987), copepods (Walters and Bell 1986), benthic ostracods, and platyhelminthes (Armonies 1988*a*). Copepods were the focus of the experiment reported here because they are the predominant meiofaunal emergers (Walters 1988; Armonies 1989), emerging in abundances of >50,000 individuals m^{-2} d^{-1} in some locations (Thistle 2003).

Emergence of benthic copepods plays a role in benthic–pelagic coupling because benthic copepods that feed in the water column and return to the seabed bring water column resources to the benthos, and benthic copepods in the water column that are consumed by pelagic predators move benthic resources into the water column (Walters and Bell 1986). Also, emergence has important consequences for copepod ecology. Emerging copepods are entrained in water flow and do not return to the same location they left (Service and Bell 1987; Palmer 1988). This displacement affects the organization of the copepod community and might explain the high recolonization rates of defaunated patches (Palmer and Gust 1985).

Copepod emergence has been studied on a variety of temporal scales, including seasonal, lunar, and tidal, but the diel emergence cycle has been a particular focus. Armonies (1989) found that more copepods emerged during the night than during the day. Several studies have measured emergence of harpacticoid copepods at 6-h intervals and found higher abundances in the water column during night and the highest rate of emergence during sunset (Walters and Bell 1986; *but see* Hicks and Coull 1986 for an exception). Walters (1988, 1991) and Walters and Bell (1994), who observed emergence patterns at 2-h intervals, found that the sunset sampling period had the highest number of emergers. Their results suggest that emergence peaks during the 2-h period beginning at dusk, but this level of resolution could be inadequate to elucidate the cues for this behavior. Environmental conditions that have been shown to influence copepod emergence, such as the intensity of the incident light and pore-water oxygenation (Armonies 1988*b*), change rapidly over periods much shorter than 2 h (Revsbech et al. 1981). The correlation of changes in the chemical and physical conditions in the habitat with copepod emergence can be better discerned if behavior and environmental conditions are examined as nearly as possible on the same timescale. Greater resolution of the timing of copepod emergence is therefore needed. Our goal was to study the emergence of benthic copepods at a temporal resolution of 20 min, higher than any used previously, to set the stage for studies of cues and causes.

Material and methods—Location: The study site was on the north Florida shelf (29°52.169′N; 084°26.428′W) in the Gulf of Mexico at a water depth of 5 m. The seabed was unvegetated, well-sorted, medium sand with a mean grain size of 0.38 ± 0.02 mm (n = 5, Fig. 1a). The water content was 25.07 ± 2.94%; organic material was 0.77 ± 0.14%. Wave orbital motion reached the seafloor episodically during periods of high wind speed. Under continuing wave action, oscillating bottom currents generated sediment ripples. The site was defined by two permanent, parallel, 10-m transect ropes separated by 3 m (area = 30 m^2). The transect lines and a movable, 3-m cross-line were marked every 10 cm, forming a Cartesian coordinate system for sampling. The diel light regime at the sediment surface was determined by measurement of the photosynthetically active radiation (PAR, 400–700 nm) with an underwater quantum sensor (LI-192SA, LI-COR Environmental). The sensor housing was buried such that the sensing head was coplanar with the sediment surface. A LI-1000 data logger recorded the mean light intensity averaged over 5 min and the minimum and maximum light intensity from 0200 h on 21 September to 0200 h on 25 September 2001. These measurements revealed that onset of darkness at the sediment surface occurred at ~1845 h and that the average daily maximum intensity of the incident PAR was 217 ± 78 μmol quanta m^{-2} s^{-1}. A sample measurement is shown in Fig. 1b. A miniature data logger (StowAway Tidbit, Onset Computer Corporation) deployed at the sediment surface recorded the seawater temperature from 20 September to 29 November 2001. The highest temperature of 28.6°C was measured on 23 November; the lowest temperature was 17.25°C on 30 October (Fig. 1c).

Laboratory flume: The flume described in Foy and Thistle (1991) was used with some modifications. The seawater in the flume (~1,000 liters, 30-μm filtered) was adjusted to in situ temperature with a chiller (Aquatic Ecosystems part AE7D) and to in situ salinity with Instant Ocean®. Three sediment samples in black-painted acrylic tubes (15.5 cm^2 × 10 cm, *see below* for sampling procedure) were inserted 50 cm from the outflow of the duct, 4 cm apart in the center of the duct (5 m long, 0.5 m wide), on a line perpendicular to the flow. After the sediment samples were inserted, seawater flowed from the head tank through a T-shaped diffuser

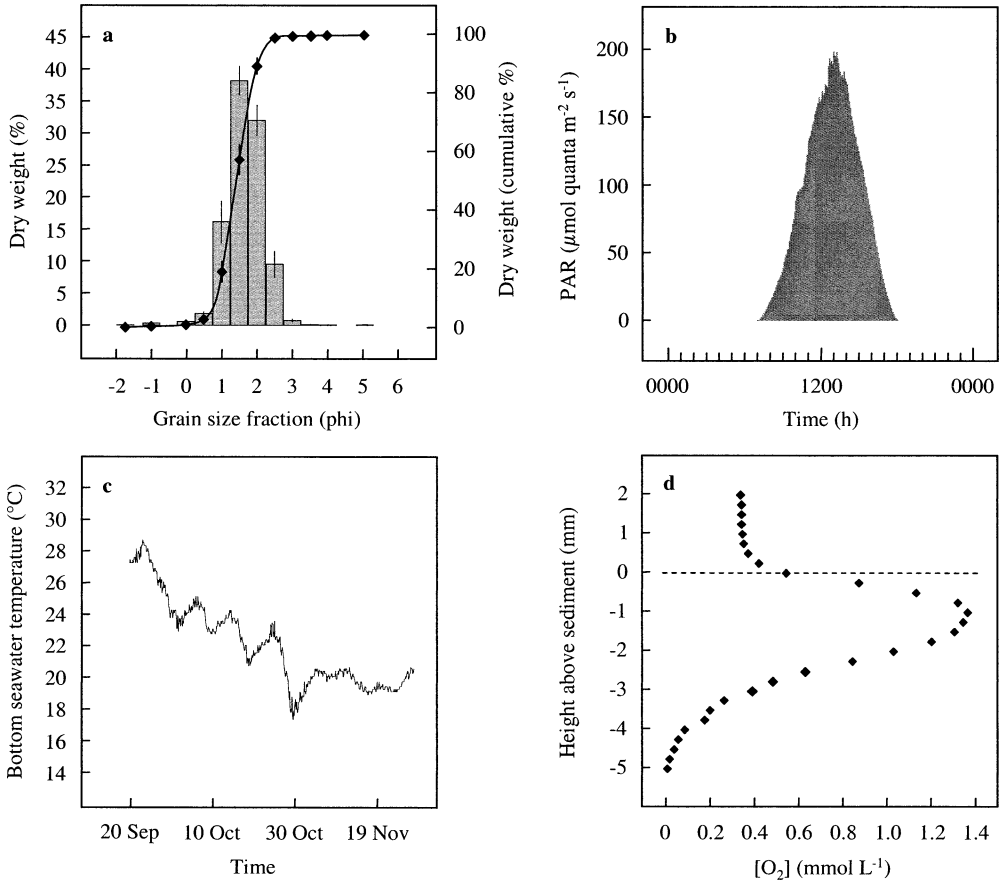

Fig. 1. Abiotic parameter at the sampling site. (a) The grain size distribution for the upper 6-mm-thick sediment layer. The bars represent the dry weight, and the line represents the cumulative dry weight. The error bars are ±1 SD. (b) PAR at the sediment surface from 0000 h on 10 Nov to 0000 h on 11 Nov 2001. The intensity of PAR was maximal at ~1400 h and decreased essentially linearly until sunset. (c) Bottom seawater temperature from 20 Sep to 29 Nov 2001. (d) Vertical $[O_2]$ profile measured on 9 Nov 2001 between 1250 and 1350 h at 130 ± 10 μmol quanta m^{-2} s^{-1} PAR and a temperature of 20.5°C. The dashed line represents the sediment surface.

and a flow straightener to fill the duct to a depth of 8 cm. A removable sieve with 30-μm mesh was located in the outflow below the duct. Copepods that left the sediment were swept away by the flow and caught in the sieve. The flow speed was much slower than needed to erode the sediment. To characterize the seawater flow above the surface of the sediment sample, we measured flow-speed microprofiles with a microelectrode (FS20, Unisense A/S; *see* Vopel et al. 2002). The flow speed microelectrode and O_2 microelectrodes (*see below*) were mounted on a micromanipulator (Märzhäuser Wetzlar) driven by stepping motors and moved vertically by a wired remote control in 200-μm increments.

Light regime: We chose a light regime that was representative of a typical day at the field site. A 750-watt halogen light (ETC Source Four) was suspended 50 cm above the test sediment. We placed a blue filter gel of known spectral properties (Rosco Filter #69, Brilliant Blue) in front of the light to simulate the light spectrum at 5 m depth. To measure the intensity of the PAR in the flume, we inserted the light sensor into a corer hole and filled the flume with 8 cm of seawater. We repeated this procedure for each corer hole, and we could not detect a difference among them. During the experiment, light intensity was held constant at 200 μmol quanta m^{-2} s^{-1} for the first hour (from 1200 h until 1300 h) and then decreased in a stepwise fashion by 11 μmol quanta m^{-2} s^{-1} every 20 min until 1840 h, when the light was switched off.

Sediment pore-water oxygenation: To assess our ability to mimic geochemical conditions, we measured profiles of pore-water $[O_2]$ with microelectrodes (OX50, Unisense A/S; Revsbech 1989) across the sediment–water interface in the field and in the flume. The output current was measured and converted to a millivolt signal by an underwater picoammeter (PA3000U, Unisense A/S) and transferred to a data logger (OM-3000, Omega® Engineering). For the field measurements, a manually operated micromanipulator (Märzhäuser Wetzlar) was attached to an aluminum post that had been driven into the sediment.

Sediment sampling: Seven replicates of the experiment were carried out on different days (five in October and two

Table 1. The number of copepods that were caught in the sieve and the number of copepods that remained in the cores over seven replicates. The former values are based on the number caught divided by the surface area of the three cores (=46.5 cm^{-2}) and then normalized to 10 cm^{-2}. Note that sieve values were estimated from three cores but that sediment values were estimated from only one of the three.

	Copepods (individuals per 10 cm^{-2})							
	1	2	3	4	5	6	7	Mean±SD
In sieve	91.6	104.3	123.9	126.0	73.1	111.6	98.7	104.2±17.2
In sediment (mm)								
0–2	11.6	45.8	107.7	139.4	63.2	82.6	106.5	79.5±39.9
2–4	6.5	3.2	23.9	11.0	76.1	123.9	12.9	36.8±42.4
4–6	3.2	7.7	17.4	29.7	47.7	70.3	51.6	32.5±23.1
6–8	5.8	4.5	16.1	23.9	53.5	67.1	34.2	29.3±22.1
8–10	11.6	0.6	7.7	15.5	20.0	39.4	9.7	14.9±11.4
10–20	110.3	13.5	74.2	40.0	12.9	121.9	39.4	58.9±41.0
20–30	65.2	12.3	94.2	85.5	85.8	97.4	25.8	66.6±31.8
30–40	43.9	46.5	81.9	86.5	51.0	89.0	38.1	62.4±20.7
Total in sediment	258.1	134.2	423.2	431.6	410.3	691.6	318.1	381.0±161.1
Total	349.7	238.5	547.1	557.6	483.4	803.2	416.8	485.2±166.5

in November 2001). For a given replicate, scuba divers took three cylindrical sediment samples at random from the study site between 0910 h and 0926 h, each 15.5 cm^2 by 10 cm deep. Thereafter, temperature and pH, [O_2], and salinity of the bottom water were measured with PortaMess 912 (Knick), Oxi 196, and LF23 (WTW) meters, respectively. During transit, the sediment samples were kept in a seawater bath at approximately in situ temperature and light intensity. A filter of the same type used in the flume covered the bath to mimic the in situ spectrum of the PAR. The sediment samples were in place in the laboratory flume <60 min after collection and before 1200 h (Eastern Daylight Time). At that time, the light was set to deliver 200 μmol quanta m^{-2} s^{-1} PAR, which corresponded to typical noon intensity at the seafloor of the sampling site (*see below*).

Flume sampling: We collected the copepods that had been caught in the sieve every 20 min for 13 h starting at 1200 h. For each 20-min period, temperature, salinity, and pH of the seawater directly upstream of the sediment sample were measured as in the field. All animals caught on a sieve were rinsed off and preserved in sodium borate–buffered, 30-μm–filtered seawater formaldehyde (9:1, v/v). At 0100 h, we selected one sediment sample at random for further analysis. The sediment was sliced at 2-mm intervals for the first centimeter and at 10-mm intervals for the second through fourth centimeters. The slices were preserved as above. All samples were stained in rose Bengal, and harpacticoid and cyclopoid copepods were removed under a dissecting microscope. The harpacticoids were separated into adults and juveniles, and the adult harpacticoids were separated by sex.

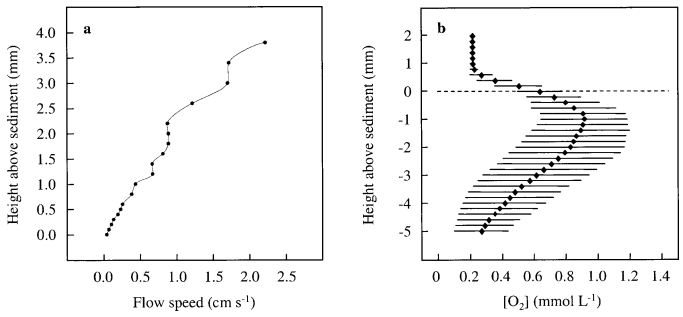

Fig. 2. Abiotic parameter in the flume. (a) Microprofile of flow speed above a sediment sample. (b) Average vertical [O_2] profile calculated from profiles that were measured across the sediment–water interface of five sediment cores at 1215 h when the light was 200 μmol quanta m^{-2} s^{-1}. The error bars are ±1 SD. The dashed line represents the sediment surface.

Results—Abiotic parameters in situ: During sampling, the temperature of the bottom seawater ranged from 18°C to 23°C, the salinity from 32 to 35, the pH from 8.1 to 8.2, and [O_2] from 230 to 244 μmol L^{-1}. Onset of darkness (as measured at the sediment surface) during the study occurred between 1815 and 1830 h. From 21 October to 13 November 2001, the maximum intensity of PAR ranged between 197 and 229 μmol quanta m^{-2} s^{-1} at the sediment surface. We measured the [O_2] in the sediment pore water in the field on 9 November 2001 between 1250 and 1350 h. The weather was calm, and the light intensity at the sediment surface was 130 ± 10 μmol quanta m^{-2} s^{-1}. The [O_2] was highest (1,362 μmol L^{-1}) at 1 mm below the sediment surface (Fig. 1d) and decreased to 5 μmol L^{-1} at 5 mm below the sediment surface, the greatest depth measured.

Abiotic parameters in the laboratory flume: The temperature of the seawater in the flume ranged from 17°C to 23°C, the salinity from 32 to 34, the pH from 7.9 to 8.1, and the [O_2] from 219 to 262 μmol L^{-1}. The flow in the flume was laminar and unidirectional, increasing in speed from ~0 cm s^{-1} at the sediment surface to 2.2 cm s^{-1} 3.8 mm above the sediment surface (Fig. 2a). An average [O_2] microprofile across the interface between the sediment sample and the flume seawater is shown in Fig. 2b. This profile was calculated from five [O_2] profiles (one profile each for five of the seven replicates), taken at 1215 h when PAR was 200 μmol quanta m^{-2} s^{-1}. The average [O_2] was highest at 1 mm

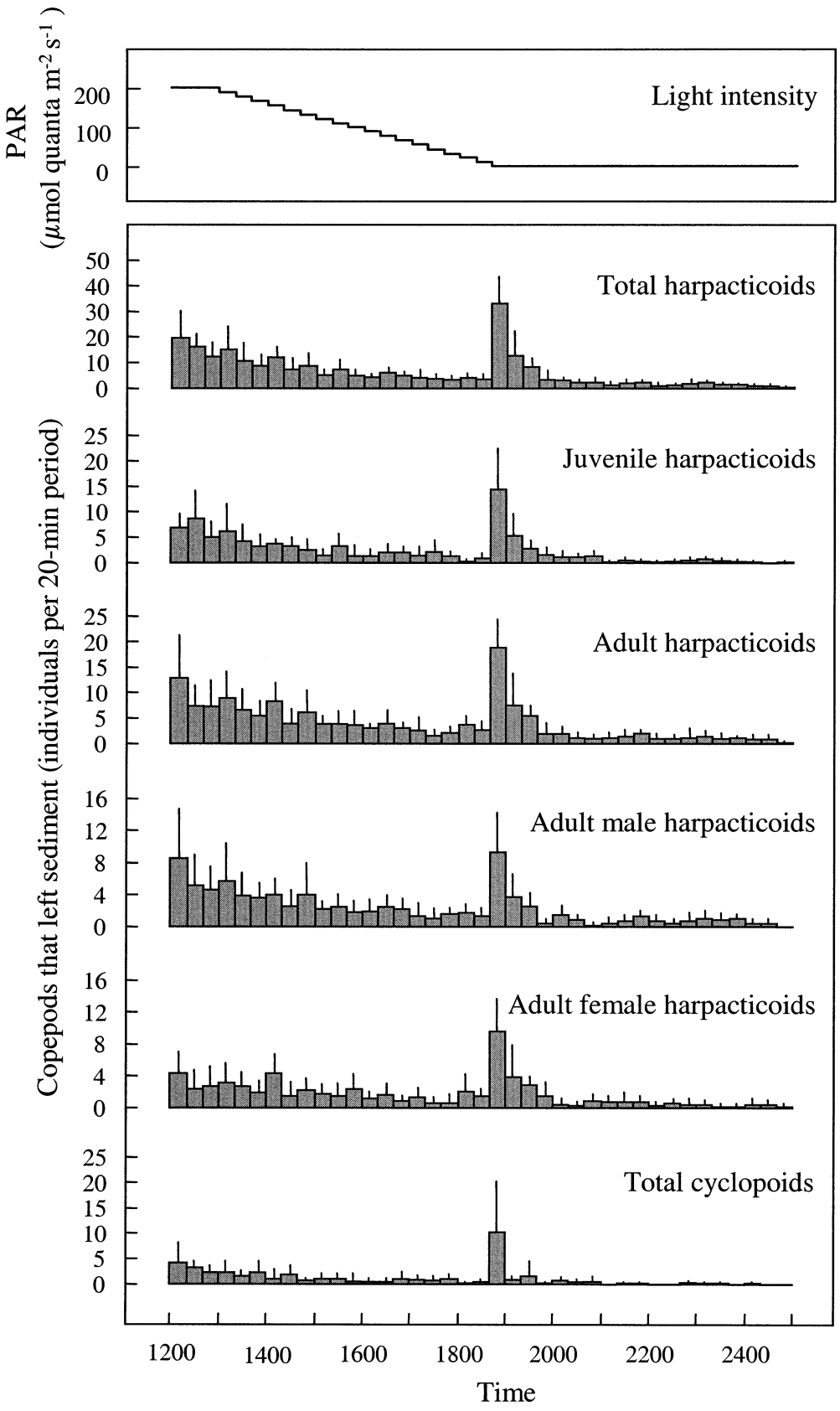

Fig. 3. Average number (n = 7) of all harpacticoids combined—juvenile harpacticoids, adult harpacticoids, adult male harpacticoids, adult female harpacticoids—and total cyclopoids that left the sediment during each 20-min sampling period.

depth (915 μmol L^{-1}) and decreased to 269 μmol L^{-1} at 5 mm depth.

Copepod emergence: The sediment contained an average of 485 ± 167 copepods 10 cm^{-2} (n = 7), of which an average of 104 ± 17 individuals per 10 cm^2 (21.5%) left the sediment during the experiment (Table 1). The upper 10-mm-thick layer of the sediment samples had the highest number of copepods, and within that layer, the 0–2-mm layer had the most. The numbers of individuals that were caught in the sieve were divided into six categories and are presented in Fig. 3. Of all the copepods that left the sediment, an average of 78% ± 6% were harpacticoids, and an average of 52% ± 8% of those were adults. The male to female ratio of adult harpacticoids was 1 : 0.7. Very few cyclopoids were found in the sediments at the end of the experiment.

Timing of emergence: The sampling period during which the most copepods left the sediment was from 1840 to 1900 h (15.2% of those that left the sediment between 1200 and 0100 h), the first interval when the PAR intensity was 0 μmol quanta m^{-2} s^{-1}. This pattern is the same for total harpacticoids, adult harpacticoids, adult male harpacticoids, adult female harpacticoids, juvenile harpacticoids, and cyclopoids (Fig. 3). During this sampling period, 76% of the animals leaving the sediment were harpacticoids, 57% of which were adults of which 49% were male. The 20-min segment during which the second highest number of copepods left the sediment was at 1200–1220 h (8.3% of those that left the sediment between 1200 and 0100 h). This period was followed by a steady decrease in the number of copepods caught in the sieve per 20-min interval until 1840 h.

Discussion—Benthic copepod emergence: Although our approach allowed a more detailed temporal assay than had been done previously, interpretation of our results was not straightforward. Our procedures collected animals that left the cores because they emerged but also collected animals that left the cores inadvertently. That is, the normal movements of benthic copepods would be expected to take them, from time to time, to the sediment–water interface and to the edge of the core, where they risk being transported by the flow onto the flume bed and then into the sieve. Thus, an animal in our sieve could have been collected because it emerged or because it was inadvertently caught in the flume flow.

Inspection of Fig. 3 reveals three groups of sampling periods, those before 1840 h (PAR was decreased from 11 to 0 μmol quanta m^{-2} s^{-1} at 1840 h), those from 1840 to 1940 h, and those after 1940 h. The first and third groups can be seen to form a trend that is interrupted by the second group. We suggest that the trend arises from the steady loss (= background loss) of copepods from our cores. The decrease in the number lost per 20-min period is reasonable because no source of benthic copepods was available to replace those lost. The results for the periods between 1840 and 1940 h must be explained differently. From the work of Walters and Bell (1986) and Walters (1991), an emergence peak near sunset was expected. We interpret the excess of benthic copepods collected above background between 1840 and 1940 h as emergence.

The resolution of previous studies was on the scale of hours. Our 20-min timescale results revealed a single peak in benthic copepod emergence. The emergence peak began at local darkness, it was less than 1 h in duration, and the largest number of copepods emerged during the first 20-min period (i.e., 1840–1900 h). Using a shorter sampling period, we might have found that the duration of the emergence peak is even shorter. From Fig. 3, the emergence peak appears to be a response to light or to a factor indirectly controlled by light, such as pH or pore-water [O_2]. If so, then the timing of the peak will depend on the rate of light attenuation at the seabed and should vary with depth, water clarity, and season.

To begin to assess the ecological consequences of benthic copepod emergence, we estimated the number of copepods that emerged during the 1-h peak. To do so, we estimated the amount of background loss during each of the three 20-min periods that constituted the peak and subtracted those values from the observed number of animals collected during the corresponding periods. The background losses in the periods adjacent to the peak differed little. We therefore calculated a linear regression based on the four periods immediately before the peak and the four periods immediately after the peak. (The regression results changed very little if a few more points around the peak were included.) We found that ~12,000 copepods m^{-2} emerged during the 1-h peak. (This estimate is likely conservative because copepods inadvertently lost before 1840 h might have emerged between 1840 and 1900 h.) This value is similar to the 10^4–10^5 copepods m^{-2} Walters and Bell (1994) found leaving the sediment during their 2-h, postsunset sampling periods, suggesting that a substantial flux of benthic copepods occurs predictably in a relatively short time in some coastal waters. This flux appears to create an opportunity for water column predators at the onset of darkness. If so, emergence would contribute to benthopelagic coupling. In a different vein, benthic copepods apparently participate in pore-water mixing as other meiofauna and microfauna do, thereby stimulating microbial mineralization (Aller and Aller 1992; Glud and Fenchel 1999; Rysgaard et al. 2000). After large numbers of copepods leave the sediment in the hour after the onset of darkness, the intensity of pore-water mixing is likely to be reduced and with it, the rates of solute transport and the microbial mineralization.

Our discoveries about the timing of emergence will allow investigations of emergence cues to be focused on the time around dusk. Future experiments must confront the problem that light might be a direct cue, an indirect cue (via pore-water chemistry), or a combination of the two. That is, manipulative experiments will be needed to decouple light intensity from the other parameters that could cue emergence.

Michael Teasdale

Department of Oceanography
Florida State University
Tallahassee, Florida 32306-4320

[1] Corresponding author (k.vopel@niwa.co.nz).

Kay Vopel[1]

National Institute of Water and Atmospheric Research
P.O. Box 11-115
Hamilton, New Zealand

David Thistle

Department of Oceanography
Florida State University
Tallahassee, Florida 32306-4320

References

ALLER, R. C., AND J. Y. ALLER. 1992. Meiofauna and solute transport in marine muds. Limnol. Oceanogr. **37:** 1018–1033.

ARMONIES, W. 1988*a*. Active emergence of meiofauna from intertidal sediment. Mar. Ecol. Prog. Ser. **43:** 151–159.

———. 1988*b*. Physical factors influencing active emergence of meiofauna from boreal intertidal sediment. Mar. Ecol. Prog. Ser. **49:** 277–286.

———. 1989. Meiofaunal emergence from intertidal sediment measured in the field: Significant contribution to nocturnal planktonic biomass in shallow waters. Helgol. Mar. Res. **43:** 29–43.

DEWITT, T. H. 1987. Microhabitat selection and colonization rates of a benthic amphipod. Mar. Ecol. Prog. Ser. **36:** 237–250.

FOY, M. S., AND D. THISTLE. 1991. On the vertical distribution of a benthic harpacticoid copepod: Field, laboratory, and flume results. J. Exp. Mar. Biol. Ecol. **153:** 153–163.

GLUD, R. N., AND T. FENCHEL. 1999. The importance of ciliates for interstitial solute transport in benthic communities. Mar. Ecol. Prog. Ser. **186:** 87–93.

HICKS, G. R. F., AND B. C. COULL. 1986. Distribution and behavior of meiofaunal copepods inside and outside seagrass beds. Mar. Ecol. Prog. Ser. **31:** 159–170.

Acknowledgments

I. Hoedl, L. Sedlacek, and K. Suderman helped in the design and running of the experiment and C. Hippolyte, G. Hurst, L. Sedlacek, and A. Vopel helped with the sorting. The comments of A. B. Thistle improved the manuscript. This research was supported by ONR grant N00014-00-1-007.

PALMER, M. A. 1988. Dispersal of marine meiofauna: A review and conceptual model explaining passive transport and active emergence with implications for recruitment. Mar. Ecol. Prog. Ser. **48:** 81–91.

———, AND G. GUST. 1985. Dispersal of meiofauna in a turbulent tidal creek. J. Mar. Res. **43:** 179–210.

REVSBECH, N. P. 1989. An oxygen microelectrode with a guard cathode. Limnol. Oceanogr. **34:** 472–476.

———, B. B. JØRGENSEN, AND B. B. BRIX. 1981. Primary productivity of microalgae in sediments by oxygen microprofile, $H^{14}CO_3^-$ fixation, and oxygen exchange methods. Limnol. Oceanogr. **26:** 717–720.

RYSGAARD, S. P., P. B. CHRISTENSEN, M. V. SØRENSEN, P. FUNCH, AND P. BERG. 2000. Marine meiofauna and nitrogen mineralization in sandy and soft sediments of Disko Bay, West Greenland. Aquat. Microb. Ecol. **21:** 59–71.

SERVICE, S. K., AND S. S. BELL. 1987. Density-influenced active dispersal of harpacticoid copepods. J. Exp. Mar. Biol. Ecol. **114:** 49–62.

THISTLE, D. 2003. Harpacticoid copepod emergence at a shelf site in summer and winter: Implications for hydrodynamic and mating hypotheses. Mar. Ecol. Prog. Ser. **248:** 177–185.

VOPEL, K., C. H. REICK, G. ARLT, M. PÖHN, AND J. A. OTT. 2002. Flow microenvironment of two marine peritrich ciliates with ectobiotic chemoautotrophic bacteria. Aquat. Microb. Ecol. **29:** 19–28.

WALTERS, K. 1988. Diel vertical migration of sediment-associated meiofauna in subtropical sand and seagrass habitats. J. Exp. Mar. Biol. Ecol. **117:** 169–186.

———. 1991. Influence of abundance, behavior, species composition, and ontogenetic stage on active emergence of meiobenthic copepods in subtropical habitats. Mar. Biol. **108:** 207–215.

———, AND S. S. BELL. 1986. Diel patterns of active vertical migration in seagrass meiofauna. Mar. Ecol. Prog. Ser. **34:** 95–103.

———, AND ———. 1994. Significance of copepod emergence of benthic, pelagic, and phytal linkages in a subtidal seagrass bed. Mar. Ecol. Prog. Ser. **108:** 237–249.

Received: 22 October 2003
Accepted: 5 January 2004
Amended: 18 January 2004

Limnol. Oceanogr., 48(5), 2003, 2034–2045

Effect of the brittle star *Amphiura filiformis* (Amphiuridae, Echinodermata) on oxygen flux into the sediment

Kay Vopel[1]
Alfred Wegener Institute for Polar and Marine Research, Columbusstrasse, D-27568 Bremerhaven, Germany

David Thistle
Department of Oceanography, Florida State University, Tallahassee, Florida 32306-4320

Rutger Rosenberg
Department of Marine Ecology, Göteborg University, Kristineberg Marine Research Station, S-450 34 Fiskebäckskil, Sweden

Abstract

O_2 plays a key role in early sedimentary diagenetic processes, but the effect of most macrofaunal species on the pathways and rates of supply of O_2 into the seabed are not well known. We investigated the effect of the ophiuroid *Amphiura filiformis*, one of the dominant macrobenthic species on soft bottoms in the northeast Atlantic, at depths of ~15–100 m, in a laboratory environment. We determined how the presence of the ophiuroid changed the total O_2 uptake of macrofauna-free sediment by combining measurements from a microcosm approach and an approach that uses microelectrodes and a flushed aquarium. We suggest that natural populations of *A. filiformis* can account for 80% of the total flux of O_2 into the soft bottom. At least 67% of this portion is due to the diffusion of O_2 across additional sediment-water interfaces excavated by the brittle star.

Because O_2 plays a key role in early sedimentary diagenetic processes, pathways and rates of supply of O_2 into the seabed are of interest. Cohesive sediments are supplied with O_2 by molecular diffusion driven by concentration gradients between bottom seawater and the interstitial seawater of the sediment (Gundersen and Jørgensen 1990) and by the advection of seawater as a consequence of infaunal activities (Aller and Yingst 1978; Aller 1980; Gust and Harrison 1981). Larger species create and ventilate burrows and tubes; that is, they expose additional sediment surface area to oxygenated seawater. Many macroinfaunal species continuously rework the sediment and thus increase the oxygenation of the pore water (Marinelli 1992; Krager and Woodin 1993; Rosenberg et al. 1997; Solan and Kennedy 2002). The meiofauna of the surficial sediment and the sediment around macrofaunal burrows apparently contribute to the interfacial flux as well by mixing the pore water through ''random walk'' within the interstitium of the sediment or by irrigating microcavities and microtubes (Meyers et al. 1987; Aller and Aller 1992; Pike et al. 2001).

Estimating the overall contribution of benthic communities to the total O_2 flux is a complex issue. This contribution is a function of, for example, the structure of the benthic community, the sizes of the species, the geometries of their burrows, their modes of burrow ventilation and feeding, and their physiological abilities and survival strategies (e.g., Aller and Yingst 1978; Aller et al. 1983). Species' life histories (population dynamics) and interspecific interactions are additional variables. Larger animals are of particular interest because they can account for the majority of the faunal effect. Populations of the burrowing shrimp *Callianassa subterranea*, for example, can account for 17% of the total oxygen utilization (TOU) of North Sea sediments (de Wilde et al. 1984; Witbaard and Duineveld 1989). Booij et al. (1994) calculated that burrow irrigation by the amphipod *Corophium volutator* and oligochaetes caused ~25% of the total O_2 flux into intertidal sediment of the western Wadden Sea. Forster and Graf (1995) found that *C. subterranea* and the polychaete *Lanice conchilega* increased the TOU of very fine, silty sediment of the Norwegian Trough (698 m, Skagerrak) by 85% over that caused by diffusion across the sediment–water interface. A 2.7-fold increase in solute flux due to the abundant polychaete *Spiochaetopterus* sp. was found by Forster et al. (1999).

Here, we present a laboratory study designed to investigate the impact of the ophiuroid *Amphiura filiformis* (O. F. Müller), one of the dominant macrobenthic species on soft bottoms in the northeast Atlantic at depths of ~15–100 m (O'Connor et al. 1983; Sköld et al. 1994). The population densities of *A. filiformis* are known to be >3,000 individuals m^{-2} (Rosenberg 1976, 1995; Josefson 1995). This brittle star

[1] Corresponding author (k.vopel@niwa.co.nz). Present address: National Institute of Water & Atmospheric Research, P.O. Box 11115, Hamilton, New Zealand.

Acknowledgments

We thank Angelika Vopel and Martina Pöhn for their assistance in the laboratory, Rick Lumpkin and Peter Sorgo for stimulating discussions about analytical geometry, and Peter Berg for a copy of his profile-interpretation procedure. The manuscript benefited from the comments of Kevin R. Carman, Anne B. Thistle, and two anonymous reviewers.

This study was financially supported by the European Union Program ''Training and Mobility of Researchers'' and the Kristineberg Marine Research Station, Sweden.

occupies burrows that extend several centimeters into the sediment. The burrow consists of a disk chamber that is connected to the bottom water through three–four arm channels (Woodley 1975). The size, shape, and positioning of the burrow are consistent, and the inhabitants remain stationary for most of the time (Solan and Kennedy 2002). *A. filiformis* does not move daily in search of food but exhibits density-dependent migratory behavior; that is, the brittle star moves horizontally both on the sediment surface and within the sediment (Rosenberg et al. 1997). Furthermore, this brittle star leaves its position in the sediment during spawning (Woodley 1975) and when $[O_2]$ of the bottom seawater is <13% saturation (Rosenberg et al. 1991).

The arms of an established *Amphiura* serve three main functions: ventilation and respiration, transportation of particles out of the burrow, and the collection of food and its transportation toward the mouth (Ockelmann and Muus 1978). *A. filiformis* usually ventilates its burrow by undulating one arm in the vertical plane (Woodley 1975; Ockelmann and Muus 1978). Undulations pass down the arm from the surface of the sediment toward the disk, forcing water along in the spaces between the upper and lower surface of the arm and the walls of the burrow. The water is drawn down that arm channel to the disk chamber and then flows passively up to the other arm channels. The arms are flanked by arrays of projecting spines to which sediment particles adhere, forming the ''respiratory fringe.'' The fringe blocks the gaps between the lateral spines and thus prevents a displacement of water during undulation and increases the driving effect of the trunk of the arms. The fringe is constructed with the help of the tube feet, which, in contrast to those of other species, stand free of the fringe and can thus transport material along the arm to the mouth while undulation continues (Woodley 1975).

All previous field and laboratory studies on *A. filiformis* have indicated that the brittle star must have a significant impact on the total O_2 flux and thus on the biogeochemical cycling of organic matter in the sediment. The aim of our study was to quantify this effect. We did enclosure experiments with macrofauna-free sediment as well as experiments with a specific number of ophiuroids added. In addition, detailed microelectrode measurements were done directly in the burrow and through burrow walls in an aquarium with flowing water, where in situ boundary-layer flow conditions could be simulated.

Materials and methods

Locality and sampling—In September 2000, a modified USNEL box corer (0.25 m^2) was used to collect organisms and sediment at the mouth of the Gullmarsfjord, west Sweden (58°14.72′N, 11°25.80′E), at 55 m depth. Bottom-water temperatures there vary between 5°C and 12°C, and the salinity is ~34. The sediment is a silty clay with a water content of 73.4% ± 2.1% and a porosity of 0.83 ± 0.04 (mean ±SD, $n = 5$). The grain-size distribution has two dominant size classes. By weight, 47% of the particles are 2–8 μm in diameter (i.e., clay-silt), and 38% are 63–125 μm (i.e., silt–very fine sand) (Sköld et al. 1994).

The sediment in the box corer was gently rinsed with filtered seawater through a 1-mm mesh that removed macrobenthic animals and was used to set up the microcosms and the flushed aquaria described below. During sieving, individuals of the brittle star *A. filiformis* with disk diameters between 6.0 and 7.5 mm were collected with forceps. These individuals were allowed to acclimate for 1 d in a flow-through seawater system filled with sediment from our site at 17 ± 0.2°C in the dark. The seawater used in all experiments was pumped from 35 m depth.

Microcosm setup—Each of 10 plastic cylinders (length, 24 cm; inner diameter, 9.8 cm), closed at the lower ends with rubber stoppers, was filled two-thirds full with sieved sediment from the study site and completely submerged (upright) in a larger tank filled with 30-μm filtered seawater (pH, 8.1; salinity, 32). The upper opening of each cylinder was then closed by an O-ring–sealed lid to which a 4-cm-long, Teflon-coated stirring bar was attached. The stirring bar was rotated at ~10 rpm by a rotating external magnet. This gentle stirring prevented the water column from becoming stagnant but did not cause movement of sediment particles. The lid of each cylinder had two ports to which Teflon tubes were connected. A peristaltic pump (Ismatec Laboratoriumstechnik) constantly moved seawater from the cylinder through the first port to a flow-though cell (AMT) and back into the cylinder through the second port. This closed system could be opened by disconnecting the Teflon tube from the second port so that seawater from the surrounding tank was drawn into the cylinder, through the flow-through cell, and back into the tank. The $[O_2]$ of the seawater in the flow-through cell was continuously measured with a Clark-type O_2 microelectrode (AMT) and a miniaturized picoampere meter (AMT) mounted directly on the microelectrode. The signal was digitized by an analog-to-digital converter (DI 220; Dataq Instruments) and analyzed with the software WinDaq/Lite (Dataq Instruments).

Microcosm measurements—The following procedure was repeated for each microcosm. We brought $[O_2]$ in the microcosm to steady state by opening the circulation system (see above). Once the $[O_2]$ was stable, the system was closed, and the decrease of the $[O_2]$ in the seawater of the microcosm was measured for 3 h. Subsequently, the system was opened, to allow flushing with oxygenated seawater from the surrounding tank until $[O_2]$ reached saturation (after ~2 h). Thereafter, 10 of the reserved specimens of *A. filiformis* rinsed with 0.7-μm filtered seawater were added to the microcosm yielding a density that corresponded to 1,326 individuals m^{-2}, a realistic natural density. Two hours after the brittle stars had buried themselves, the system was closed, and the decrease of the $[O_2]$ in the seawater of the cylinder was measured again for 3 h. All measurements were made in darkness at 17 ± 0.2°C. Afterward, the number of openings per burrow and the number of extended arms per individual were estimated visually. The TOU of the microcosm in each treatment was calculated from the rate of decrease of $[O_2]$ in the seawater above the sediment and the volume of the overlying seawater. The rate of decrease in $[O_2]$ was obtained by linear regression of the $[O_2]$ curve ($R^2 > 0.937$).

Respiration rate of A. filiformis—Each group of 10 adult specimens of *A. filiformis* was removed from its cylinder, rinsed in 0.7-μm filtered seawater, and transferred to a 100-ml flask filled with normoxic, 0.7-μm filtered seawater (pH, 8.1; temperature, 17 ± 0.2°C; salinity, 32). No sediment was added. We measured the $[O_2]$ in the flask at the beginning and at the end of a 4-h (dark) incubation with the O_2 microelectrode by circulating the seawater between the flask and the flow-through cell. Flasks of filtered seawater served as controls. The average individual respiration rate was calculated from the volume of the seawater in a flask and the decrease in its $[O_2]$. The wet weight and dry weight of the average individual were determined for each of the 10 groups of *A. filiformis*. For wet weight, the 10 brittle stars in each group were rinsed in 0.7-μm filtered seawater, transferred onto a sieve, and weighed. For dry weight, the individuals in each group were rinsed with distilled water, dried at 70°C for 24 h, and weighed again.

Experiments in flow aquaria—Two small aquaria (19 × 6 × 10 cm) were completely filled with sieved sediment from the study site. These aquaria were submerged in a larger, 60-cm-long aquarium (25 × 10 cm) filled with seawater (temperature, 17 ± 0.2°C; salinity, 32) and equipped with an outflow on one side and an inflow on the other. The in- and outflow were connected with silicon tubes to a reservoir holding 200 liters seawater that was continuously bubbled with air. This seawater was pumped from the reservoir to the aquarium at a rate of 2.16 ± 0.03 L min^{-1} ($n = 5$) and returned to the reservoir by gravity. The resulting flow in the aquarium, measured by tracking of particles ~5 cm above the sediment surface, was ~2 cm s^{-1}. After six $[O_2]$ microprofiles across the sediment–water interface had been measured (see below), 5–10 specimens of *A. filiformis* were placed on the sediment surface of each small aquarium, whereupon they burrowed into the sediment within a few minutes. Some burrows were visible though the sides of the aquaria, so an arm or the disk could be observed. The brittle stars were not fed.

Microelectrode setup—Spatial and temporal variations in $[O_2]$ of the sediment–water interface and in the burrows of *A. filiformis* were recorded with a Clark-type O_2 microelectrode (MasCom) mounted on a micromanipulator (Märzhäuser) driven by remotely controlled stepping motors and secured to a stable support. The electrode current, measured by a miniaturized picoammeter (MasCom) mounted directly on the shaft of the sensor, was converted to a millivolt signal with a two-channel indication amplifier and digitized by an analog-to-digital converter (DI 220; Dataq Instruments) for data acquisition. The sensor was calibrated at the experimental temperature. Seawater from the tank that had been saturated with O_2 by air bubbled into it was the standard for air saturation. An aliquot that had been nitrogen flushed was the zero-$[O_2]$ standard. A stereomicroscope (SZ60; Olympus) mounted on a tripod was used to observe the movements of the sensor tip near the surface of the sediment and in the burrows of the brittle stars.

Microscale measurements—We measured one high-resolution $[O_2]$ profile across the sediment–seawater interface at six randomly chosen locations in the flushed aquaria by advancing the sensor vertically in 0.2-mm increments. Continuous recordings of $[O_2]$ were made in burrows of *A. filiformis* that were against the walls of the aquaria, so that the position of sensor could be controlled visually. The sensor readings were displayed in real time, and the behavior of the brittle star and the resulting changes in $[O_2]$ were observed at the same time.

A high-resolution $[O_2]$ profile was also measured across the channel lumens of the undulating arms of five individuals (Fig. 1, chord B). In each case a second, parallel profile was measured in the surrounding sediment alone (Fig. 1, chord A). These measurements allowed us to estimate the thickness of the oxic halo around the arm channel, the diameter of the channel lumen, and the O_2 consumption of the surrounding sediment. The tip of the microelectrode crossed the oxic halo and the lumen of an arm channel ~1.5 cm below the sediment surface at an angle (θ) of 45°, parallel to the vertical radius (Y) of the ellipsoid cross section and perpendicular to the horizontal radius (X). Construction of O_2 profiles in a plane normal to the long axis of the lumen required an estimate of the radial distance (x_{bn}) of each measurement from the center of the lumen. The distance (x_b) of chord B from Y was calculated with Eq. 1.

$$x_b = \{[(B/2)^2 - (A/2)^2] \times \cos^2(90° - \theta) - c^2\}/2c \quad (1)$$

where A and B are the lengths of the chords A and B, respectively, and c is the distance between the chords. The distance (r_{bn}) from the center of the ellipsoid cross section to every measuring point (b_n) along chord B could then be determined with Eq. 2.

$$r_{bn} = (y_n^2 + x_b^2)^{1/2} \quad (2)$$

where y_n is the distance from b_n to the intersection of chord B and the x-axis. The distances X and Y from the center of the lumen to the edge of the oxic halo along the x- and y-axis were calculated with Eqs. 3 and 4, respectively.

$$X = [B^2 \times \cos^2(90° - \theta) + x_b^2]^{1/2} \quad (3)$$

$$Y = X/\cos(90° - \theta) \quad (4)$$

Given X and Y, the length (R_{bn}) of any line through b_n connecting the center and the perimeter of the ellipse can be calculated with Eq. 5.

$$R_{bn} = [(X^2 \times Y^2 \times [1 + y_n^2/x_b^2])/(Y^2 + X^2 \times y_n^2/x_b^2)]^{1/2} \quad (5)$$

Finally, the distance r_{bn} was converted to the distance (x_{bn}) in a plane normal to the long axis of the arm channel with Eq. 6.

$$x_{bn} = X \times r_{bn}/R_{bn} \quad (6)$$

For the construction of the $[O_2]$ profiles normal to the long axis of the arm tube (see below), the only measurements used were those taken as the sensor moved from the sediment into the channel lumen (not those taken as the sensor moved from the lumen into the sediment).

Calculation of O_2 flux—The diffusive flux (J) of O_2 from the aquarium seawater into the sediment was calculated from

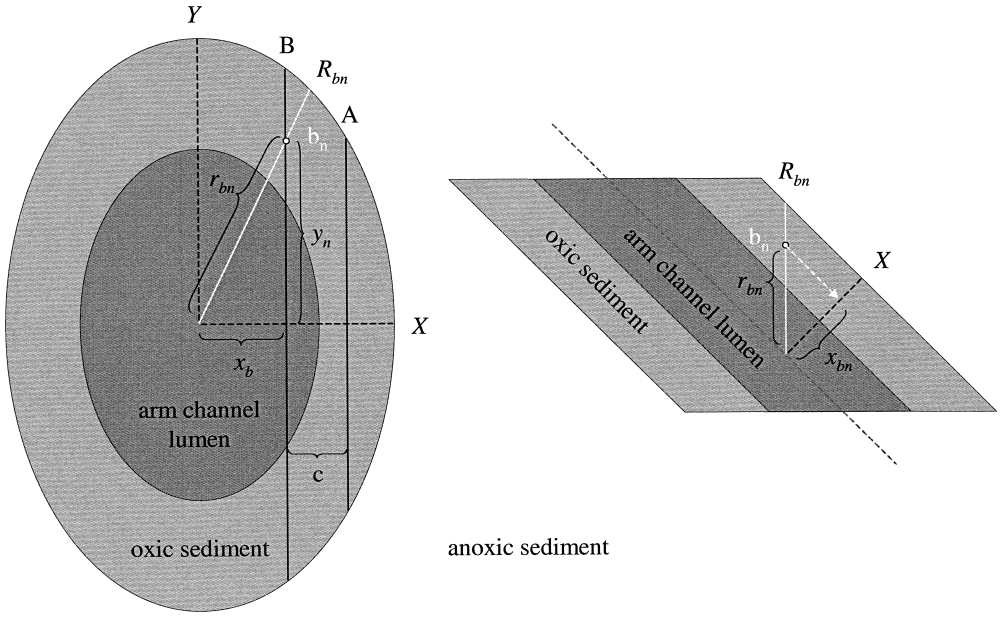

Fig. 1. (Left) Schematic drawing of the plane along which two parallel vertical profiles across the burrow–sediment interface were measured (chords A and B). (Right) Longitudinal section of the arm-channel lumen and its oxic halo. Given the lengths of chords A and B and the distance, *c*, between the two chords, the shortest distance, x_{bn}, of every measuring point, b_n, from the long axis was calculated. From these values, a pore-water $[O_2]$ profile normal to the long axis was constructed.

the measured steady-state O_2 gradients (dC/dz) in the diffusive boundary layer (Jørgensen and Revsbech 1985):

$$J = -D_0 dC/dz \quad (7)$$

where D_0 is the free-solution diffusion coefficient of O_2, C is the $[O_2]$, and z is the depth. Values of D were taken from Broecker and Peng (1974) and were recalculated to the experimental temperature with the Stokes-Einstein relation (Li and Gregory 1974).

The depth-integrated O_2 consumption rate (R) of the sediment was computed from the steady-state, sediment–pore-water profiles according to the method of Berg et al. (1998). The sediment porosity (ϕ) and, thus, the sediment diffusion coefficient (D_s) were assumed to be constant with depth or distance from the burrow wall.

Table 1. Contribution of buried adult *A. filiformis* individuals to the TOU of laboratory microcosms (MC). The contribution of inhabited burrows to the TOU was calculated from the difference between TOU of control microcosms (devoid of macrofauna) and microcosms to which brittle stars had been added. The density of the brittle stars corresponded to the abundance of 1326 ind. m^{-2}. Seawater temperature, 17 ± 0.2°C; salinity, 32; pH, 8.1.

	TOU (μmol m^{-2} h^{-1})		Number of burrow openings (extended arms)	O_2 uptake of one inhabited burrow (nmol h^{-1})
MC	Control	Treatment		
1	475.21	1290.26	32 (19)	614.79
2	453.87	1045.76	30 (15)	446.46
3	394.20	1359.62	34 (26)	728.21
4	518.45	1103.51	28 (20)	441.31
5	404.72	995.21	34 (23)	445.41
6	801.06	1608.96	31 (20)	609.39
7	852.56	1528.32	38 (22)	509.72
8	384.48	1302.19	26 (11)	692.22
9	406.24	1389.27	34 (27)	700.76
10	518.57	1354.53	32 (21)	630.59
Mean	526.34	1297.76	31.90 (20.40)	581.88
SD	157.04	189.28	3.24 (4.52)	106.71

Sediment porosity and O_2 diffusion coefficients—The porosity of the sediment (ϕ), which accounts for the tortuosity correction (Ullman and Aller 1982), was determined as the weight loss of a known volume of sediment after drying at 105°C for 24 h. The sediment diffusion coefficient for O_2 (D_s) was calculated from the temperature-corrected diffusion coefficient (D_0) and the porosity according to

$$D_s = \phi^{(m-1)} D_0$$

where $m = 2$ (Ullman and Aller 1982).

Results

Total O_2 utilization of microcosms—The average TOU of control microcosms without macrofauna was 3.97 ± 1.18 μmol h^{-1}. In contrast, the average TOU in microcosms containing 10 buried specimens of *A. filiformis* was 9.79 ± 1.43 μmol h^{-1} ($n = 10$; here and henceforth the values are given as arithmetic means ± standard deviation). Given that the area of the sediment surface of each microcosm was 75.43 cm^2, the TOU were 526 ± 157 and 1298 ± 189 μmol m^{-2} h^{-1} for control and *A. filiformis*–populated microcosms, respectively (Tables 1, 2-A1, 2-A2). The average contribution

Table 2. Summary of results from two different approaches.

Result	A: Microcosm with rotating flow	B: Aquaria with unidirectional flow
1. TOU without macrofauna	526 ± 157 μmol m^{-2} h^{-1}, measured as decrease in seawater [O_2]	358 ± 42 μmol m^{-2} h^{-1}, estimated from [O_2] profile in DBL 346 ± 35 μmol m^{-2} h^{-1}, estimated from [O_2] profile in sediment
2. TOU with density of 1326 ind. m^{-2}	1298 ± 157 μmol m^{-2} h^{-1}, measured as decrease in seawater [O_2]	1110 μmol m^{-2} h^{-1}, calculated from B3 and B1
3. TOU of 1 burrow + inhabitant	582 ± 107 nmol h^{-1}, calculated from A2 and A1	567 ± 31 nmol h^{-1}, measured as decrease in disc chamber [O_2]
4. Respiration of *A. filiformis*	191 ± 17 nmol h^{-1}, measured as decrease in respiration chamber [O_2]	
5. TOU of burrow	391 nmol h^{-1} (251 μmol m^{-2} h^{-1}), calculated from A3 and A4	1451 ± 301 μmol m^{-2} h^{-1}, flux from arm channel lumen into sediment, calculated from [O_2] profiles in burrow wall

of one buried *A. filiformis* to the TOU of the brittle-star microcosms was 582 ± 107 nmol h^{-1}, calculated from the difference between TOU of control microcosms and microcosms containing 10 brittle stars (Tables 1, 2-A3). At the completion of the measurements, an average of 32 ± 3 burrow openings and 20 ± 5 arms were visible at the sediment surface per treatment microcosm (Table 1); that is, each burrow of *A. filiformis* had three arm channels, and each individual extended two arms. A few disk chambers were visible against the cylinder at a mean sediment depth of 4.75 ± 0.56 cm (n = 6).

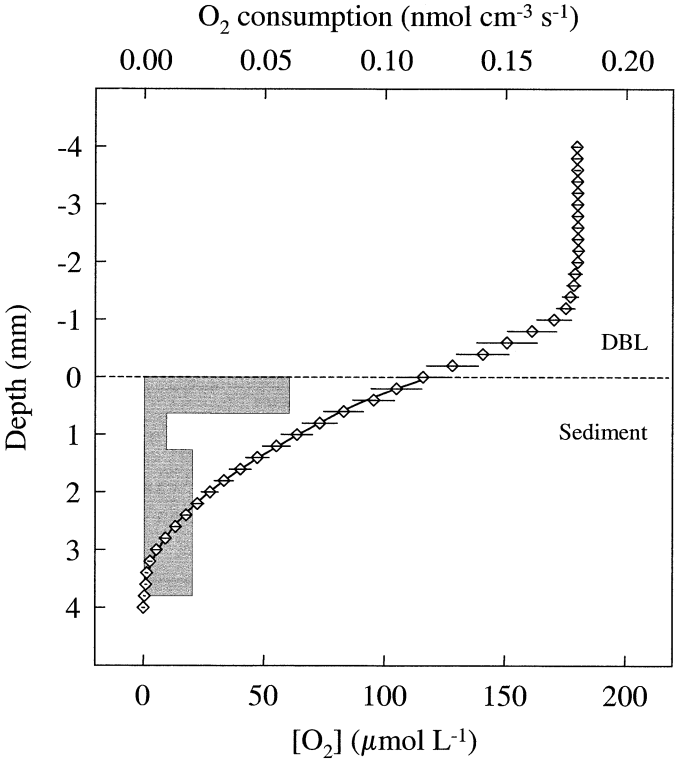

Fig. 2. Vertical [O_2] profile (diamonds) and O_2-consumption rates (bars) at the sediment–seawater interface in the aquarium. The O_2-consumption profile and the fit (R^2 = 0.9996) were calculated from the mean [O_2] profile according to the method of Berg et al. (1998). For [O_2], symbols indicate the mean (n = 6), and horizontal lines indicate standard deviations. Note that concentrations are given per volume of pore water, but consumption rates are given per volume of sediment. The sediment–water interface is located at 0 mm (dashed line). The speed of the overlying water, measured ~5 cm above the sediment surface, was ~2 cm s^{-1}. Salinity = 32; temperature = 17 ± 0.2°C.

Table 3. Respiration rate of adult *A. filiformis* specimens at a seawater temperature of 17 ± 0.2°C and a salinity of 32. The incubation lasted 4 h. The individual values were calculated from the weights and respiration rates of groups of 10 specimens for each replicate. DW, dry weight; MC, microcosm; WW, wet weight.

MC	O_2 consumption (nmol ind.$^{-1}$ h^{-1})	WW (mg)	DW (mg)	Weight-specific O_2 consumption: μmol g WW^{-1} h^{-1}	Weight-specific O_2 consumption: μmol g DW^{-1} h^{-1}
1	163.23	103.83	48.32	1.57	3.38
2	193.76	109.56	52.68	1.77	3.68
3	172.08	100.39	48.09	1.71	3.58
4	223.45	126.91	59.81	1.76	3.74
5	182.17	111.97	52.92	1.63	3.44
6	205.54	138.92	60.61	1.48	3.39
7	195.59	153.41	64.67	1.27	3.02
8	203.98	172.41	70.67	1.18	2.89
9	187.43	148.78	64.49	1.26	2.91
10	181.65	139.64	58.59	1.30	3.10
Mean	190.89	130.58	58.09	1.49	3.31
SD	16.64	22.77	7.10	0.21	0.30

Respiration of A. filiformis—The adult specimens of *A. filiformis* recovered from the microcosms had a mean individual wet weight (WW) of 131 ± 23 mg and a mean dry weight (DW) of 58 ± 7 mg (n = 10, Table 3). Their individual O_2 consumption averaged 191 ± 17 nmol O_2 h^{-1} (n = 10, Tables 2-A4, 3). Their weight-specific O_2 consumption was 1.49 ± 0.21 μmol g WW^{-1} h^{-1} and 3.31 ± 0.30 μmol g DW^{-1} h^{-1}.

O_2 flux across the DBL—Figure 2 shows the average [O_2] profile across the interface between the seawater in the aquarium and the sediment, calculated from arithmetic means of six replicate measurements. The O_2 flux into the sediment was estimated both from the [O_2] gradients in the

Table 4. Oxygen concentration in different burrow segments of undulating *A. filiformis* individuals. Average values and standard deviations were calculated from means of 1500 data points continuously recorded at a frequency of 25 Hz. The speed of the overlying water, measured ~5 cm above the sediment surface, was ~2.0 cm s^{-1}.

Burrow region	Arm position	$[O_2]$ (μmol L^{-1})
Arm-channel entry	On sediment surface	102.8 ± 28.9
Arm-channel lumen, depth ~ 1.5 cm	Upright	220.3 ± 32.6
Disk-chamber lumen	Upright	110.5 ± 27.4

diffusive boundary layer (DBL) and from the pore-water–$[O_2]$ profiles. The thickness of the effective diffusive boundary layer (Jørgensen and Revsbech 1985) was ~1 mm, and the average $[O_2]$ gradient in the DBL was 0.547 ± 0.064 μmol cm^{-4}. Under the assumption of $D = 1.814 \times 10^{-5}$ cm^2 s^{-1} at a seawater temperature of 17°C and a salinity of 32, the average O_2 flux from the seawater into the sediment was 358 ± 42 μmol m^{-2} h^{-1} (Table 2-B1).

O_2 penetrated 4 mm into the sediment. We used the six replicate measurements of pore-water $[O_2]$ to compute the best-fitting concentration profiles and the resulting O_2-consumption profiles. The porosity of the sediment was ϕ = 0.83, so the diffusivity corrected for tortuosity was D_S = 1.51×10^{-5} cm^2 s^{-1}. Bioturbation and irrigation by meiofauna were neglected. The calculated concentration profiles closely matched the data points, giving R^2 values >0.999. The average depth-integrated, O_2-consumption rate (the equivalent flux across the sediment–water interface) was 346 ± 35 μmol m^{-2} h^{-1} (Table 2-B1). The highest O_2 consumption rates (0.06 nmol cm^{-3} s^{-1}) were found in the upper zone of the sediment (Fig. 2).

Burrow water $[O_2]$—A few *A. filiformis* individuals lowered the extended, upright parts of their arms toward the sediment surface at a bottom-water flow of ~2 cm s^{-1}. This arm position allowed us to insert the electrode into the opening of the arm channel so that the sensor tip was positioned on one side of the arm, 1 mm below the sediment surface. The $[O_2]$ there averaged 103 ± 29 μmol L^{-1} (n = 8) (Table 4; curve 1 in Fig. 3A as an example). Note that we did not take measurements at this position with the extended parts of the arms in an upright position.

Burrows that were partially visible against the wall of the aquarium allowed us to record $[O_2]$ in the burrow lumen with visual control of the sensor-tip position and the behavior of the brittle stars. The $[O_2]$ in the channel lumen of undulating arms that had their tips extended and in upright position averaged 220 ± 33 μmol L^{-1} (n = 12) measured ~1.5 cm below the sediment surface (Table 4; curve 2–3 in Fig. 3A). In the lumen of the disk chambers of undulating individuals, a mean $[O_2]$ of 111 ± 27 μmol L^{-1} (n = 8) was measured (Table 4; curve 4 in Fig. 3A as an example).

Undulation frequency—The continuous recordings in burrow lumens gave rising and falling values (Fig. 3A) because of the undulating movements of the arms of the brittle stars. Depending on the position of the sensor tip, one side or the other of the arm (Fig. 3A, curves 1, 2, and 4; Fig. 3B) or

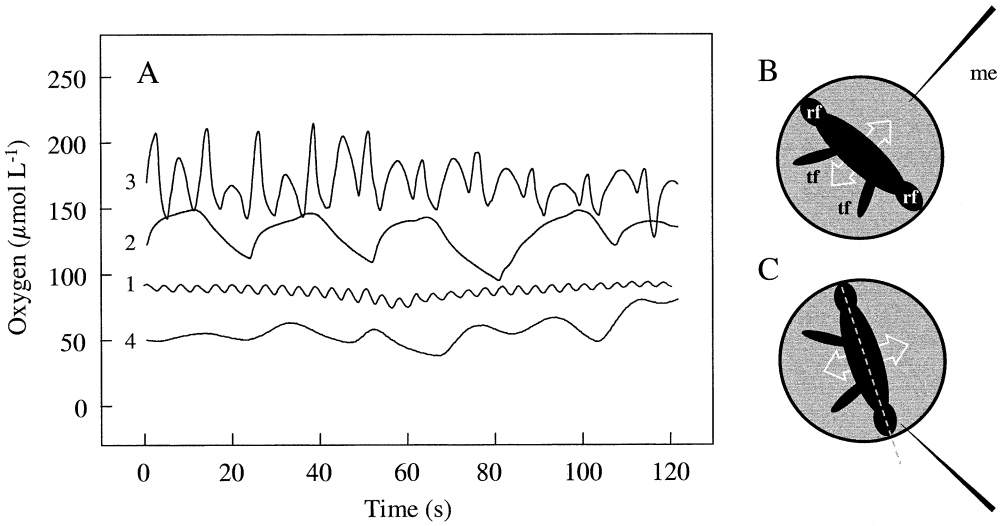

Fig. 3. *A. filiformis*. (A) Recordings of $[O_2]$ (1) at the burrow opening; (2) and (3) in the lumen of an arm channel, ~1.5 cm below the sediment surface; and (4) in the disk chamber. (B,C) Schematic drawing of a arm-channel cross section and a microelectrode (me). White arrows indicate the direction of the arm's movement. The arm is flanked by projecting spines, which may account for about half the total width of the arm. The respiratory fringes (rf) are aggregations of substratum particles consolidated with mucus. During undulation, the driving effect of the trunk of the arm would be reduced by the lateral displacement of water through the gaps between the arrays of spines if these gaps were not blocked by these aggregations of particles. The tube feet (tf) project downward, clear of the fringe, during undulation.

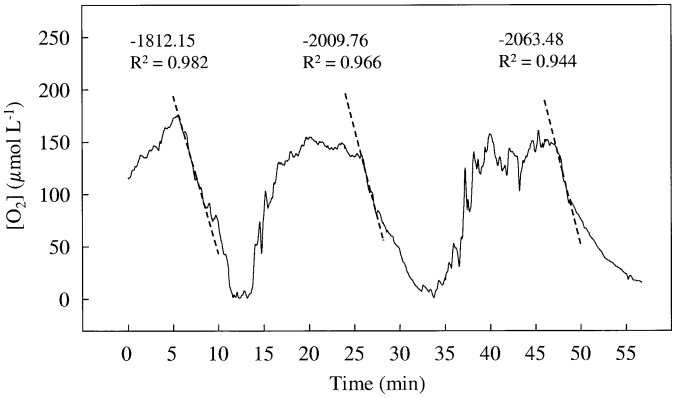

Fig. 4. *A. filiformis* disk chamber [O_2]. At 5, 25, and 45 min, the burrow openings were blocked. The slopes of the [O_2] curves immediately after closure are shown (μmol L^{-1} h^{-1}). From these slopes, the total oxygen consumption of the inhabited burrow was estimated. Salinity = 32; temperature = 17 ± 0.2°C.

the respiratory fringes (Fig. 3A, curve 3; Fig. 3C) disturbed the sensor tip, causing a rapidly decreasing signal once or twice per undulation, respectively. This effect was used to estimate the frequency of undulation. Measurements with the sensor tip positioned ~1.5 cm below the sediment surface in the lumen dorsal or ventral of arms whose tips were extended and upright revealed an undulation frequency of 2.4 ± 0.2 min^{-1} (n = 3). A higher frequency of 4.9 ± 0.2 min^{-1} (n = 9) was observed shortly after the flow in the aquarium was stopped (Fig. 3A, curve 3). During the latter recordings, the respiratory fringe of the arm passed the sensor tip twice per undulation; that is, the sensor detected the [O_2], for example, for 3.6–6.2 s on one side and 6.2–8.6 s on the other side of the arm. The different durations of the exposures indicated that the sensor tip was not in line with the lateral axis of the arm (Fig. 3C). The durations of the two phases were negatively correlated (ρ = −0.904); that is, the exposure of the sensor tip to one side of the arm increased when the exposure to the opposite side decreased. This negative correlation arose because the arm rotated along its longitudinal axis when the extended arm tip moved from an upright position toward the sediment surface. The undulation frequency of the distal end of the buried arm estimated from the [O_2] measurements in the channel opening 1 mm below the sediment surface averaged 15.3 ± 1.1 min^{-1} (Fig. 3A, curve 1).

O_2 demand of inhabited burrows—We estimated the O_2 demand of an inhabited burrow by measuring the change of the [O_2] in the disk chamber immediately after plugging the uppermost millimeter of all three arm channels with sediment using a small spatula. A microelectrode was inserted into the disk chamber in such a way that the tip of the electrode was positioned in the seawater-filled space between the disk of the brittle star and the inner surface of the disk chamber. Immediately after the openings of the burrow had been closed, the [O_2] in the disk chamber dropped quasi-linearly (R^2 = 0.964 ± 0.016) at a rate of 1962 ± 108 μmol L^{-1} h^{-1} (three trials, same burrow; Fig. 4). The burrow system consisted of three arm channels, each 6.7 cm long and 2.31 mm wide, and a hemispherical disk chamber (diameter = 0.8 cm), so the total surface area and the volume of the burrow were 15.60 cm^2 and 0.977 ml, respectively. Subtracting the volume of the inhabitant (0.688 ml) from the volume of the burrow gives the volume of the seawater in the burrow, 0.289 ml. The total O_2 consumption of the burrow + inhabitant was 567 ± 31 nmol h^{-1} (Table 2-B3).

Pore water [O_2] around arm channels—Figure 5B–F shows [O_2] profiles in a plane normal to the long axis of the arm channel, constructed from vertical measurements across the lumens of the arm channels and the surrounding sediment (chords A and B, Fig. 1). An example of such measurements is shown in Fig. 5A. The stepwise [O_2] measurements in the sediment immediately surrounding the arm channels (see below) gave stable readings at each distance from the inner surface of the channel. The lengths of the chords A and B were defined by the points along the profile at which O_2 was detected. The relative position of the inner surface of the arm channel was detected by the onset of oscillating readings and the abrupt change in [O_2]. The profiles across the arm channels revealed that O_2 penetrated the surrounding sediment 0.73 ± 0.18 mm (n = 5). The maximum thickness of the oxic halo was 1.04 mm; the minimum thickness was 0.53 mm. The average diameter of the arm channels was 2.31 ± 0.25 mm (maximum, 2.61 mm; minimum, 1.95 mm). The [O_2] at the inner surface of the arm channel ranged from 85 (Fig. 5F) to 202 μmol L^{-1} (Fig. 5B).

On the simplifying assumption that the oxygenated zone around the arm-channel lumen is planar, the O_2-consumption rate as a function of the distance from the inner surface of the lumen and the flux across the wall of the lumen can be calculated according to the method of Berg et al. (1998). Irrigation and bioturbation by meiofauna were neglected, and the sediment porosity and thus the sediment diffusion coefficient were assumed to be constant with distance from the burrow wall. The measured [O_2] profiles normal to the long axis of the arm-channel lumen, the calculated best-fitting concentration profiles, and the consumption profiles are shown in Fig. 5B–F. The average integrated O_2 consumption of the burrow wall area ~1.5 cm below the sediment surface calculated from the five replicate profiles was 1451 ± 301 μmol m^{-2} h^{-1} (Table 2-B5). The O_2 consumption rates were at their highest at the interface between the lumen and the burrow wall (Fig. 5D–F) and at the transition between the oxic and anoxic zones (Fig. 5B,C).

Discussion

The aim of our study was to quantify the effect of the ophiuroid *A. filiformis* on the total O_2 flux into the sediment. For this purpose, we measured the O_2 utilization of enclosures of both macrofauna-free sediment and sediment in which brittle stars had buried themselves. These experiments were supplemented by microscale [O_2] measurements in an aquarium with flowing seawater, where in situ boundary-layer flow conditions could be simulated. In the following, we will compare and discuss the results of these two different approaches and then use our data to estimate the contri-

bution of a natural *A. filiformis* population to the O_2 flux into the sediment.

The results from our microcosm experiments incorporate various possible effects of the brittle stars on the O_2 flux. The microelectrode measurements in the flow aquarium, in contrast, allowed the O_2 flux to be measured under more realistic flow conditions and permitted recordings of $[O_2]$ in different regions of the burrow at high temporal and spatial resolution. Because the buried brittle stars remained in the same burrows during our experiments, the possible effects of sediment reworking due to density-dependent migration of the brittle stars could not be considered.

O_2 uptake of macrofauna-free sediment—The diffusive O_2 flux into the sediment of the flow aquarium calculated from O_2 gradients in the DBL agreed well with the O_2 uptake rate modeled from the pore-water $[O_2]$ profile (Table 2-B1). Such consistency was also reported in studies in coastal and deep-sea regions by Rasmussen and Jørgensen (1992) and Glud et al. (1994). The estimated TOU of the control microcosms (without macrofauna) was higher than the O_2 flux into the sediment of the aquaria (by a factor of 1.47; Table 2, compare A1 and B1). This difference probably resulted because, in contrast to the value calculated from microelectrode recordings in the aquaria, the values from our microcosm measurements integrated the O_2 uptake of the seawater overlying the sediment. The latter was independently estimated during the measurement of brittle-star respiration (control) to be 1.36 μmol L^{-1} h^{-1}, so it contributed ~20% of the TOU of the control microcosm. The difference between microcosm TOU and the O_2 uptake of the sediment in the aquaria might also have been due to the rotating flow in the microcosms, which prevented the development of natural DBL (~1 mm thick). As a consequence, higher $[O_2]$ occurred at the sediment surface, and the sediment therefore consumed more O_2. The probability of pore-water irrigation by pressure gradients that exist in rotating flow is likely to be negligible in muddy sediment, in contrast to the situation in permeable sediments, where this irrigation increases the O_2 flux significantly (Huettel and Gust 1992; Booij et al. 1994; Glud et al. 1996).

Impact of A. filiformis *on the TOU of the sediment*—Buried *A. filiformis* contribute to the total O_2 flux by their respiration and by the O_2 uptake of the additional sediment surface that they create (i.e., the inner surfaces of their burrows). The mounds around their burrow openings are made of sediment from deeper layers ejected to the surface as the feeding arms push up through the sediment–water interface. This sediment can consume more O_2 than the surrounding surficial sediment, as was shown for mounds raised by *C. subterranea* by Forster and Graf (1995). Furthermore, the extended arms of *A. filiformis* can increase the O_2 uptake of the superficial sediment by disturbing the boundary layer flow and by moving particles while sweeping the sediment surface in circles (Duchêne and Rosenberg 2001). We estimated the TOU of an inhabited burrow from (1) the decrease in the $[O_2]$ of the seawater in the microcosms with and without brittle stars (Table 2-A3) and (2) direct measurements of $[O_2]$ in the disk chamber after all burrow openings had been closed (Table 2-B3). The values from (1) integrate all above-mentioned effects, whereas the microelectrode approach used in (2) accounts only for the $[O_2]$ uptake of the brittle star and the inner burrow surface. Because these two different estimates gave similar results, the possible effects of the excavated sediment (mounds) and the activity of the brittle star arms at and on the sediment surface are likely to be negligible. Given the diffusive O_2 uptake of the sediment surface (Table 2-B1) and the TOU of a buried individual as calculated from our microscale measurements under conditions of unidirectional boundary layer flow in the aquaria (Table 2-B3), the TOU of sediment populated by 1326 individuals m^{-2} would be 1110 μmol m^{-2} h^{-1} (Table 2-B2). This value is only 15% smaller than the value calculated from our microcosm experiments (Table 2-A2).

Respiration by A. filiformis—We measured the mean weight-specific O_2 consumption of *A. filiformis* to be 1.5 μmol g WW^{-1} h^{-1} by incubating the brittle stars in air-free flasks of normoxic seawater without sediment. A similar approach was used by Buchanan (1964), who reported a higher respiration rate of 0.058 ml O_2 g WW^{-1} h^{-1} = 2.59 μmol g WW^{-1} h^{-1} at a lower temperature of 6°C. In neither case were conditions natural. Our measurements in the main chamber of the burrow revealed that the disk of the brittle star experienced an $[O_2]$ of only 40%–48% air saturation. At low $[O_2]$, respiration rates of benthic animals decline (Theede et al. 1973), so *A. filiformis* is likely to consume less O_2 in its natural environment than during our respiration measurement. Nevertheless, we use this value (Table 2-A4) to estimate the total O_2 flux across the burrow wall by subtracting it from the calculated burrow TOU (Table 2-A3, see below), because a possible discrepancy between the measured and the actual respiration rate of a buried *A. filiformis* is apparently balanced by the O_2 consumption of the sediment constituting the ''respiratory fringe'' of the brittle star and of the sediment particles transported along the arms.

O_2 uptake of the inner burrow surface—Given that the TOU of an inhabited burrow was 582 nmol h^{-1} (Table 2-A3) and that the respiration rate measured under normoxic conditions (Table 2-A4) accounted for the O_2 consumption of the buried brittle star, its ''respiratory fringe,'' and mobile sediment particles, the O_2 demand of the inner burrow surface would be 391 nmol h^{-1}—that is, 67% of burrow TOU (Table 2-A5). A calculation based on the burrow TOU of 567 nmol h^{-1}, as estimated from the change in burrow water $[O_2]$ after irrigation was stopped (Fig. 4; Table 2-B3), gives a marginally lower value of 66% of burrow TOU (376 nmol h^{-1}).

On the assumptions that the O_2 demand of the burrow wall was 391 nmol h^{-1} and that the inner surface area of the burrow was 15.6 cm^2, the O_2 flux from the burrow lumen into the surrounding sediment would be 251 μmol m^{-2} h^{-1} (Table 2-A5). This flux is 30% lower than the flux estimated for the sediment surface (Table 2-B1). The average O_2 flux calculated from the microelectrode measurements around the arm channels, however, was 1451 μmol O_2 m^{-2} h^{-1}—5.8 times higher than the value calculated above. This rate applies only to the upper region of the arm channel, however.

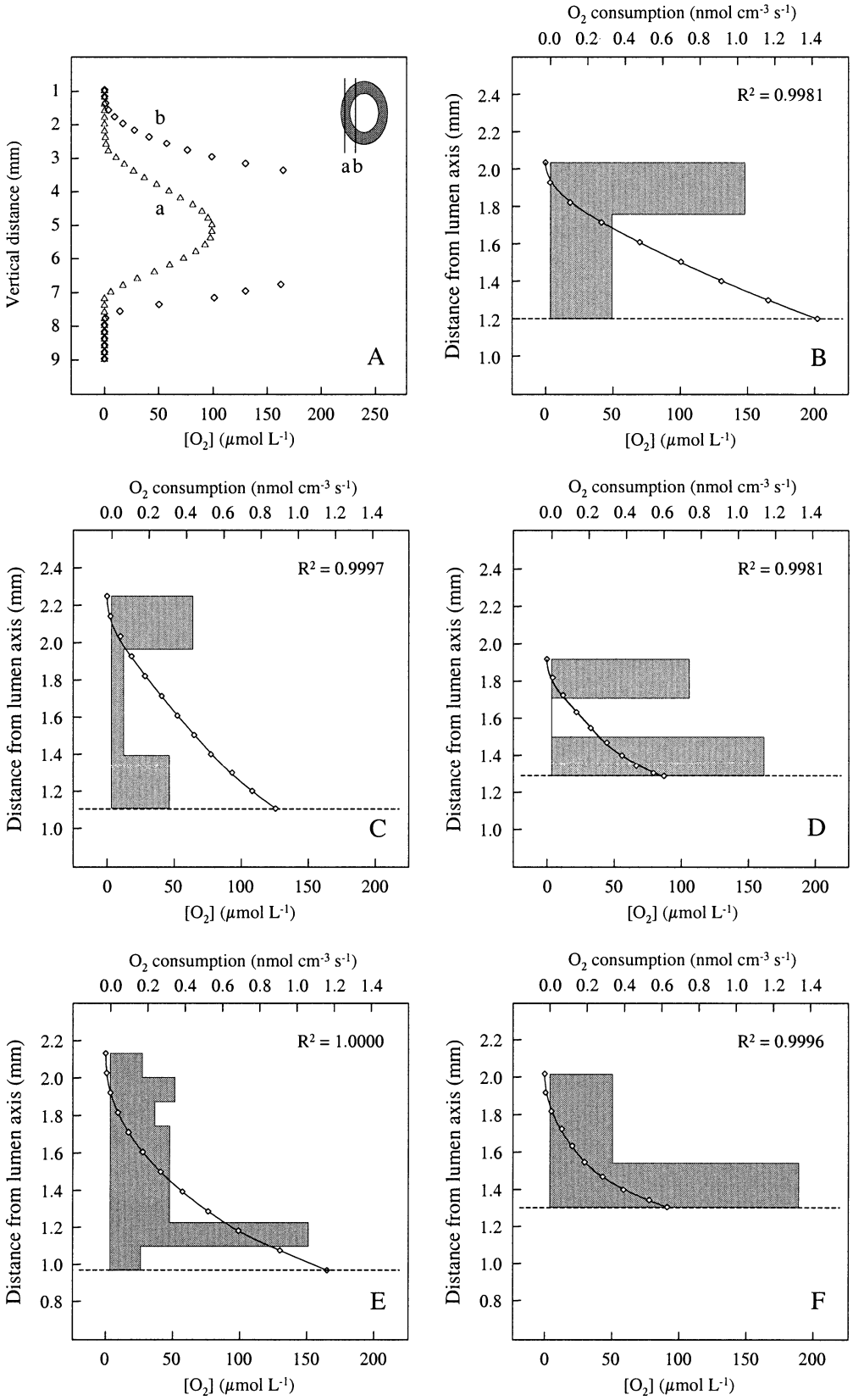

Fig. 5. (A) Example of two parallel, vertical profiles of pore-water $[O_2]$ (a, b) across the sediment immediately surrounding the lumen of an *A. filiformis* arm channel (see inset). The tip of the electrode crossed the long axis of the arm channel lumen ~1.5 cm below the sediment surface at

The $[O_2]$ in the channel lumen decreased with increasing sediment depth, and so should the flux into the surrounding sediment. Furthermore, the $[O_2]$ profiles across the burrow wall were only measured in channels of undulating arms. Although *A. filiformis* usually has two arms extended (Table 1; Loo et al. 1996), apparently only one arm ventilates the burrow; seawater is driven down that arm to the disk and then flows passively up the other channels (Ockelmann and Muus 1978), so the $[O_2]$ in the lumen and the O_2 flux into the sediment surrounding the latter channels were likely to be lower. The O_2-consumption profiles across the sediment surrounding the channel lumen (Fig. 5) were calculated on the assumption that the porosity (and diffusivity) of this sediment equaled the porosity of the bulk sediment. The channel wall, however, was apparently compacted and stabilized with mucus (Buchanan 1964; Woodley 1975). Compaction would decrease the diffusivity for solutes, so our calculation would overestimate the flux. Higher consumption rates near the inner surface of the burrow (Fig. 5) were probably due to the supply of easily degradable material. The higher O_2 consumption at the oxic/anoxic interface can be explained by an oxidation of reduced organic and inorganic compounds from the anaerobic mineralization in the surrounding sediment.

The comparison of our different estimates for the O_2 uptake of the burrow wall shows that, for a realistic estimate of the total O_2 uptake of the inner surface of the burrow system, a large number of $[O_2]$ profiles measured in different parts of the burrow would be required. Combining microscale measurements with enclosure experiments, however, provides the average TOU of the burrow system and detailed information on the behavior of the brittle stars. Our measurement of $[O_2]$ in different sections of the burrow system revealed that, in future studies, microelectrodes can be used to investigate how the behavior associated with its response to changes in boundary layer conditions and food supply of the buried brittle star affects the burrow chemistry. Such studies can be carried out in situ because visual control of the electrode tip within the sediment is not essential.

Behavioral control of solute transport—Oxygenation of the burrow water and the pore water of the sediment surrounding the lumen of the burrow is determined by behavior patterns associated with three main functions of the arms: ventilation and respiration, the transportation of sediment and waste material out of the burrow, and the collection and transportation of food (Woodley 1975; Ockelmann and Muus 1978). The oxygenation of the pore water surrounding the lumen of the burrow is crucial for *A. filiformis* and the associated micro- and meiofauna because it prevents the diffusion of sulphide into the burrow system. Vistisen and Vismann (1997) showed that, although this brittle star tolerates hypoxia very well, even low concentrations of sulfide decrease its survival significantly. *A. filiformis* is apparently able to avoid contact with sulfide by maintaining a seawater flow through the burrow given a bottom-water $[O_2]$ as low as 10% saturation. At lower concentrations, the brittle star leaves its protected position in the sediment and appears at the sediment surface (Rosenberg et al. 1991; Vistisen and Vismann 1997). The aeration of the burrow is controlled by a wavelike undulation of one arm within its channel and by pumping due to raising and lowering of the disk (Woodley 1975). The wavelength and period increase from the burrow opening toward the disk (compare curves 1 and 2 in Fig. 3). Under conditions of bottom-water flow, the wave period measured at the burrow entrance was 4 s. This observation agrees with that of Woodley (1975). Shortly after the flow was stopped, the wave period, measured ~1.5 cm below the sediment surface, decreased from 25 to 12 s. Similar behavior was observed by Woodley (1975), who reported that in stagnant water the movement sometimes reached a rate of 100 waves min^{-1} (a period of 0.6 s, most probably measured at the burrow entrance).

A. filiformis can switch between deposit and suspension feeding; that is, the extended arm tips are held low to explore the surface of the sediment for particles or up vertically to a distance of 3–4 cm above the sediment surface to trap both nonliving particulate suspended matter and phytoplankton (Buchanan 1964; Woodley 1975). Our measurements indicated that these different arm positions affected burrow-water oxygenation. Under flow conditions, the average $[O_2]$ at the burrow opening was as low as 103 μmol L^{-1} when the extended arms were positioned on the surface of the sediment (Table 4). This value approximated the values measured at the sediment surface under conditions of diffusion across the DBL (Fig. 2). Although we were not able to measure $[O_2]$ at the burrow opening when the arm tip was in the upright position, our recordings in the channel lumen, ~1.5 cm below the sediment surface, revealed an average of 220 μmol O_2 L^{-1} (Table 4), indicating that this arm position results in an advective transport of seawater toward the arm channel opening and therefore in a higher burrow-water $[O_2]$.

Potential impact of A. filiformis *on TOU of soft bottoms*—If bottom seawater is fully oxygenated and the average O_2 demand of a buried adult *A. filiformis* is 582 nmol h^{-1} (Table 2-A3), the diffusional O_2 flux into a square meter of macrofauna-free sediment (~350 μmol h^{-1}; Table 2-B1) would be doubled by the presence of only 600 individuals of *A. filiformis.* The densities of natural populations of *A. filiformis* are known to be >3000 individuals m^{-2} (Rosenberg 1976, 1995; Josefson 1995). At a somewhat lower density of 2500

←

an angle of 45°. From such measurements, an $[O_2]$ profile normal to the long axis of the arm channels was constructed (B–F, symbols). The fits and the O_2-consumption profiles (bars) in panels B–F were calculated from the $[O_2]$ profiles as described by Berg et al. (1998). Note that $[O_2]$ is given per volume of pore water, but consumption rates are given per volume of sediment. A dashed line indicates the interface between the burrow lumen and the surrounding sediment.

individuals m^{-2}, as reported by Rosenberg (1995) for the east and west slopes (65–90 m depth) of a trench in the Skagerrak, western Sweden, at least 80% of the total O_2 flux into the sediment would be due to *A. filiformis*. Given the additional effects of associated infaunal species on the total O_2 flux, the portion of the total transport attributable to diffusion through the boundary layer of the sediment surface would be <20%. This example emphasizes that information on how key species control their physical microenvironment is crucial for a better understanding of solute exchange across the sediment–water interface.

References

ALLER, R. C. 1980. Quantifying solute distributions in the bioturbated zone of marine sediments by defining an average microenvironment. Geochim. Cosmochim. Acta **44:** 1955–1965.

———, AND J. Y. ALLER. 1992. Meiofauna and solute transport in marine muds. Limnol. Oceanogr. **37:** 1018–1033.

———, AND J. Y. YINGST. 1978. Biogeochemistry of tube-dwellings: A study of the sedentary polychaete *Amphitrite ornata* (Leidy). J. Mar. Res. **36:** 201–254.

———, ———, AND W. J. ULLMAN. 1983. Comparative biogeochemistry of water in intertidal *Onuphis* (Polychaeta) and *Upogebia* (Crustacea) burrows: Temporal patterns and causes. J. Mar. Res. **41:** 571–604.

BERG, P., N. RISGAARD-PETERSEN, AND S. RYSGAARD. 1998. Interpretation of measured concentration profiles in sediment pore water. Limnol. Oceanogr. **43:** 1500–1510.

BOOIJ, K., B. SUNDBY, AND W. HELDER. 1994. Measuring the flux of oxygen to a muddy sediment with a cylindrical microcosm. Neth. J. Sea Res. **32:** 1–11.

BROECKER, W. S., AND T.-H. PENG. 1974. Gas exchange rates between air and sea. Tellus **26:** 185–190.

BUCHANAN, J. B. 1964. A comparative study of some features of the biology of *Amphiura filiformis* and *Amphiura chiajei* [Ophiuroidea] considered in relation to their distribution. J. Mar. Biol. Assoc. U.K. **44:** 565–576.

DE WILDE, P.A.W.J., E. M. BERGHUIS, AND A. KOK. 1984. Structure and energy demand of the benthic community of the Oyster Ground, central North Sea. Neth. J. Sea Res. **18:** 143–159.

DUCHÊNE, J.-C., AND R. ROSENBERG. 2001. Marine benthic faunal activity patterns on a sediment surface assessed by video numerical tracking. Mar. Ecol. Prog. Ser. **223:** 113–119.

FORSTER, S., R. N. GLUD, J. K. GUNDERSEN, AND M. HUETTEL. 1999. In situ study of bromide tracer and oxygen flux in coastal sediments. Estuar. Coast. Mar. Sci. **49:** 813–827.

———, AND G. GRAF. 1995. Impact of irrigation on oxygen flux into the sediment: Intermittent pumping by *Callianassa subterranea* and ''piston-pumping'' by *Lanice conchilega*. Mar. Biol. **123:** 335–346.

GLUD, R. N., S. FORSTER, AND M. HUETTEL. 1996. Influence of radial pressure gradients on solute exchange in stirred benthic chambers. Mar. Ecol. Prog. Ser. **141:** 303–311.

———, J. K. GUNDERSEN, B. B. JØRGENSEN, N. P. REVSBECH, AND H. D. SCHULZ. 1994. Diffusive and total oxygen uptake of deep-sea sediment in the eastern South Atlantic Ocean: In situ and laboratory measurements. Deep-Sea Res. I **41:** 1767–1788.

GUNDERSEN, J., AND B. B. JØRGENSEN. 1990. Microstructure of diffusive boundary layers and the oxygen uptake of the sea floor. Nature **345:** 604–607.

GUST, G., AND J. T. HARRISON. 1981. Biological pumps at the sediment-water interface: Mechanistic evaluation of the alpheid shrimp *Alpheus mackayi* and its irrigation pattern. Mar. Biol. **64:** 71–78.

HUETTEL, M., AND G. GUST. 1992. Solute release mechanisms from confined sediment cores in stirred benthic chambers and flume flows. Mar. Ecol. Prog. Ser. **82:** 187–197.

JØRGENSEN, B. B., AND N. P. REVSBECH. 1985. Diffusive boundary layers and the oxygen uptake of sediments and detritus. Limnol. Oceanogr. **30:** 111–122.

JOSEFSON, A. B. 1995. Large-scale estimate of somatic growth in *Amphiura filiformis* (Echinodermata: Ophiuroidea). Mar. Biol. **124:** 435–442.

KRAGER, C. D., AND S. A. WOODIN. 1993. Spatial persistence and sediment disturbance of an arenicolid polychaete. Limnol. Oceanogr. **38:** 509–520.

LI, Y.-H., AND S. GREGORY. 1974. Diffusion of ions in sea water and in deep-sea sediments. Geochim. Cosmochim. Acta **38:** 703–714.

LOO, L.-O., P. R. JONSSON, M. SKÖLD, AND Ö. KARLSSON. 1996. Passive suspension feeding in *Amphiura filiformis* (Echinodermata: Ophiuroidea): Feeding behaviour in flume flow and potential feeding rate of field populations. Mar. Ecol. Prog. Ser. **139:** 143–155.

MARINELLI, R. L. 1992. Effects of polychaetes on silicate dynamics and fluxes in sediments: Importance of species, animal activity and polychaete effects on benthic diatoms. J. Mar. Res. **50:** 745–779.

MEYERS, M. B., H. FOSSING, AND E. N. POWELL. 1987. Microdistribution of interstitial meiofauna, oxygen and sulfide gradients, and the tubes of macro-infauna. Mar. Ecol. Prog. Ser. **35:** 223–241.

OCKELMANN, K. W., AND K. MUUS. 1978. The biology, ecology and behaviour of the bivalve *Mysella bidentata* (Montagu). Ophelia **17:** 1–93.

O'CONNOR, B., T. BOWMER, AND A. GREHAN. 1983. Long-term assessment of the population dynamics of *Amphiura filiformis* (Echinodermata, Ophiuroidea) in Galway Bay, west coast of Ireland. Mar. Biol. **75:** 279–286.

PIKE, J., J. M. BERNHARD, S.G. MORETON, AND I. B. BUTLER. 2001. Microbioirrigation of marine sediments in dysoxic environments: Implications for early sediment fabric formation and diagenetic processes. Geology **29:** 923–926.

RASMUSSEN, H., AND B. B. JØRGENSEN. 1992. Microelectrode studies of seasonal oxygen uptake in a coastal sediment: Role of molecular diffusion. Mar. Ecol. Prog. Ser. **81:** 289–303.

ROSENBERG, R. 1976. Benthic faunal dynamics during succession following pollution abatement in a Swedish estuary. Oikos **27:** 414–427.

———. 1995. Benthic marine fauna structured by hydrodynamic processes and food availability. Neth. J. Sea Res. **34:** 303–317.

———, B. HELLMANN, AND B. JOHANSSON. 1991. Hypoxic tolerance of marine benthic fauna. Mar. Ecol. Prog. Ser. **79:** 127–131.

———, H. C. NILSSON, K. HOLLERTZ, AND B. HELLMAN. 1997. Density-dependent migration in an *Amphiura filiformis* (Amphiuridae, Echinodermata) infaunal population. Mar. Ecol. Prog. Ser. **159:** 121–131.

SKÖLD, M., L.-O. LOO, AND R. ROSENBERG. 1994. Production, dynamics and demography of an *Amphiura filiformis* population. Mar. Ecol. Prog. Ser. **103:** 81–90.

SOLAN, M., AND R. KENNEDY. 2002. Observation and quantification of in situ animal-sediment relations using time-lapse sediment profile imagery (t-SPI). Mar. Ecol. Prog. Ser. **228:** 179–191.

THEEDE, H., J. SCAUDINN, AND F. SAFFÉ. 1973. Ecophysiological studies on four *Nereis* species of the Kiel Bay. Oikos Suppl. **15:** 246–252.

ULLMAN, W. J., AND R. C. ALLER. 1982. Diffusion coefficients in nearshore marine sediments. Limnol. Oceanogr. **27:** 552–556.

VISTISEN, B., AND B. VISMANN. 1997. Tolerance to low oxygen and sulfide in *Amphiura filiformis* and *Ophiura albida* (Echinodermata: Ophiuroidea). Mar. Biol. **128:** 241–246.

WITBAARD, R., AND G. C. A. DUINEVELD. 1989. Some aspects of the biology and ecology of the burrowing shrimp *Callianassa subterranea* (Montagu) (Thalassinidae) from the southern North Sea. Sarsia **74:** 209–219.

WOODLEY, J. D. 1975. The behaviour of some amphiurid brittlestars. J. Exp. Mar. Biol. Ecol. **18:** 29–46.

Received: 8 October 2002
Accepted: 25 March 2003
Amended: 13 April 2003